ABSTRACT

BEGENIR, ASLI. Structure-Process-Property Relationships in Elastic Nonwovens Made From Multi-Block Elastomers. (Under the direction of Stephen Michielsen and Behnam Pourdeyhimi.)

Melt-blown webs from ester and ether thermoplastic polyurethanes (TPU) and polyether-block-amide (PEBA) elastomers were produced at different die-to-collector distances (DCD) to study the correlation between polymer type, process conditions and web properties. Air temperature and velocity profiles were measured and modeled to correlate fiber formation to melt-blowing conditions. Isothermal crystallization kinetics was measured by DSC, and analyzed by traditional Avrami and model proposed by Kurajica. Web tensile properties were explained in terms of crystallization kinetics along with air temperature profile.

Crystallization kinetic parameters derived from both models exhibited similar temperature, polymer type and hardness dependence. The air flow field from simulations showed good agreement with experimental profiles and enabled modeling of fiber formation in melt-blowing. Both air temperature and velocities dropped significantly even at the die tip and continued to fall rapidly until reaching a plateau. The crystallization onset temperatures were found to fall within DCD region of rapid air velocity and temperature drop. This suggests that polymers already started to crystallize before collector, the extent of which depends on crystallization kinetics.

Web strength behavior was highly dependent on DCD and polymer hardness. By mapping crystallization behavior onto air temperature profile, polymer crystallization kinetics was observed to have a profound effect on web strength. This was clearly

demonstrated in PEBA series, in particular with the hardest grade, P55 which produced the lowest web strength mainly due to its significantly higher crystallization rate. It is concluded that web tensile behavior is strongly dependent on degree of fiber solidification achieved within the web, which is determined by crystallization kinetics and distances traveled between die and collector. Moreover, polymer extrusion and air temperatures as well as air velocity are critical in determining the amount of time it takes for polymer melt to travel the distance from the die to collector and the temperature that fibers have upon reaching collector.

Structure-Process-Property Relationships in Elastic Nonwovens Made from Multi-Block Elastomers

by
Asli Begenir

A dissertation submitted to the Graduate Faculty of
North Carolina State University
In partial fulfillment of the
Requirements for the degree of
Doctor of Philosophy

Fiber and Polymer Science

Raleigh, North Carolina

2008

APPROVED BY:

Dr. Sam M. Hudson	Dr. Martin A. Hubbe
Dr. Stephen Michielsen Co-chair of Advisory Committee	Dr. Behnam Pourdeyhimi Co-chair of Advisory Committee

BIOGRAPHY

Asli Begenir received her Bachelor of Science degree in Textile Engineering in 1999 from Uludag University, Turkey and obtained her Master of Science in Textile & Apparel Technology & Management in 2002 from North Carolina State University, USA. She joined Hanes Brands Inc. (formerly Sara Lee Branded Apparel) in 2003 and North Carolina State University to enroll her Doctoral program in Fiber and Polymer Science in fall 2004.

ACKNOWLEDGEMENTS

I would like to express my sincere gratitude to Dr. Stephen Michielsen and Dr. Behnam Pourdeyhimi for being my advisors, their great supervision, patience and encouragement throughout the course of this research. I would also like to thank Dr. Martin A. Hubbe and Dr. Sam M. Hudson for serving on my advisory committee and providing helpful suggestions and feedback.

I would like to extend many thanks to Hanes Brands Inc. (formerly Sara Lee Branded Apparel) and Nonwovens Cooperative Research Center (NCRC) for funding this research. Appreciation is also extended to all NCRC staff and students for their support and friendship.

Finally, I wish to thank my husband, Bener Doguc for his constant patience, encouragement and support.

TABLE OF CONTENTS

LIST OF TABLES

LIST OF FIGURES

I. INTRODUCTION

Thermoplastic elastomers (TPE) are semi-crystalline block copolymers consisting of crystalline hard and amorphous soft polymeric segments. They can be processed using thermoplastic processes while recovering their rubber-like properties upon cooling to room temperature. TPEs owe their unique combination of plastic and elastic attributes to their two-phase morphology resulting from two competing self-organizing mechanisms: crystallization of hard segments or micro-phase separation to form domains due to incompatibility and immiscibility of hard and soft segments. Thermoplastic polyurethane (TPU) and poly-ether-block-amide (PEBA) elastomers are a class of TPEs. In typical TPU elastomers, hard segments are created by the reaction of a diisocyanate with low molecular weight diols, yielding hard segments with urethane groups. In PEBA elastomers, hard polyamide segments are connected to soft segments through ester groups.

Despite the fact that TPEs including TPU and PEBA elastomers have found use in a variety of nonwoven applications since their introduction, the literature describing their nonwoven processing and use has been limited to the patent literature. **[2-7]** Hence, in this work, we investigate the relationship between the polymer characteristics, processing conditions and web properties in melt-blowing. Melt-blowing is a unique nonwoven process where hot, high velocity air streams elongate the polymer melt extruded from a row of nozzles to very fine fibers, which are deposited on the collector to produce web substrates. **[1]** Because the molten polymer is attenuated by the air flow until reaching the collector within microseconds, the resultant fiber properties and fiber formation process depend strongly on the interaction between processing conditions and polymer characteristics.

The degree of attenuation and solidification attained when the newly formed fiber contacts with the others already on the collector will depend on the distances traveled between the die and the collector (DCD), polymer extrusion and air temperatures, and the crystallization behavior of the polymer. The crystallization behavior of TPEs is complex and controls the polymer properties through the morphology established during processing and solidification. Thus, in order to optimize the melt-blowing process and obtain webs with better properties, it is critical to understand the correlation between the polymer crystallization behavior and processing conditions.

Three different hardness grades of polyether and polyester based TPU and poly (tetramethylene oxide) glycol (PTMO) based PEBA copolymers have been studied: (1) BASF Elastollan® Ether TPU series (Shore A): 1180A10, 1190A16, and WY5352D-1; (2) BASF Elastollan® Ester TPU series (Shore A): C78A15, and C95A10; and (3) Arkema Pebax® series (Shore D): 2533, 3533, 5533. In both ether and ester TPU elastomers studied, the hard segment chemistry is based on 4, 4'-diphenylmethane diisocyanate (MDI) and 1, 4-butanediol (BDO), while that of PEBA is polyamide 12. **[8-15]** The isothermal crystallization kinetics of these polymers was measured by DSC. The kinetic parameters were derived from two different models: (1) the traditional Avrami analysis, and (2) the analysis of Kurajica et al. **[16]**. Because the exposure time of the polymer melt to the heated air is determined by the air flow field and the distances traveled between the die and the collector (DCD), the air temperature and velocity profiles used in processing these elastomers were measured on-line for various DCDs. The web tensile properties were measured and explained in terms of the crystallization kinetics along with the temperature profile of the process air.

Finally, the web elastic properties were measured to understand the effect of polymer composition and hardness grade.

II. LITERATURE REVIEW

II. 1. Thermoplastic Elastomers

Thermoplastic elastomers (TPE) represent a unique class of polymers as they combine processing characteristics of thermoplastics (plastics) at high temperature and physical properties of elastomers (rubbers) at room temperature. Thermoplastic polyurethane (TPU) and polyether-block-amide (PEBA) TPEs studied are semi-crystalline block copolymers that display inherent characteristics of two-phase morphology as a result of micro-phase separation: hard (crystalline) and soft (amorphous) phases, as shown in Figure 1. **[1, 17]** These elastomeric copolymers owe their unique plastic and elastic attributes to their two-phase morphology, which governs the processing conditions and resultant product properties. While the amorphous soft segments provide rubber-like properties, hard segments crystallize when cooled below their crystallization point, thereby building a thermally reversible crystalline network that acts as physical crosslinks. This network structure introduces mechanical properties similar to those of cross-linked elastomers. Unlike chemically, irreversible crosslinking in vulcanized rubbers, these physical crosslinks break upon heating such that these copolymers become a homogeneous flowing melt with thermoplastic characteristics. The ratio of the hard and soft segments governs the bulk properties of these polymers, often characterized by the Shore hardness. **[8-15, 18]**

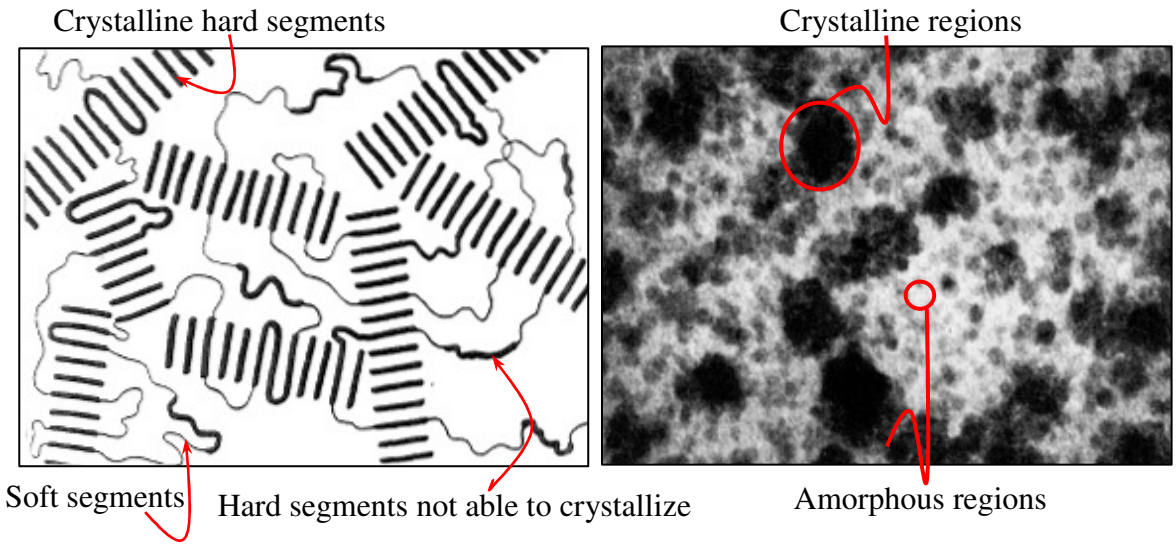

Figure 1: Two-phase morphology in thermoplastic elastomers: crystalline (hard segments) and amorphous (soft segments) regions **(a)** schematic **(b)** TEM

In typical TPUs, hard segments are created by the reaction of a diisocyanate with low molecular weight diols as chain extender, yielding hard segments with urethane groups. 1,4 butanediol (BDO) is the most commonly used chain extender since it exhibits more favorable molecular fit due to its chain linearity, thereby promoting crystallinity of the hard segments. Isocyanates can be either aromatic such as 4,4'-diphenylmethane diisocyanate (MDI), toluene diisocyanate (TDI) or aliphatic such as hexamethylene 1,6-diisocyanate (HDI), isophorone diisocyanate (IPDI). Typically aromatic diisocyanates are preferred and the most widely used one is MDI. In polyether and polyester TPUs studied, the hard segment chemistry is based on 4, 4'-diphenylmethane diisocyanate (MDI) and 1, 4-butanediol (BDO). The soft segments are typically polyether or polyester polyols and connect hard segments as shown below: **[8, 9]**

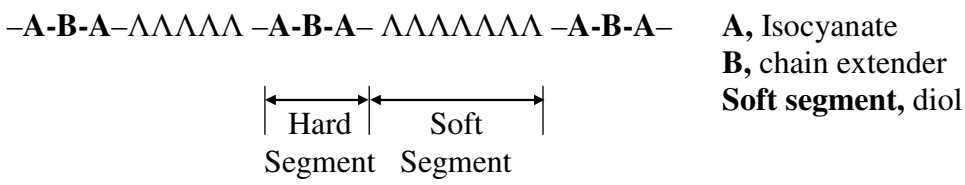

The molecular weight of the polyether or polyester segments is generally in the range of 600 to 4000. Among available polyether soft segments, poly (tetramethylene oxide) glycol (PTMO) yields the best mechanical properties partially due to linear chain structure regularity and ability to crystallize upon extension. **[8-15, 18]**

In early 1980s, Arkema (formerly Atochem) introduced thermoplastic polyether-block-amide elastomer systems (PEBA) under the tradename PEBAX. **[8, 19]** The general structure of these systems is:

HO- [O(C)-**PA**-O(C)-O-**PE**-O]$_N$ –H

where PA is hard polyamide segments connected to soft polyether (PE) segments through ester groups. The molecular weight of the PE segments is generally in the range of 400 to 3000, while the molecular weight of the PA segments ranges from 500 to 5000. Due to a wide variety of polyamides (PA 11, 12, 6, 66…) and polyethers (PTMO, PPO, PEO...) available, PEBA elastomers have a broad spectrum of properties. **[8, 13, 18]** PEBA series studied here consists of PA 12 hard segments and poly (tetramethylene oxide) glycol (PTMO) soft segments.

It is well established that the morphology of semicrystalline block copolymers depends strongly on the interaction between two self-organizing mechanisms: crystallization of hard segments and microphase separation to form domains due to incompatibility and immiscibility of hard and soft segments.

In TPU and PEBA block copolymers, crystallization occurs through association of hard segments via hydrogen bonding between urethane and amide groups, respectively. **[20, 21]** Domain formation and microphase separation in block copolymers depend on how crystallization proceeds. Microphase separation may precede crystallization from disordered melt or crystallization may drive microphase separation from disordered melt when block incompatibility is small. Depending on the strength of segregation, degree of cooling, glass-transition temperature of the amorphous segments, and competition between crystallization and diffusion rates, crystallization may proceed within the preexisting domains or it may destroy existing microphase separated domains. **[10, 20]** When block copolymers crystallize from a single-phase melt, their crystallization behavior is similar to homopolymers. In this case, crystals can grow freely and aggregate to form macroscopic structures such as spherulites since there are no existing domains to restrict the crystal growth. However, in strongly phase separated melts, crystal growth is restricted in one direction since crystallization is confined to microdomains. This leads to nanoscale crystal structures. These morphological differences affect the crystallization kinetics. When crystallization drives microphase separation either from homogeneous melt or by destroying an existing domain structure, the Avrami model describes the characteristic sigmoidal crystallization kinetics at early stages of isothermal crystallization. For crystallization isolated to domains, crystallization will follow first-order kinetics along with very small Avrami n values ($n<1$). **[22-28]**

Many earlier studies investigating the morphology of block copolymers consisting of crystalline hard and flexible amorphous soft segments have been reported.

In a series of morphological studies of ether-ester copolymers, *Wegner et al.* **[29-31]** observed formation of spherulitic crystals in the amorphous matrix, which was similar to the crystallization of homopolymers rather than microphase separation as observed in block copolymers. *Ho et al.* **[32]** suggested spherulitic crystallization of hard segments with no macro phase separation in ether-ester block copolymers. *Seymour et al.* **[33]** and *Xu et al.* **[14]** proposed a model of spherulitic crystallization for ester-urethane copolymers where microphase separation occurs only into crystalline and amorphous regions. In these models, incompatibility of hard and soft segments drives association and crystallization of hard segments rather than microphase separation into hard and soft domains. In a study of nanophase separated Pebax 3533 and Pellethane TPU 70A with AFM *McLean and Sauer* **[15]** observed larger crystals in PEBA than in TPU 70A. They described crystallization in PEBA as crystallization driven phase separation, while in TPU crystallization was restricted to hard domains which had already phase separated. **[34]**

II. 2. Crystallization Kinetics of Multi-Block Thermoplastic Polymers

A variety of models have been developed to describe the crystallization kinetics of semi-crystalline polymers under isothermal quiescent conditions. **[16, 35]** Among these, the Avrami model has been the most commonly used to describe the kinetics of the primary crystallization stage of isothermal crystallization, which includes primary nucleation and growth of the crystal units until their impingement, followed by the secondary crystallization stage. At a given crystallization temperature, the degree of phase transformation i.e. relative crystallinity, $X(t-t_0)$, is related to time t by the Avrami equation: **[36]**

$$X(t-t_0)=\frac{Xc_t}{Xc_\infty}=1-\exp\left(-k(t-t_0)^n\right) \quad (1)$$

where Xc_t and Xc_∞ are the amount of crystallinity at time t and at infinite time, respectively. k is the crystallization rate constant; n is the Avrami exponent; and t_0 is the time at the onset of crystallization. Assuming that the relative degree of crystallinity increases with crystallization time, equation (1) can be used to analyze isothermal crystallization. The crystallization rate constant, k is a function of the nucleation and growth rates and depends on the polymer properties and the temperature. The Avrami exponent, n provides information on the number of dimensions in which growth takes place (growth geometry) and on the nucleation process. According to the original assumptions of the theory, the Avrami exponent, n ranges between the positive integers 1 and 4. **[36-38]**

The Avrami kinetic parameters are usually determined by taking double logarithm of equation (1):

$$\log[-\ln(1-X(t-t_0))]=n\log(t-t_0)+\log k \quad (2)$$

The rate constant, k and Avrami exponent, n are obtained by plotting the $\log[-\ln(1-X(t-t_0))]$ against the $\log(t-t_0)$. The value of y-intercept gives *log(k)* while n is just the slope of the least-square line. **[11]**

Even though the traditional Avrami method is commonly accepted for the analysis of isothermal crystallization kinetics of polymers, it has well known shortcomings. The Avrami equation is only valid for crystallization levels where no impingement of crystal units occurs, i.e. at short crystallization times.

Because the crystallization onset, t_0 is typically determined visually on the DSC isothermal crystallization exotherm, the calculation of the relative crystallinity, $X(t-t_0)$ by integrating the DSC data inherently involves errors. In addition, the double log form of the Avrami plot may result in superficially good fits for the experimental data, and thus the derived kinetic parameters may not give a true representation of the crystallization process. **[32, 38]** Although this does not mean that the derived Avrami parameters are invalid, the evaluation of the crystallization kinetics based only on the Avrami analysis may be misleading. Among many studies attempting to improve the Avrami analysis, *Kurajica et al.* **[16]** proposed a different approach for analysis of isothermal crystallization DSC data. They took the derivative of the Avrami equation and fit the untransformed DSC data directly to this function. In their equation, they replaced k of the Avrami equation by k^n. Thus, they represented the heat flow dq/dt measured by DSC as follows:

$$\frac{dq}{dt} = \Delta H \frac{d\alpha}{dt} = \Delta H n k^n (t-t_0)^{n-1} \exp\left(-k^n (t-t_0)^n\right) \quad (3)$$

where ΔH is the enthalpy of crystallization and $d\alpha/dt$ is the change in the amount of crystalline material with time. One advantage of this approach is that dq/dt is obtained directly from the DSC data, while the traditional Avrami analysis requires transformation of the DSC data from differential to integral form, which makes this traditional method very sensitive to errors. It is also worth noting that k in the Kurajica analysis has units of 1/time while in the traditional Avrami analysis, k has units of 1/time^n.

II. 3. Melt-blowing Process

Ever since Wente introduced a method to produce fine fibers from thermoplastic materials **[39]**, the melt-blowing process has been studied and used in producing nonwovens. In the melt-blowing process, polymer melt is extruded from a row of fine capillaries along the center of the die. Once it exits the die, very high velocity heated air impinges on the polymer melt and the resultant drag force attenuates the molten polymer into fine fibers having diameters in the range of 1-20 microns within microseconds. These fibers are then deposited on the collector to produce web substrates. Melt-blowing process is depicted in Figure 2. **[4]**

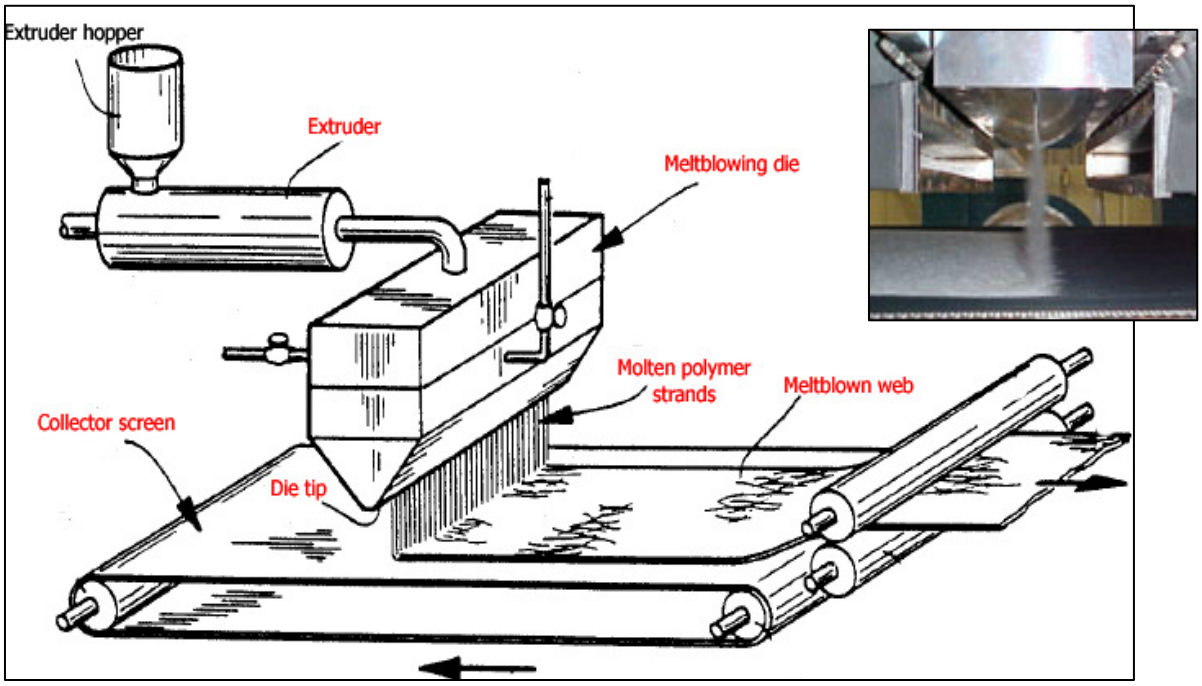

Figure 2: Melt-blowing process

Because the polymer melt is extruded directly into the hot air jet streams, the fiber formation process and properties depend on the air flow field, which in turn depends on the die configuration. The exposure time of the polymer melt to the heated air is determined by the

air velocity profile and the distances traveled between the die and the collector (DCD). Since melt-blowing typically produces self-bonding nonwoven structures that derive their strength from fiber to fiber contacts, the ability of the fiber to stick to other fibers already on the collector is critical. Thus, while the profiles of polymer and air temperatures along with flow rates are important in fiber formation, the rate of heat transfer or cooling of polymer melt and the degree of fiber solidification attained on the collector will also depend on distances traveled between the die and collector (DCD) and crystallization behavior of the polymeric material. **[40]**

Temperature and velocity profiles of the air flow produced from melt-blowing dies of various configurations having single or multiple polymer nozzles have been experimentally studied and empirically modeled in the literature. Because the melt-blowing die used in our study is a dual air slot type, the literature focusing on this die type will be reviewed briefly. Harpham and Shambaugh **[41, 42]** reported that air velocity and temperature profiles of a blunt melt-blowing die are primarily a function of the distances downstream and across the die for both isothermal and non-isothermal jets. They also showed that the flow field below a melt-blowing die that has a large aspect ratio (air slot length-to-width ratio) can be approximated as a 2-D flow field and the end effects at the center plane are negligible. In another study, Bansal and Shambaugh **[43]** showed good agreement between measured fiber diameters and profiles of centerline air temperature and velocity. They found that the polymer and air temperatures dropped rapidly within the first 1.5 cm below the die, where most of the fiber attenuation occurs. Thereafter, they reach a plateau at $DCD = 4\ cm$ suggested to be due to polymer crystallization. Shambaugh and coworkers **[44-49]** studied the effect of die angle,

geometry (blunt and sharp nose pieces) and positioning of the nose piece (inset, flash, and outset). They showed that sharp die tip configuration is aerodynamically superior to blunt die and provides higher centerline air velocities but increased air turbulence at any point below the die. At the same air flow rates, with increasing die angles the two symmetric air jets converging from the sharp dies were found to merge to the maximum velocity at farther distances below the die, produce lower centerline velocities, broader temperature profiles, and slower fiber attenuation rates.

III. EXPERIMENTAL

III.1. Materials

Melt-blown webs were produced on the North Carolina State University (NCSU) Nonwoven Cooperative Research Center's melt-blowing line from thoroughly dried (1) BASF Elastollan® Ether TPU series: 1180A10, 1190A16, and WY5352D-1; (2) BASF Elastollan® Ester TPU series: C78A15, and C95A10; and (3) Arkema Pebax® series: 2533, 3533, 5533. Within Table 1, and throughout this manuscript, ester and ether TPU's are denoted as *Sxx* and *Txx*, respectively, where xx represents Shore A hardness. Likewise, the polyether-block-amides (PEBA's) are referred to as *Pxx*, where xx represents Shore D hardness. These elastomers were chosen to span similar hardness ranges across all of the materials studied.

III.2. Melt-blowing Process Conditions

The melt-blown webs were produced on the 0.56m (22 inches) pilot-scale melt blowing line at the Nonwovens Cooperative Research Center, NCSU.

Table 1: Melt-blowing Process Conditions

Sample ID			Die Temp. (°C)	Air Temp. (°C)	Air Flow Rate (%)	Polymer Mass Flow Rate (Ghm)†
Ether Elastollan® TPU	1180A10	T80	233	222	70	0.5
	1190A10	T90	251	238	70	0.5
	Wy5352d	T98	261	249	70	0.5
Ester Elastollan® TPU	C78A15	S78	253	234	70	0.5
	C95A10	S95	262	261	50	0.5
PEBA (Pebax®)	2533	P25	287	258	25	0.24
	3533	P35	305	267	20	0.24
	5533	P55	312	274	20	0.24

Ghm†: grams per hole per minute

The line consists of a 0.76 m (30inches) wide slot die with a single row of 535 polymer capillaries having 0.381 mm diameter with a density of 25 holes/inch, 50 mm (2.0 inch, 24:1) extruders and melt pumps. Air flow rates corresponding to 20-25% and 50-70% of the pump speed were used in melt blowing PEBA and TPU polymers, respectively. The processing conditions employed during melt-blowing of these polymers are shown in Table 1. Die-to-collector distances (DCD) of 14 cm (5.5 inches), 20 cm (8 inches), and 30.5 cm (12 inches) were used to produce melt-blown webs of approximately 100 g/m^2 at polymer mass flow rates of 0.24 g/hole/min and 0.5 g/hole/min for PEBA and TPU polymers, respectively. The polymer mass flow rates used are representative of commercial melt-blowing production rates. The polymer extrusion (die) temperatures were adjusted for each polymer type and grade to maintain the die pressures in the range 450-550 psi, the acceptable range for an efficient melt-blowing process on this apparatus.

III.3. Melt-Blowing Air Velocity and Temperature Measurements

Process air temperature and velocity profiles were measured online with a K-type thermocouple and a T2-600 cylindrical pitot tube (Hotek Technologies) connected to HD2134P.2 Digital Manometer Thermometer (Hotek Technologies) with full-scale readings of 0.01 mbar – 1 Pa differential pressure and 2 - 210 m/s velocity range. The data collected was processed with Deltalog 9 (Hotek Technologies) software. The pitot tube and thermocouple probe were mounted on a three-dimensional framework such that they were oriented parallel with the direction of air flow i.e. parallel to *z*-axis to minimize flow disturbance. The set up permitted x, y, and z motions within the flow field in 1.6 mm increments.

Figure 3 shows a cross-section of a typical slot type melt-blowing die used in this study. **[50]** This type of die is referred to as a sharp-edged, inset die with a recession of a = 1.524 mm and 45° angle between the plane of the air slots and the die face. This means the dual air jets will intersect and impinge upon the polymer melt exiting the capillaries at an angle of 45° from two sides of the single row of nozzles. The air gap widths were d = 1.524 mm, the air slot width b = 0.63 mm, the distance between the outer edges of the air slots is h = 1.263 mm ($h = 2b$), and the overall length of the air slot was l = 737 mm. Since the aspect ratio l/b = 1168 is significantly larger than 50, the flow field of the dual, converging air jets from the melt-blowing line used in this study can be assumed to be 2D at positions below the die center and free of end effects. **[41, 42, 51]** All air temperature and velocity measurements were measured at positions in the center plane of the die.

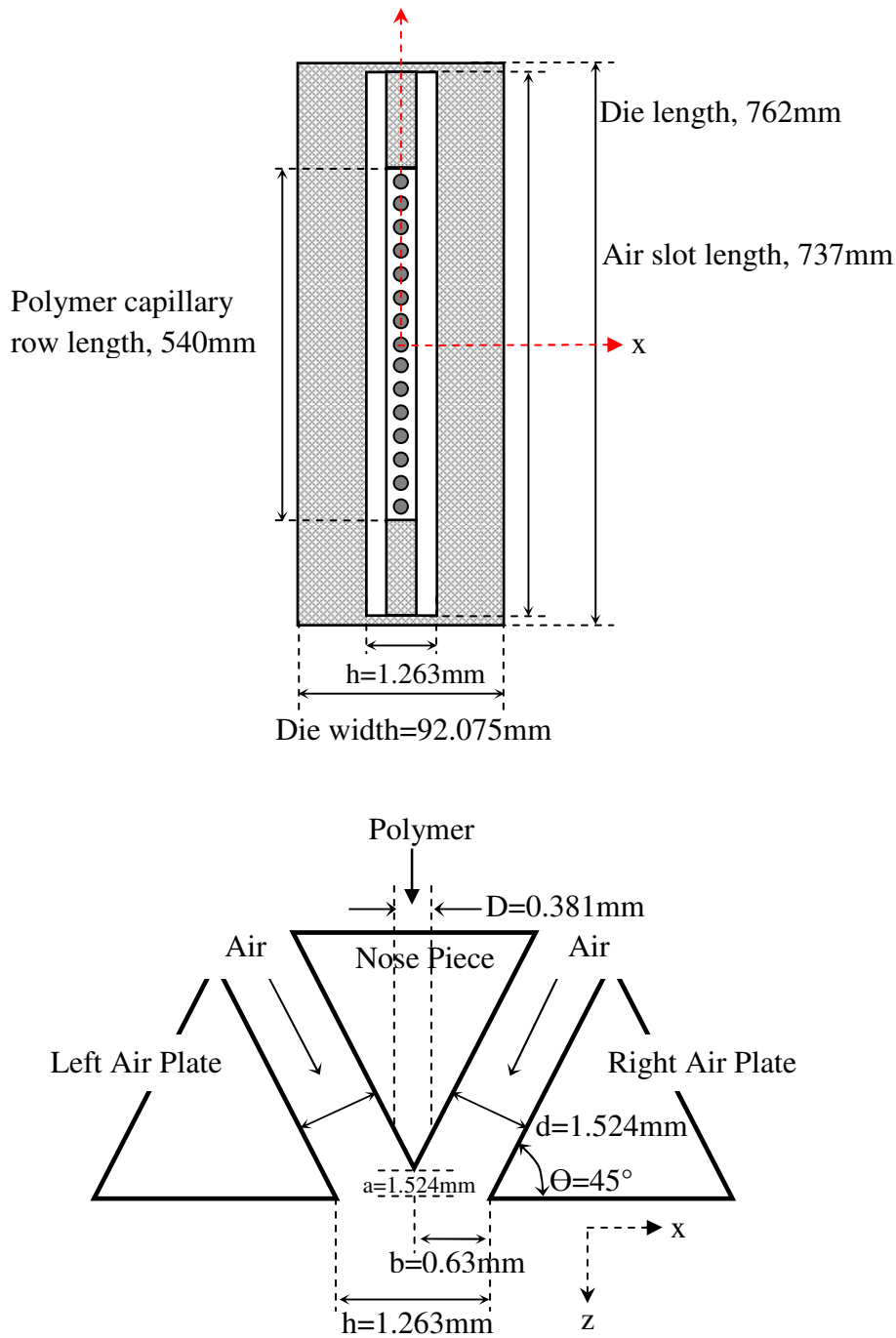

Figure 3: A cross-sectional view of **(a)** melt blowing die face, the z-axis (not shown) is perpendicular to the plane of the drawing, and **(b)** 45° sharp, inset melt blowing die, the y-axis (not shown) is perpendicular to the plane of the drawing (drawing is not to scale)

The coordinate system used in this work is also shown in Figure 3. All coordinates are relative to the die face. Its origin is at the center of the die face, i.e. at the tip of the nosepiece for the measurement of the air velocity and temperatures. The *y*-direction (CD-cross direction) is parallel to the air slots, while the *x*-direction (MD-machine direction) is across the die face and parallel to the ground. The positive *z*-direction (not shown) is perpendicular to the die face i.e. downward direction below the melt-blowing die. I.e. coordinates of $x = y = z = 0$ means the center tip of the melt-blowing die, while $x = y = 0$ and $z = 1\ mm$ means 1 mm below the melt-blowing die or DCD = 1 mm. At each level, the axial velocity and temperature profiles of the process air were measured as a function of axial position, *z* (DCD) and horizontal position, *x*. Across the die face (*x*-direction) horizontal steps of 1.6 mm were used for positions $-3.17 < x < 6.35$ mm. For vertical positions near the die face ($0 < z < 96.5$ mm), the data was collected at z increments of 5 mm, while for positions farther below the die ($z > 96.5$ mm), fewer measurements needed to be made. (For positions 96.5 mm $< z <$ 137 mm and $z > 137$ mm, vertical steps of 10 mm and 25 mm were used, respectively) This is mainly because the changes in data were much more gradual at larger distances. **[42,44]** To approximate the processing conditions used in melt-blowing as shown in Table 1, the die temperature was 260°C, while the air temperatures were 260°C and 315°C at air flow rate corresponding to 50% of the pump speed. Measurement of the air flow field profiles beyond 50% of the pump speed was not possible since the air velocities exceeded the upper limit of the pitot tube. This velocity limit, however, is sufficiently high to cover all regions of operation in the melt-blowing process, as described by Shambaugh et al. **[52]**.

The selected air velocities for ether and ester TPU series fall within Region II and III, which produces fiber diameters in the range of 0.1μm–10μm. Even though fiber vibrations are significant in this high air velocity region, we assume during attenuation the polymer path coincides with the direction of the axial component of the air velocity at the centerline. For PEBA series, on other hand, the air velocities correspond to those classified under Region 1 and produce melt-blown webs having fiber diameters in the range of 10μm–20μm. The temperature and velocity profiles of the air were measured in the absence of polymer flow.

III.4. Characterization of Melt-Blown Webs

III.4.1. Thermal Analysis

Thermal analysis (heating DSC scans provided by BASF and Arkema) for both polymer pellets and melt-blown webs was carried out using Universal V4.1D TA Instruments for ester TPU and PEBA series, and Universal V3.8B TA Instruments for ether TPU series. The heating and cooling temperatures were in the range of -50°C/-90°C to 250°C at a heating rate of 20°C/min, for ester and ether TPU series, respectively, while from -80°C/-140°C to 220°C at a heating rate of 10°C/min for PEBA series. Solution viscosity data was provided by Arkema and BASF.

III.4.2. Isothermal Crystallization Kinetics

III.4.2.1. Differential Scanning Calorimeter

A Perkin Elmer Diamond differential scanning calorimeter (DSC) was used to detect the thermal transitions and follow the heat flow from the web samples during isothermal

crystallization from the melt.

The DSC equipped with internal liquid nitrogen cooling unit reliably provided a cooling rate up to 50°C min^{-1}. At higher cooling rates, it was observed that the collected data was unreliable due to the initial instability of the DSC program vs. sample temperature. Temperature calibration was performed using an indium standard (T_m =156.6°C and ΔH=28.5 Jg^{-1}). All DSC scans were carried out under nitrogen atmosphere and each sample was used only once to reduce degradation. Web samples of 3-5 mg were placed in open DSC pans, vacuum-dried at 60°C for 3 hrs, and kept in desiccators until just before loading into the DSC. **[32,37]** To observe the crystallization exotherm and determine the onset of crystallization, web samples were first heated to temperatures 40-50°C above their peak melting temperature at 20°C min^{-1}, maintained at this temperature for 3 min to ensure complete melting, then were cooled to 25°C at 10°C/min. **[54]** The initial isothermal crystallization temperature was chosen by adding 5°C-10°C to the observed onset of crystallization temperature as seen in Table 2.

Table 2: DSC Crystallization Temperatures and Test Conditions

Sample ID		**T_m** (°C)	**Crystallization T_{onset}** (°C)	**Crystallization T_{peak}** (°C)	**DSC Isothermal Crystallization**	
					Melt Temp. (C)	Crystallization Temp. Range (C)
Ether TPU	T80	146.5	79.1	71.2	195	89-93.5
	T90	165	106.2	99.3	210	110-120
	T98	183.3	118.4	112.9	225	130-146
Ester TPU	S78	158.1	81.0	71.8	215	88-93.5
	S95	196	113.2	107.7	225	124-134
PEBA	P25	135	90.1	81.6	180	84-92
	P35	142	98.6	91.1	180	96-110
	P55	161	133.8	126.8	200	138-143

Isothermal crystallization kinetics from the melt was determined as follows. Melt-blown web samples were melted at temperatures 40-50°C above their peak melting temperature at heating rates of 20°C min^{-1}, held there for 3 min, then cooled at 50°C min^{-1} to the designated crystallization temperature, T_c, and maintained at that temperature for 10 min until crystallization was complete. The heat flow generated as a function of time during the isothermal crystallization was recorded and analyzed according to the typical procedure to obtain relative degrees of crystallinity, $X(t-t_0)$:

$$X(t-t_0) = \left(\frac{A_t}{A_\infty}\right) \quad \text{.....(4)}$$

where t_0 is the time at which the web sample attains stable isothermal conditions, which is assumed to correspond to the crystallization onset. A_t is the cumulative area under the exotherm from time t_0 to time t and A_∞ is the total area of the crystallization exotherm at long times.

III.4.2.2.Optical Polarizing Microscope

The morphology of the meltblown webs was observed by using Metaltek Instruments Carl Zeiss optical polarizing microscope with a Mettler model FP82HT hot stage and a Diagnostic Measurements, 0.6X, HRP060-CMT camera. Meltblown web samples produced from P55, T98 and S95 were sandwiched between two microscope cover glasses, melted at 200-225ºC for 3 min and then rapidly cooled to the crystallization temperature at a rate of 10°C/min. Morphology development was recorded during crystallization.

III.4.3. Mechanical Properties

III.4.3.1. Tensile Properties

Tensile properties were measured using an Instron tensile tester and a dogbone sample with gage lengths of 63.5 mm (2.5") and 114 mm (4.5") for PEBA and TPU systems, respectively. The dogbone sample shape was determined by ASTM D 638-03 (type III & IV) for PEBA systems, while that of TPU systems was ASTM D638 (type III). The test conditions were modified from ASTM 3776 so as to give the same extension rate for the dogbone samples as for the straight sided samples of method ASTM 3776. Thus the crosshead speed was set at 132 mm/min for the 63.5 mm gage dogbone and 228 mm/min for the 114 mm gage dogbone specimen. Elongation to rupture measurements were based on the elongation of the narrow section of the sample. The actual % elongation of the narrow section of sample was found to be 17% and 58% larger than instrumental elongation for TPU and PEBA series, respectively.

III.4.3.2. Elastic Properties

Tensile set and elastic limit at various elongations were measured at room temperature using Zwick tensile tester. Since there is no standard method available, 1x6 inch strip samples were stretched to three different strains-50%, 75% & 100%-at a crosshead speed of 4 inches min^{-1} and initial gage length of 4 inches. At these strains, samples were held for a fixed length of time, t=60sn and allowed to return to original gage length (zero stress) at a crosshead speed of 500mm min^{-1}. The sample was removed and held in relaxed position for t=60sn. The retracted length of the sample was measured and % tensile set was recorded as a percentage of the initial length by using the following formula:

$$\% \text{ Tensile Set} = \left(\frac{\text{Recovered Length} - \text{Initial Length}}{\text{Initial Length}} \right) \times 100 \quad \ldots\ldots\ldots\ldots\ldots\ldots\ldots\ldots\ldots\ldots\ldots(5)$$

Elastic limit was extrapolated from the regression fit of % tensile set plotted as a function of given extensions.

III.4.4. Fiber Orientation Distribution

Five transmitted light optical microscopy images were obtained randomly for each web sample and analyzed by NCRC Image Analysis software for fiber orientation distribution analysis. The software performs a Fast Fourier Transform to measure the orientation distribution. The results are illustrated as mean dominant angle of orientation and frequencies of orientation angles. **[55]**

III.4.5. Fiber Diameter Distribution

Scanning Electron Microscopy (SEM) images were obtained for each melt-blown web sample and 50 diameter measurements were obtained using NCRC Image Analysis software. **[56]**

IV. RESULTS AND DISCUSSION

IV. 1. Melt-blowing Process

Melt-blown web structures from ester TPU, ether TPU and polyether-block-amide (PEBA) were produced with three different hardness grades after adjusting the the process parameters as discussed below. In melt-blowing of ether and ester TPU, and PEBA elastomers, several

processing difficulties were encountered. During extrusion of these polymers within the recommended processing temperature range, die pressures approached 60-75bar due to their high molecular weight and melt viscosity. Extremely high die pressures led to unstable processing and extensive polymer dripping at the die exit, possibly leading to shot formation that sometimes manifested itself in the form of semi-molten polymer chunks on the web and poor web formation. To bring the melt viscosity down into the acceptable range for melt-blowing, thereby relieving intense die pressures, the extrusion temperatures were increased. It is well known that the urethane groups in these systems are not thermally stable and can easily undergo thermal degradation during melt processing. **[57]** Hence, in some cases, increasing melt temperatures well above the recommended temperature ranges seen in Table 1 led to polymer degradation. The high molecular weight of the polymers used, in particular ester TPU and PEBA series, was believed to cause large die swell on exiting the spinneret. This led to adjacent fibers to fusing and forming large shot, as the accumulated polymer broke free from the spinneret face plate. In addition, the attenuating air caused extreme fiber breakage and many short fibers were blown away rather than depositing onto the belt, commonly referred to as fly formation. In order to achieve long fibers with little or no breaks and eliminate poor web formation, the attenuating air was reduced from 70% to 50% for ester TPU series, and to 20% for PEBA series. Reduced attenuating air flow rates, however, are believed to increase the chance of semi-molten individual fibers coming in contact with each other before reaching the belt, possibly leading to rope formation. For PEBA series, the throughput was reduced from 0.5ghm to 0.24ghm, and the quench air was turned off.

Solution viscosities of the pellets and melt-blown webs produced from PEBA and TPU elastomers were analyzed to understand the degree of polymer degradation during melt-blowing process. In comparison to original pellet solution viscosities, the viscosity values of the melt-blown web samples were found to decrease by 11-45% for PEBA series, 6-25% for ester TPU and 21-26% for ether TPU series. This was more pronounced with increasing extrusion temperatures. This clearly suggests that the high processing temperatures used to relieve the die pressures in melt-blowing PEBA and TPU elastomers caused significant molecular weight degradation. The degradation was more pronounced in ester TPU series. The S85 grade of ester TPU series could not be melt-blown within the available time allocated for the trials.

IV. 2. Thermal Analysis

Heating DSC data and scans of the PEBA, ether and ester TPU pellets and melt-blown webs processed at different DCDs and extrusion temperatures are shown in Tables 3-4 and Figure 4. Because the DSC data and heating profiles of the melt-blown webs processed at different DCDs were almost identical, the values shown in Tables 3-4 are averaged over the DCD range. And, DSC heating scans in Figure 4 for the pellets are also representative of the melt-blown webs regardless of the DCD.

From Tables 3-4, comparison of transition temperatures and associated melting enthalpies of melt-blown webs at studied DCDs to those of pellets suggest that melt-blowing process does not affect thermal behavior of ether and ester TPU series, but affects T_{m2} of PEBA series.

Table 3: DSC heating scans and data for PEBA elastomers

Sample	T_g (°C)	T_{m1} (°C) (T_{mPE})	$T_{m\ PA}$ (°C)		
			T_{m2}	T_{m3}	ΔH_3 (J/g)
P25					
Pellet	***	7.6	70.9	137.1	14.6
Web	-76.43	6.5	57.9	134.9	22.8
P35					
Pellet	***	4.6	90.7	143.5	22.9
Web	-77.7	4.6	59	140.9	25.3
P55					
Pellet	***	***	87.8	160.8	47.6
Web	***	***	59.4	160.8	44

Table 4: DSC heating scans and data for ester and ether TPU elastomers

Sample		Tg (°C)	T_{mhard} (°C)			ΔH_{hard} (J/g)
			T_{onset}	T_{m1}	T_{m2}	ΔH_2
Ester TPU	S78	-48.4	53.2	***	156.7	17.8
	S85	-48.5	120.9	***	159.5	22.1
	S95	-37.8	129.5	***	195.9	29.3
Ether TPU	T80	***	26.7	73.8	146	31.7
	T90	***	28.2	73.3	165.2	29.3
	T98	***	30.2	72.6	183.8	41.5

As seen in Table 3, for both pellets and melt-blown webs, the glass transition temperature ($T_{g,\ PE}$) is around -77˚C, higher than the PE homopolymer (-84˚C), while T_m of the hard PA segment appears to be lower than the homopolymer PA (180˚C). This suggests the presence of hard segments in the soft matrix and imperfection of the hard crystalline structures. The two distinct melting endotherms observed in Figure 4 (c) at lower (T_{m1}) and higher temperature (T_{m3}) ranges indicate the existence of two crystalline phases: soft and hard crystalline melting at T_{m1} and T_{m3}, respectively. **[58,59]** A number of studies suggested melting of crystalline structures having different thickness or sizes, or imperfection of hard crystalline domains as possible explanations for T_{m2} and T_{m3}. **[13,18,19]**

Figure 4: Heating DSC scans of **(a)** ether TPU, **(b)** ester TPU, **(c)** PEBA webs

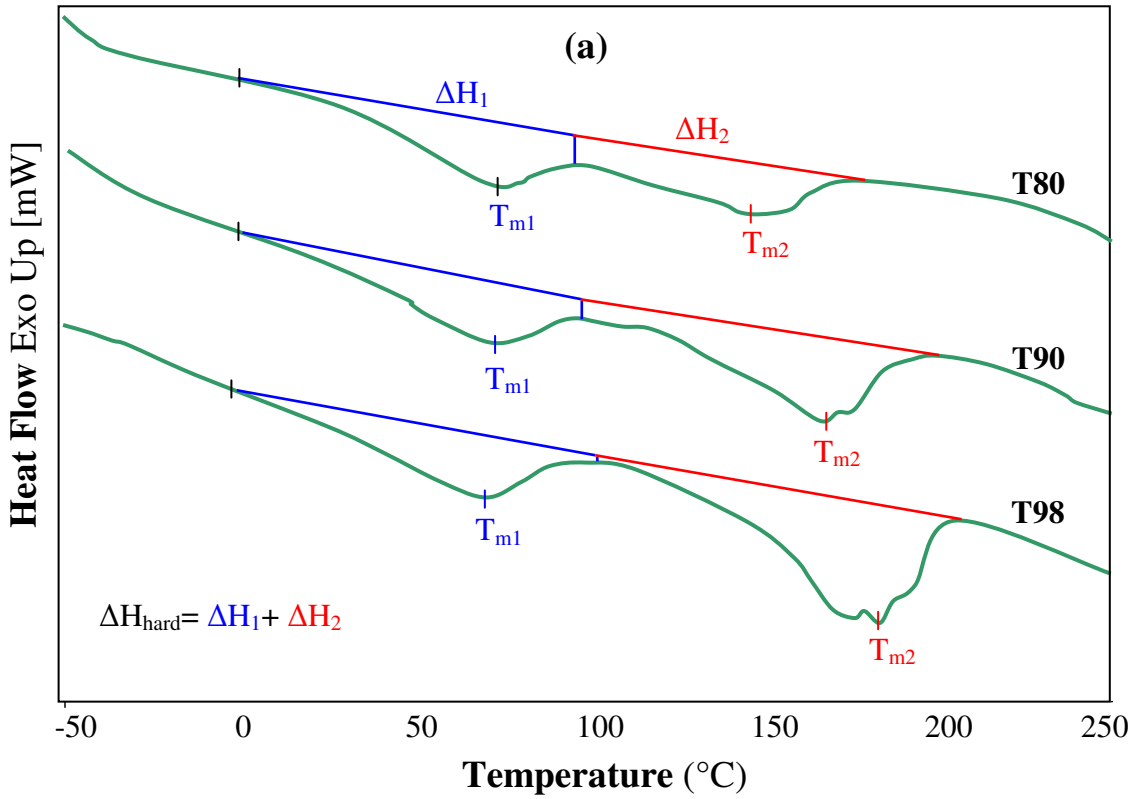
(a)
ΔH1
ΔH2
T80
Tm1
Tm2
T90
Tm1
Tm2
T98
Tm1
Tm2
ΔHhard= ΔH1+ ΔH2
Heat Flow Exo Up [mW]
-50
0
50
100
150
200
250
Temperature (°C)

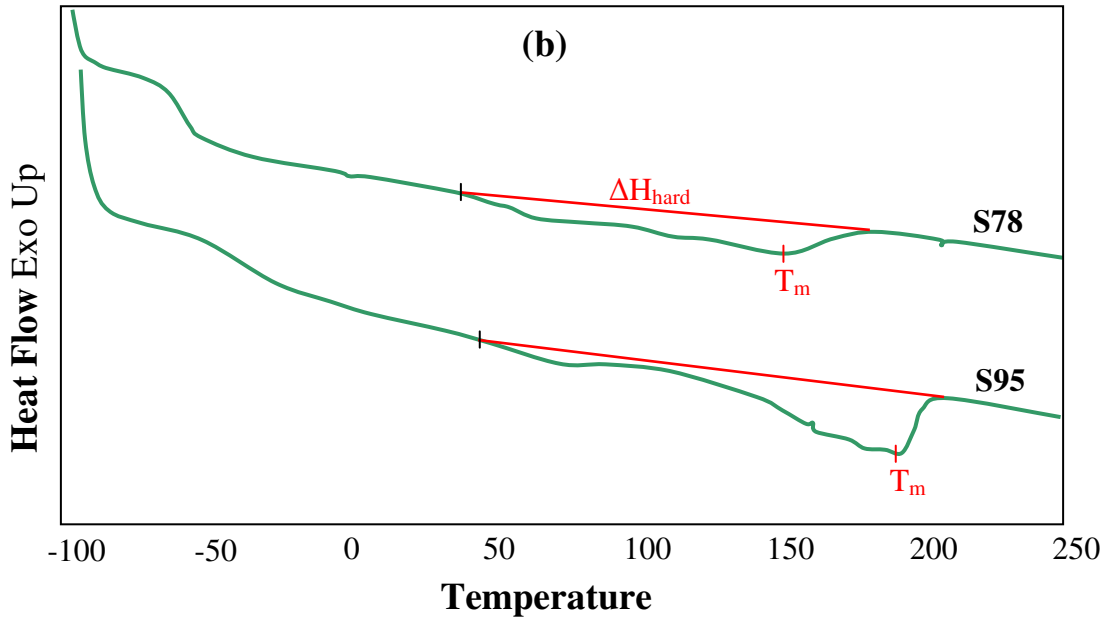
(b)
ΔHhard
S78
Tm
S95
Tm
Heat Flow Exo Up
-100
-50
0
50
100
150
200
250
Temperature

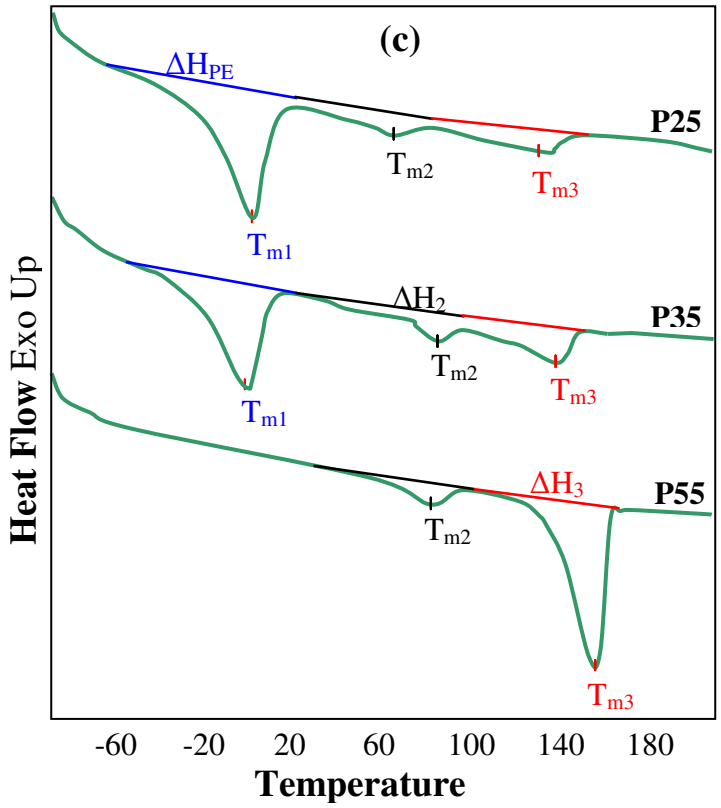

As for TPU elastomers seen in Figure 4 (a) and (b), two endotherm peaks were detected in ether TPU series while a relatively broad melting endotherm is observed in ester TPU series. The presence of a broad melting endotherm for ester TPU and two melting endotherms for the ether TPU suggests the imperfection of the hard crystalline structures. **[8, 60]** Multiple endotherms detected in ether TPU series can also be attributed to melting of hard segments with differing degrees of order. **[61-63]**

As expected, the area of the soft melting endotherm is the largest in the softest grades i.e. P25, T80 and S78, and decreases with increasing hard segment content until it diminishes. The area of the hard melting endotherm becomes larger with increasing hard segment content

in the order of P55>P35>P25 in PEBA, S95>S85>S78 in ester and T98>T90>T80 in ether TPU series. The hard crystalline melting peak, also, shifts to higher temperatures with increasing hard segment content. Various studies suggested that T_m and crystallinity of the hard segments depends mainly on the block length and content. With increasing hard segment content, average length of the crystallizable hard segments increases. This promotes hydrogen bonding between polar amide and urethane groups in PEBA and TPU series, respectively. This results in the formation of larger and more ordered hard crystalline structures, thereby enhancing the crystallinity and higher melting temperatures. **[13, 19, 63-67]**

IV. 3. Isothermal Crystallization Kinetics

The desired isothermal crystallization temperatures were determined from cooling crystallization exotherms by adding 5-10°C to the temperature of the onset of crystallization. The isothermal crystallization temperature ranges and the maximum temperature at which the melt was held (melt temperature) for TPU and PEBA melt-blown webs are shown in Table 2. As expected, melting and crystallization peaks as well as onset of the crystallization shift to higher temperatures with increasing amount of crystallizable component i.e. increasing Shore hardness. Thus, the crystallization temperature, T_c, follows the order of P55>P35>P25 for PEBA, S95>S78 for ester TPU, and T98>T90>T80 for ether TPU. The experimental measurements are limited by the DSC instrument resolution. If the crystallization is very slow, the amount of heat evolved per unit time or the crystallization exotherm is too small to be observed within the sensitivity of DSC.

In contrast, at low crystallization temperatures, the crystallization can be too fast and the experimental measurements are limited by the fact that the sample has already crystallized to a significant extent by the time its temperature reached the predetermined crystallization temperature. Figure 5 shows a typical DSC crystallization exotherm for isothermal crystallization of the melt-blown web, T98 at T_c =130°C after complete melting at 225°C for 3 min. Crystallization is assumed to begin at point A where t_0 = 0.778 min, which is preceded by a short time period during which the temperature of the web sample reached isothermal crystallization conditions and crystallization begins. The exothermic heat flow increases until reaching a maximum at point B. Beyond the maximum heat flow, crystallization slows significantly, and no noticeable change in the heat flow is detected after point C. **[68]**

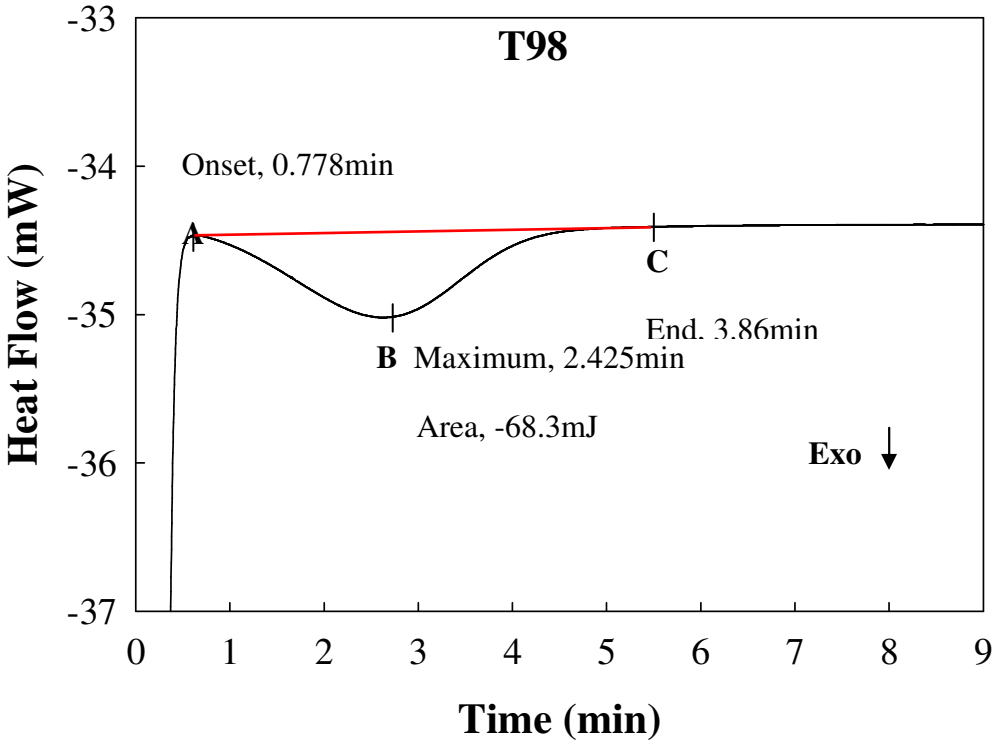

Figure 5: Isothermal crystallization of T98 melt-blown web at T_c=130°C

The rate of heat flow during isothermal crystallization depends strongly on the kinetics of the crystallization process, which is very sensitive to crystallization temperature. This is illustrated in Figure 6, where crystallization exotherms of web T90 at several crystallization temperatures are plotted. It is clearly observed that at higher crystallization temperatures the crystallization maxima shift to longer times and become flatter. This means that the time to reach the ultimate degree of crystallinity becomes longer and the crystallization rates decrease due to the decrease in the degree of cooling ($T_{melting\ \ point}$-$T_{crystallization}$). The crystallization exotherms of the other polymers studied are not shown here since all exhibited similar temperature dependency.

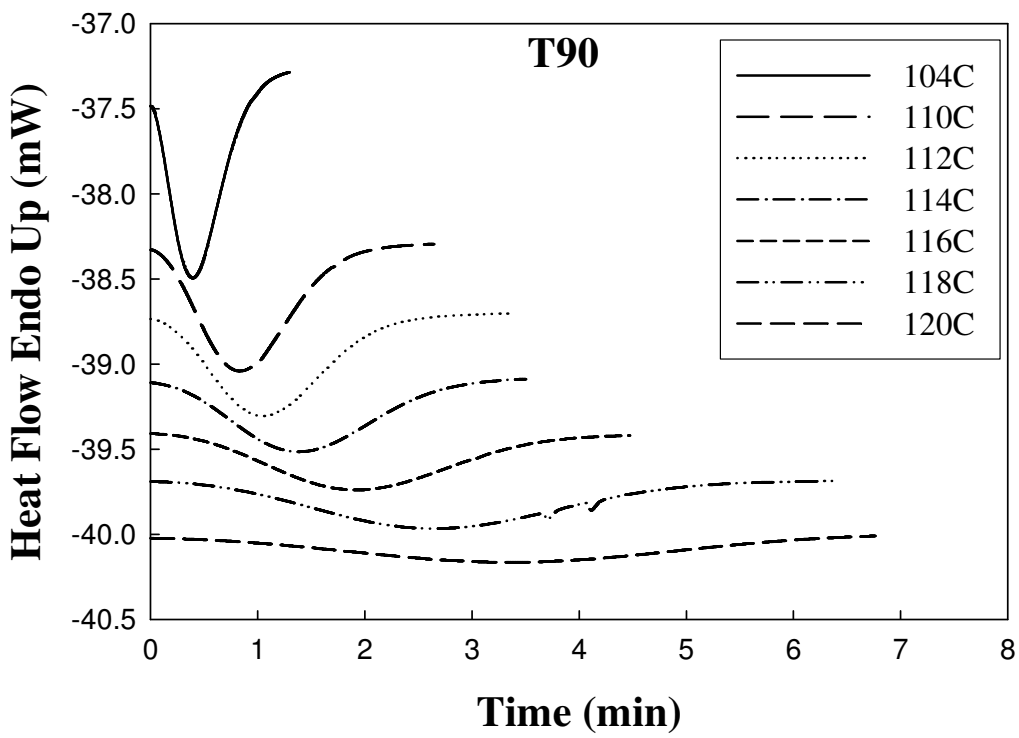

Figure 6: Isothermal crystallization of T90 melt-blown web at several T_c

Figure 7 shows the development of relative crystallinity $X(t-t_0)$ with crystallization time for PEBA series. It can be seen that all exotherms exhibit characteristic sigmoidal behavior and the curves shift to longer times with increasing crystallization temperatures. The relative crystallinity vs. crystallization time plots of ether and ester TPU systems are not shown here since all exhibit similar sigmoidal dependence.

The double logarithmic Avrami plots of $\log[-\ln(1-X(t-t_0))]$ vs. $\log(t-t_0)$ are shown in Figure 8. As observed from the plots, experimental DSC data fit the Avrami model only for the initial portion of the crystallization process, beyond which deviations from the model are observed as changes in the slope. This is in agreement with the literature suggesting that the Avrami model is valid only for the early stages of the crystallization process. Therefore, in order to obtain Avrami kinetic parameters, k and n, the experimental data at low transformations of the crystallization are used, corresponding to around $X_c < 30\%$ for soft and medium grades and $< 10\%$ for the hardest grades. **[38, 69]**

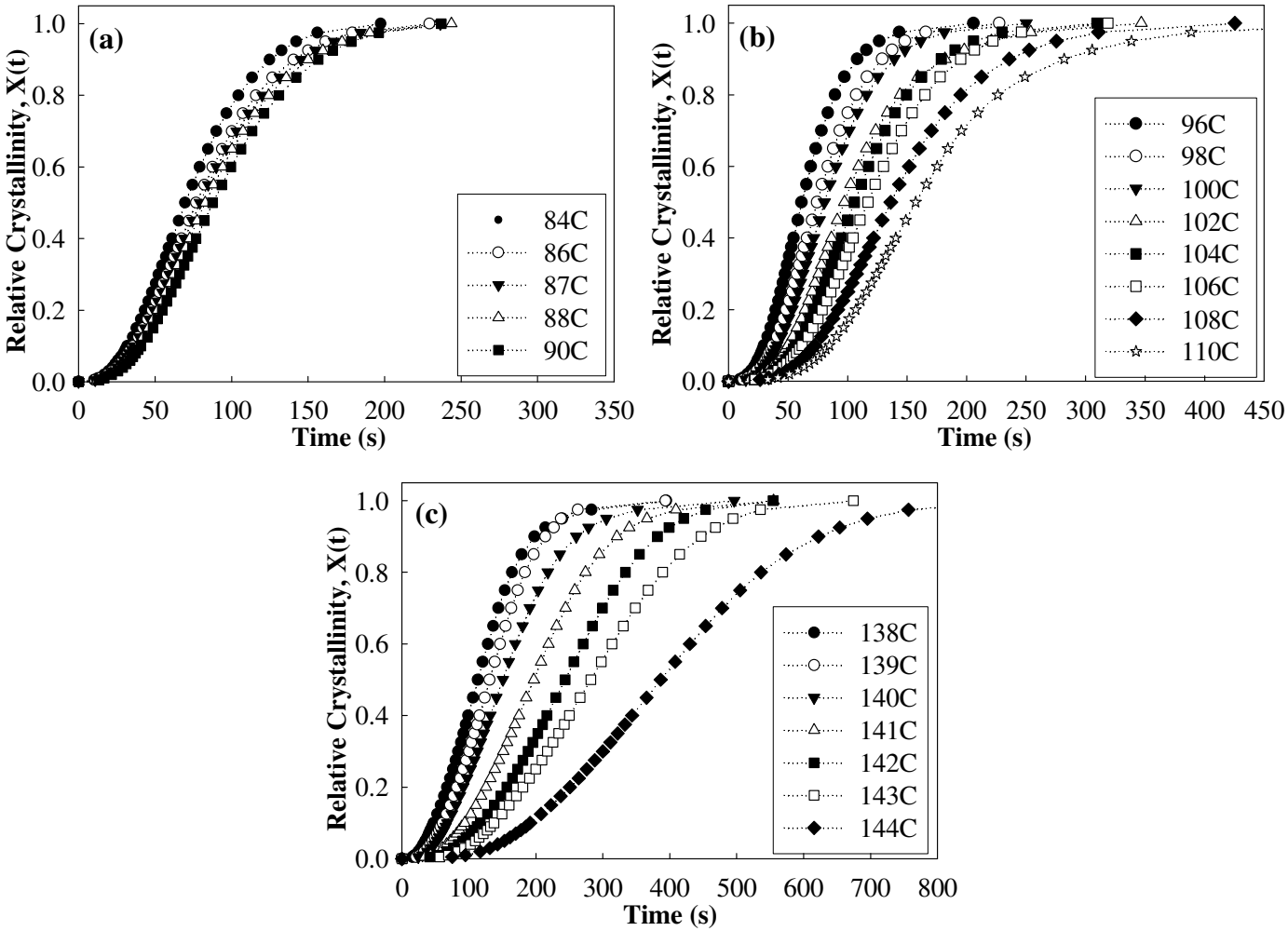

Figure 7: Relative crystallinity $X\ (t\text{-}t_0)$ vs crystallization time **(a)** P25, **(b)** P35 **(c)** P55

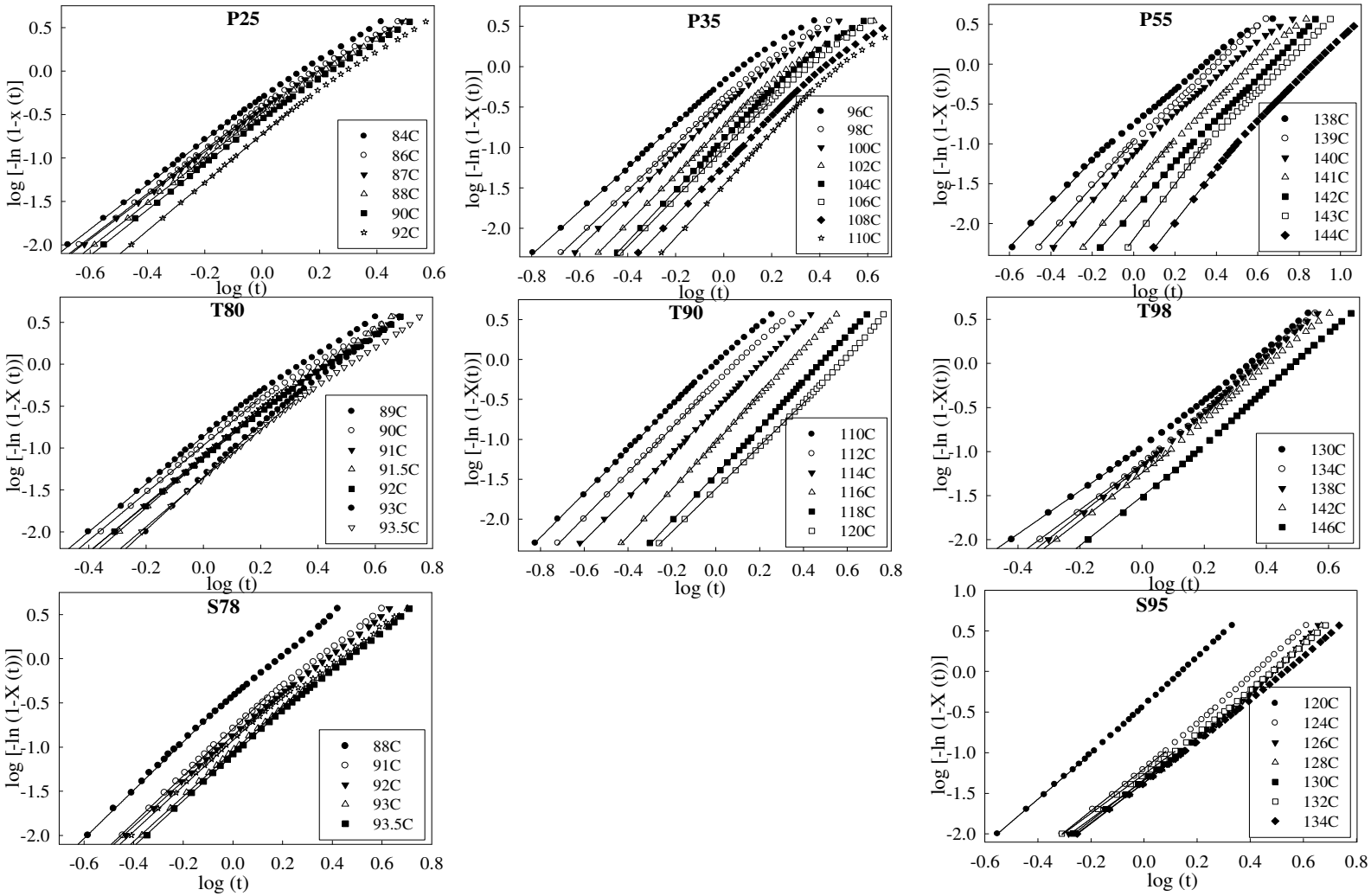

Figure 8: Avrami double logarithm plots from dried samples

The values of the crystallization kinetics parameters determined from the DSC heat flow data using traditional Avrami analysis in equation (2) plotted against those derived from the Kurajica model in equation (3) are shown in Figure 9. A linear correlation between the n-parameters (Figure 9a) obtained from both models is observed indicating that both methods give similar values. However, n obtained from the Avrami fit tends to be larger than that obtained from the Kurajica model. In Figure 9b, the Avrami k^{-n} value is plotted against the k value from the Kurajica model. This approach accommodates the different definitions used for k in equation (1) and equation (3). There is a linear dependence of the value of k determined from fitting equation (3) to the DSC data with the value of k^{-n} derived from the Avrami fit, except those of P55, which lie above the line relating these parameters (see Figure 9b). However, the value of k^{-n} derived from the Avrami fit is smaller than the value of k obtained from the Kurajica model. This is clearly demonstrated in Figures 10 & 11, which illustrate the Avrami exponent, n and crystallization rate, k plotted as a function of polymer type and hardness as well as isothermal crystallization temperatures. Both the Avrami n and crystallization rate, k values obtained by the integrated and untransformed DSC data are consistent and comparable. As described earlier, in traditional Avrami analysis, the crystallization rate, k is obtained from the double logarithmic plot of $\log[-\ln(1-X(t-t_0))]\text{vs.}\log(t-t_0)$, where k is the anti-logarithmic value of y-intercept. Thus, the value of k is very sensitive to errors in correctly determining the crystallization onset, t_0 and relative crystallinity, $X(t-t_0)$ from the DSC isothermal crystallization exotherm.

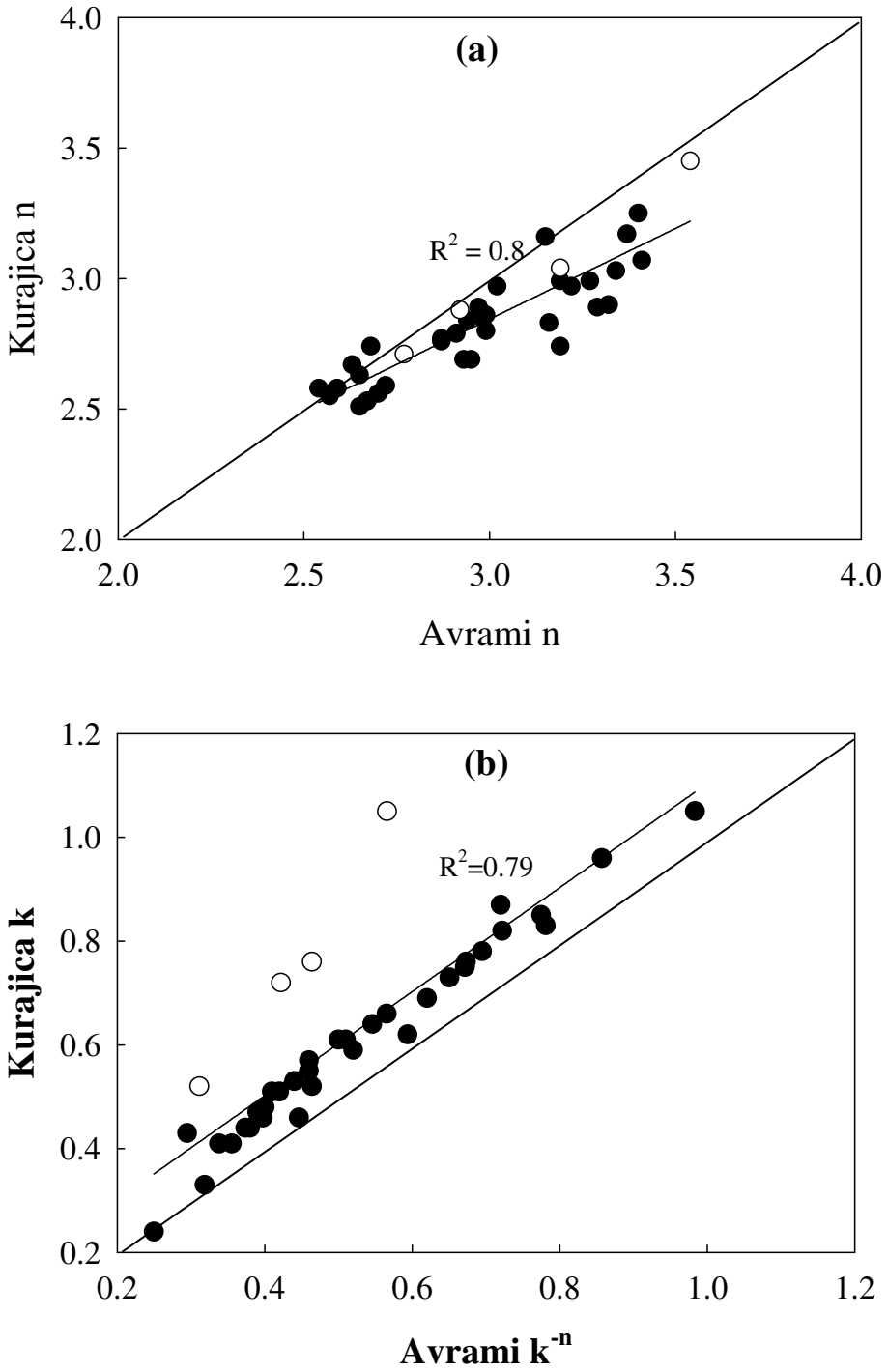

Figure 9: Comparison of kinetic parameters obtained from Avrami model in Eqn. (2) vs. derivative Kurajica model of the Avrami Equation as in Eqn. (3), **(a)** Avrami exponent *n*, **(b)** Kurajica and Avrami crystallization rate *k* and , k^{-n} respectively. Hollow circles represent P55.

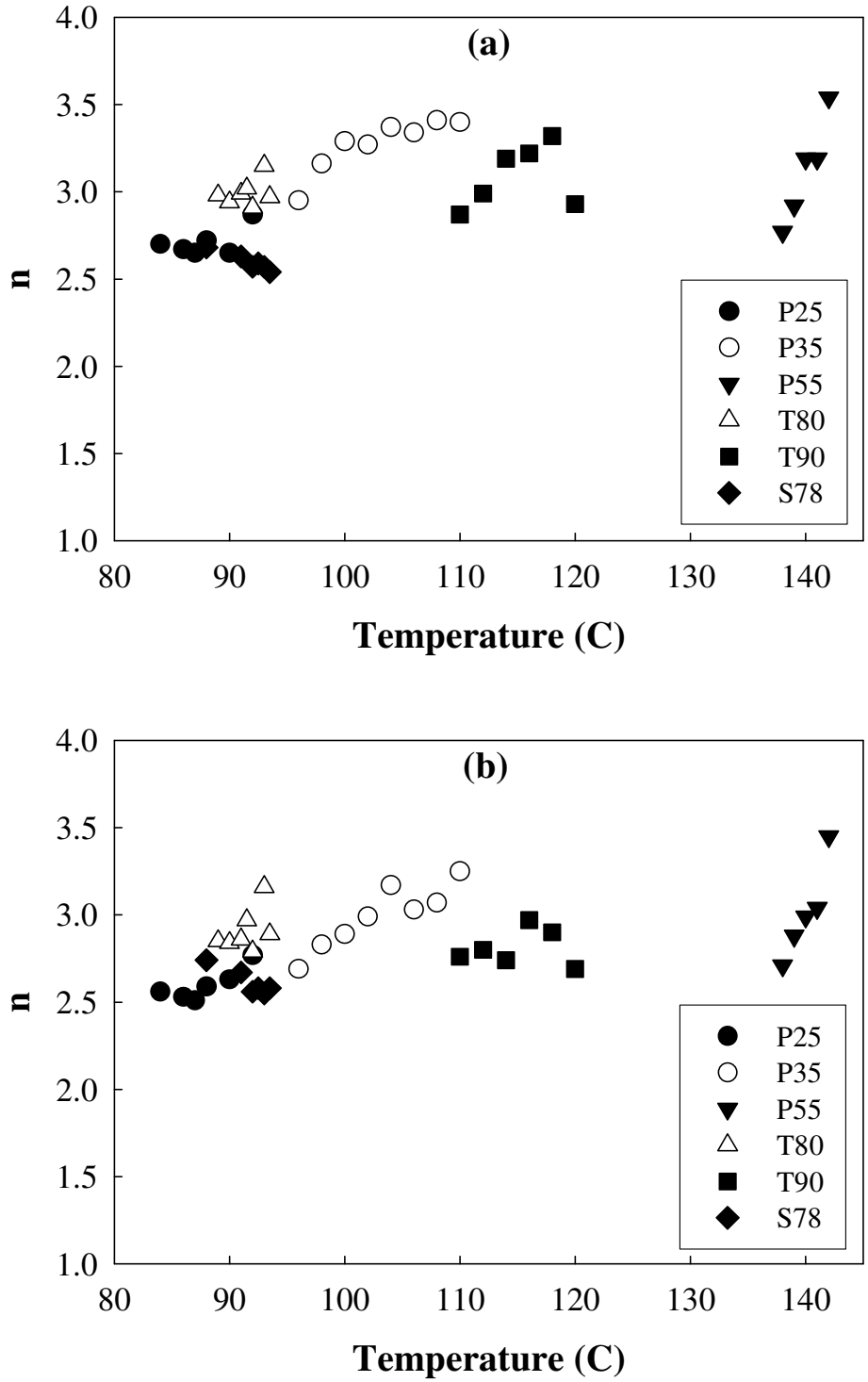

Figure 10: Avrami exponent *n* against crystallization temperatures obtained by **(a)** Kurajica and **(b)** Avrami models; Sample P25●, P35○, P55▼; T80Δ, T90■; S78♦

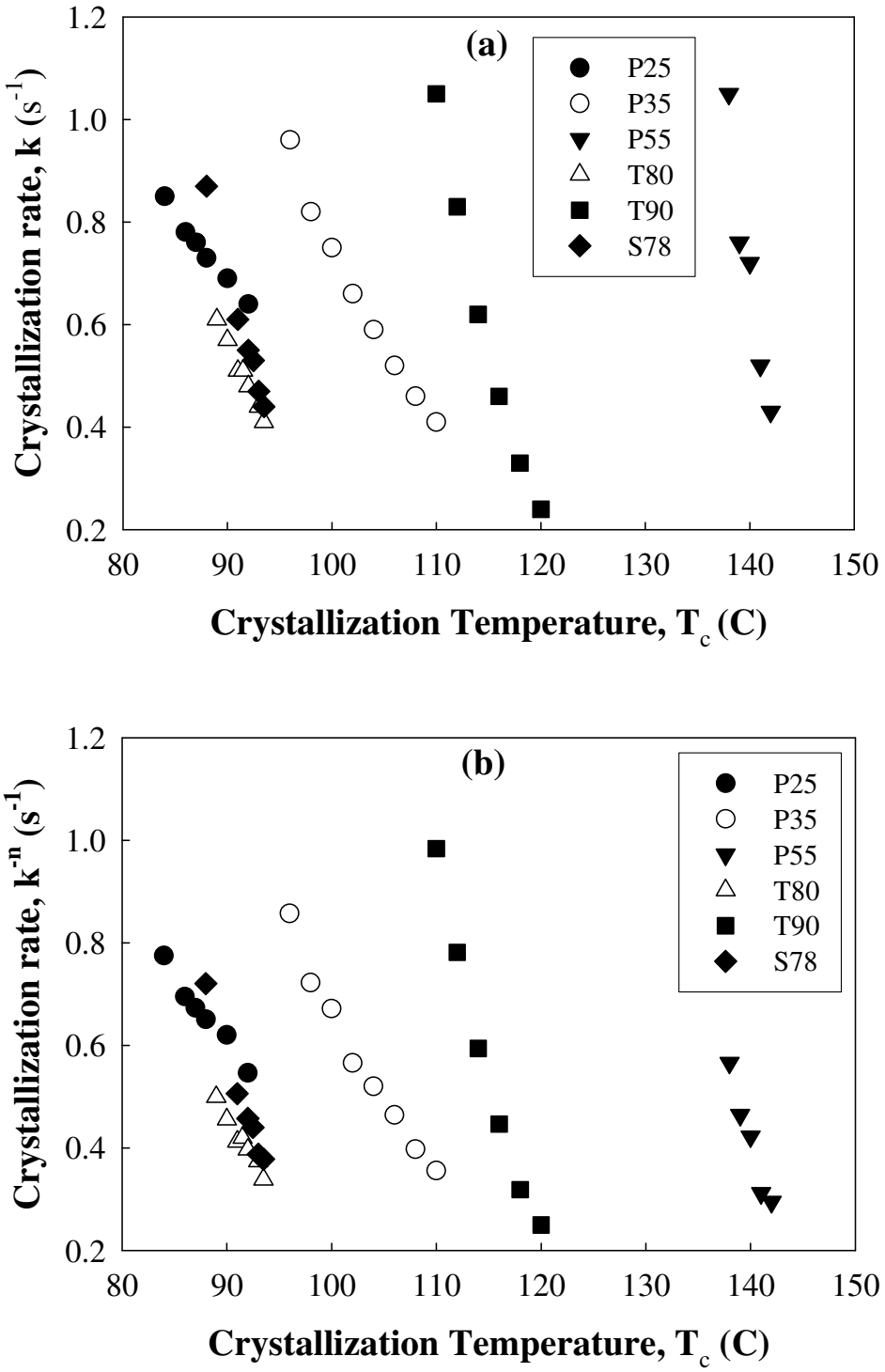

Figure 11: Crystallization rate, (a) *k* against crystallization temperatures obtained by Kurajica and **(b)** k^{-n} against crystallization temperatures obtained by Avrami models; Sample P25●, P35○, P55▼; T80Δ, T90■; S78♦

Table 5: Kinetic parameters for isothermal crystallization of melt-blown samples obtained by Kurajica model

T80							
Tc (°C)	**89**	**90**	**91**	**91.5**	**92**	**93**	**93.5**
N	2.98	2.94	2.99	3.02	2.91	3.15	2.97
K (min^{-1})	0.61	0.57	0.51	0.51	0.48	0.44	0.41
$\mathbf{t_{1/2}}$ (min)	1.45	1.55	1.73	1.74	1.84	2.02	2.16
T90							
Tc (°C)	**110**	**112**	**114**	**116**	**118**	**120**	
N	2.87	2.99	3.19	3.22	3.32	2.93	
K (min^{-1})	1.05	0.83	0.62	0.46	0.33	0.24	
$\mathbf{t_{1/2}}$ (min)	0.84	1.07	1.44	1.94	2.71	3.68	
S78							
Tc (°C)	**88**	**90**	**92**	**92.5**	**93**	**93.5**	
N	2.68	2.63	2.57	2.59	2.57	1.54	
K (min^{-1})	0.87	0.61	0.55	0.53	0.47	0.44	
$\mathbf{t_{1/2}}$ (min)	1.00	1.43	1.58	1.64	1.84	1.97	
P25							
Tc (°C)	**84**	**86**	**87**	**88**	**90**	**92**	
N	2.7	2.67	2.65	2.72	2.65	2.87	
K (min^{-1})	0.85	0.78	0.76	0.73	0.69	0.64	
$\mathbf{t_{1/2}}$ (min)	1.03	1.12	1.15	1.20	1.26	1.38	
P35							
Tc (°C)	**96**	**98**	**100**	**102**	**104**	**106**	**108**	**110**
N	2.95	3.16	3.29	3.27	3.37	3.34	3.41	3.4
K (min^{-1})	0.96	0.82	0.75	0.66	0.59	0.52	0.46	0.41
$\mathbf{t_{1/2}}$ (min)	0.92	1.09	1.19	1.35	1.52	1.72	1.95	2.19
P55							
Tc (°C)	**138**	**139**	**140**	**141**	**142**		
N	2.77	2.92	3.19	3.19	3.54		
K (min^{-1})	1.05	0.76	0.72	0.52	0.43		
$\mathbf{t_{1/2}}$ (min)	0.83	1.16	1.24	1.71	2.10		

Because the approach in equation (3) can directly be fitted to the DSC experimental data, the errors associated with the Avrami model are reduced, allowing more accurate determination of the crystallization rate, *k*. Therefore, we use the Kurajica approach, in the remainder of this study. The values of *k* and *n* obtained from untransformed DSC data by fitting Kurajica

model in equation (3) are shown in Table 5.

Analysis of the secondary crystallization is not considered within this text because the purpose of this research is to understand the effect of crystallization kinetics in melt-blowing process where polymer melt reaches the collector within time scales significantly shorter than the onset of secondary crystallization. As seen in Table 5, for all studied webs, non-integer *n* values were obtained, contradictory to the theoretical expectations of integer values based on the original Avrami assumptions. Earlier studies interpreted non-integer *n* values due to simplified assumptions in the original Avrami equation which may not apply to all polymers under all crystallization conditions, **[70]** the complex nature of crystallization, **[37]** mixed nucleation and/or crystal growth modes, **[11]** variations in crystal growth dimension, **[71]** variation in nucleation and/or crystal growth rates during crystallization, **[72]** development of similar crystal growth structures from different types of nuclei, **[38]** and simultaneous occurrence of two and three dimensional crystal growth. **[69]** As suggested by *Cho et al*. **[72]** non-integer *n* values will be considered as representative of the nearest integer.

Figure 10 shows that the values of *n* do not vary with the isothermal crystallization temperature for polyester and polyether based TPUs or for P25 polyamide TPE. On the other hand, *n* appears to increase with isothermal crystallization temperature for P35 and P55. The values of *n* range between 2.59 and 3.41, which may be rounded of the nearest integer 3. These *n* values of nearly 3 indicate that all webs produced from these polymers have similar nucleation and growth mechanism even under different melting and crystallization conditions. Based on the characteristic sigmoidal crystallization behavior observed in Figure 7 along with *n* values of around 3, for all studied copolymers, the crystallization mechanism

is similar to that of semi-crystalline homopolymers involving formation of macroscopic crystal structures. **[29-33]**

The nature of nucleation and crystal growth, and how crystallization develops from the melt: either from single-phase melt or by destroying existing microphase separated domains was further explored by optical microscopy. Figure 12 shows microscopic images of P55 crystallized at 138ºC from the melt under crossed polarizers and at different times during crystallization. The initial melt conditions were the same as the DSC protocol described in experimental section. Within the resolution of the microscope, no residual crystallites or other structures were observed in the melt state. This observation indicates that crystallization develops from a single-phase melt structure where crystallization dominates the formation of final morphology. Upon reaching the isothermal crystallization temperature, crystal nuclei are observed to form rapidly and grow in size until reaching a constant size as seen in Figure 12 (e) and (f). Some of the crystals impinge against each other but others do not, even after long crystallization times. Due to limited resolution of the microscope, it is difficult to conclude the nature of nucleation and growth modes from the microscopic images.

These results suggest the following nucleation and crystal growth possibilities: (1) three-dimensional crystal growth that nucleates with instantaneous (heterogeneous) nucleation or (2) two-dimensional crystal growth that nucleates with sporadic (homogeneous) nucleation. **[37, 38, 73, 74]** Because crystals appear to be visible around the same time upon reaching the crystallization temperature, three dimensional crystal growth initiated by heterogeneous nucleation is suggested. Also, compared to the time to reach the ultimate crystallinity the

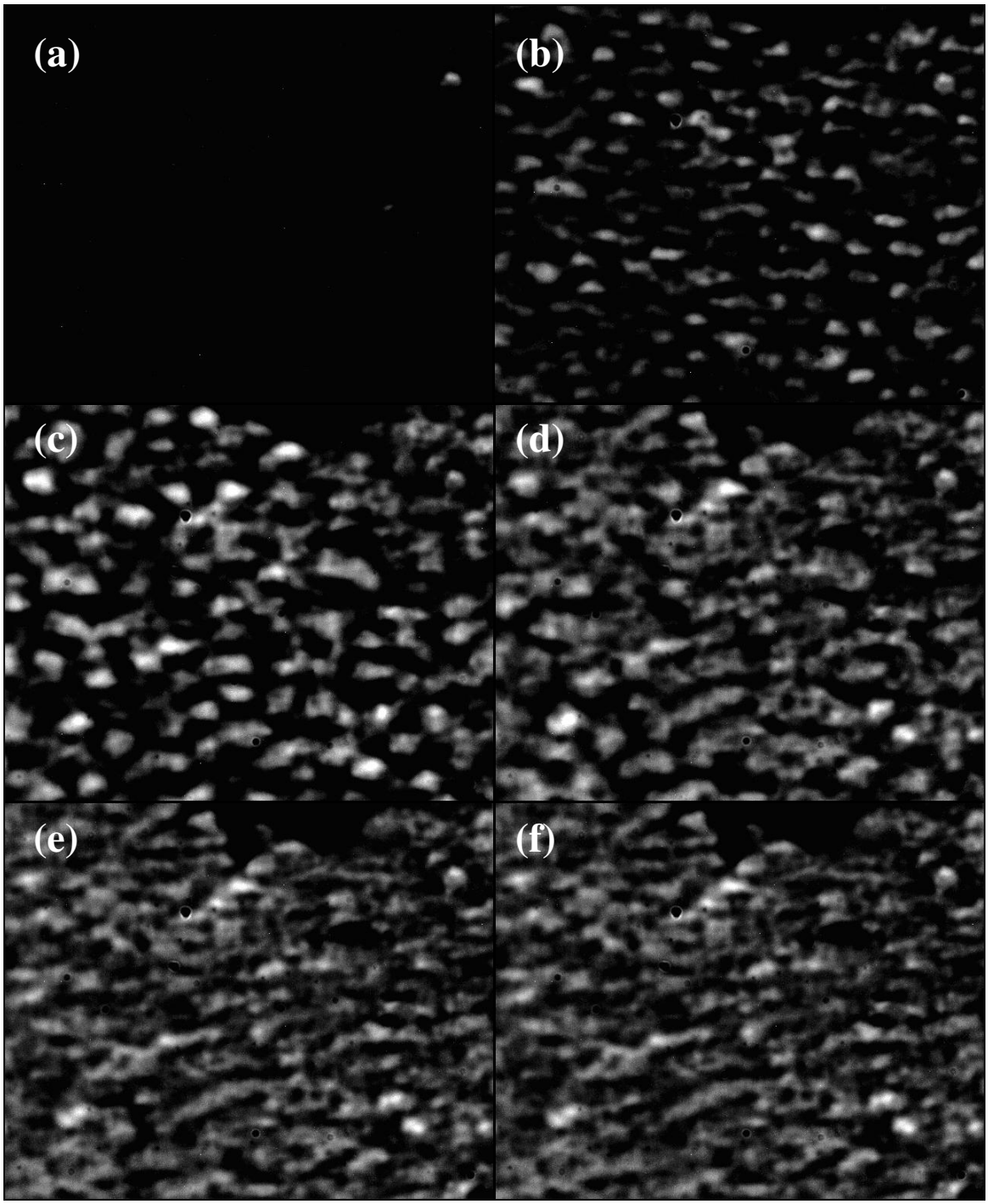

Figure 12: Optical images of the same field of P55 sample melt crystallized at T_c=*138ºC* at crystallization times **(a)** 0 sec, **(b)** 45 sec, **(c)** 90 sec, **(d)**135 sec, **(e)**180 sec, **(f)**225 sec

nucleation time is very short, again indicating heterogeneous nucleation and three dimensional crystal growth, in agreement with earlier studies on block copolymers. **[14, 15, 29-33, 75]**

Similar crystal nucleation and growth were observed for the corresponding hardness grades of ether and ester TPU elastomers (T98 and S95), while crystallites were too small to be observed microscopically for the medium and soft grades of both TPU and PEBA series.

Figure 11a shows the crystallization rate, k plotted against the crystallization temperatures. As expected, the crystallization rate, k decreases with increasing crystallization temperatures, regardless of the polymer type and hardness. Because n values of nearly 3 are relatively independent of the isothermal crystallization temperatures as illustrated in Figure 10, the mechanism of nucleation and crystal growth do not change with increasing crystallization temperatures, at least within the studied temperature ranges. The decrease in the crystallization rate is therefore due to the decrease in the rate of nucleation and crystal growth with increasing crystallization temperatures. This is expected since the energy barrier for nucleation will increase as the crystallization temperatures approach melting temperatures. **[53, 70, 76]**

It is generally considered better to compare the crystallization rate for different polymers at constant difference in crystallization temperature below the melting temperature, i.e. $\Delta T = T_m - T_c$ = constant. This is illustrated in Figure 13 where the crystallization rate, k is plotted as a function of the extent of cooling, ΔT. It is clear from Figure 13 that the extent of cooling required to achieve a given crystallization rate follows the order P55 < P35 < P25 for PEBA series, T98 < T90 < T80 for ether TPU series and S95 < S78 for ester TPU series. Also, at

constant ΔT, the crystallization rate, k, decreases with increasing concentration of non-crystallizable component i.e. soft segment. This means that with increasing amount of crystallizable component i.e. polymer hard segments, the crystallization of the polymer melt becomes faster, and crystallization onset temperatures shift to higher temperatures, but crystallization onset occurs with a smaller extent of cooling.

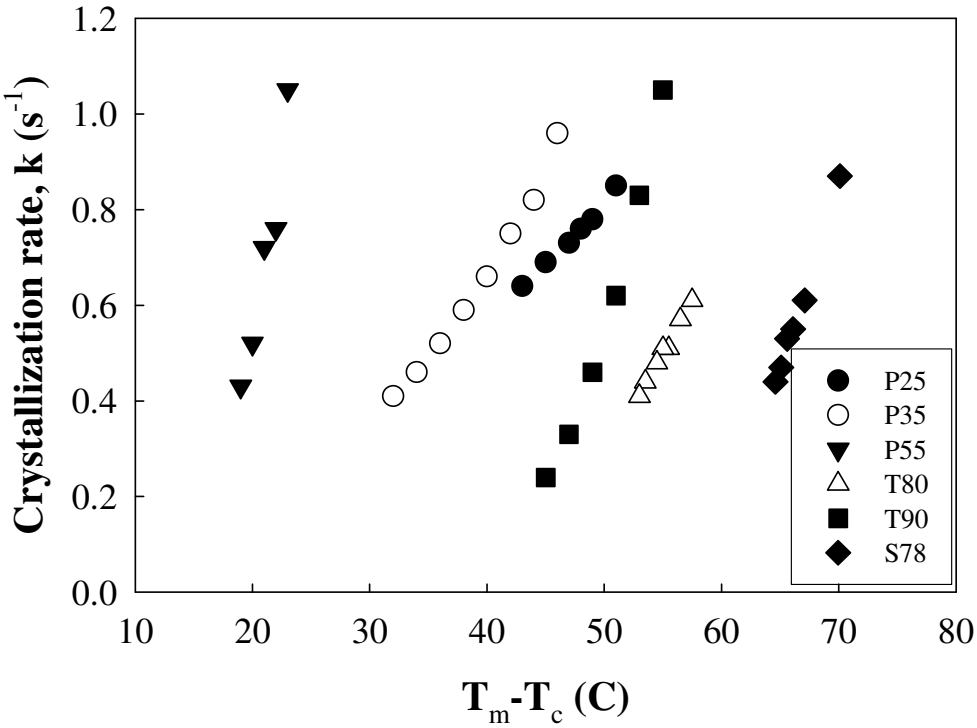

Figure 13: Crystallization rate, k as a function of degree of cooling; Sample P25●, P35○, P55▼; T80Δ, T90■; S78♦

The crystallization half-time, $t_{1/2}$, is defined as the time from the onset of the crystallization until the crystallization is half-completed. Based on the Avrami analysis in equation (1), $t_{1/2}$ is determined from the measured kinetic parameters

$$t_{1/2} = \left(\frac{\ln 2}{k^{-n}}\right)^{1/n} \quad \text{.....} \quad (6)$$

Because we use the Kurajica approach, where k has units of 1/time , the crystallization half-time is defined as follows and plotted as a function of isothermal crystallization temperature in Figure 14.

$$t_{1/2} = \left(\frac{\ln 2}{k}\right)^{1/n} \quad \text{(7)}$$

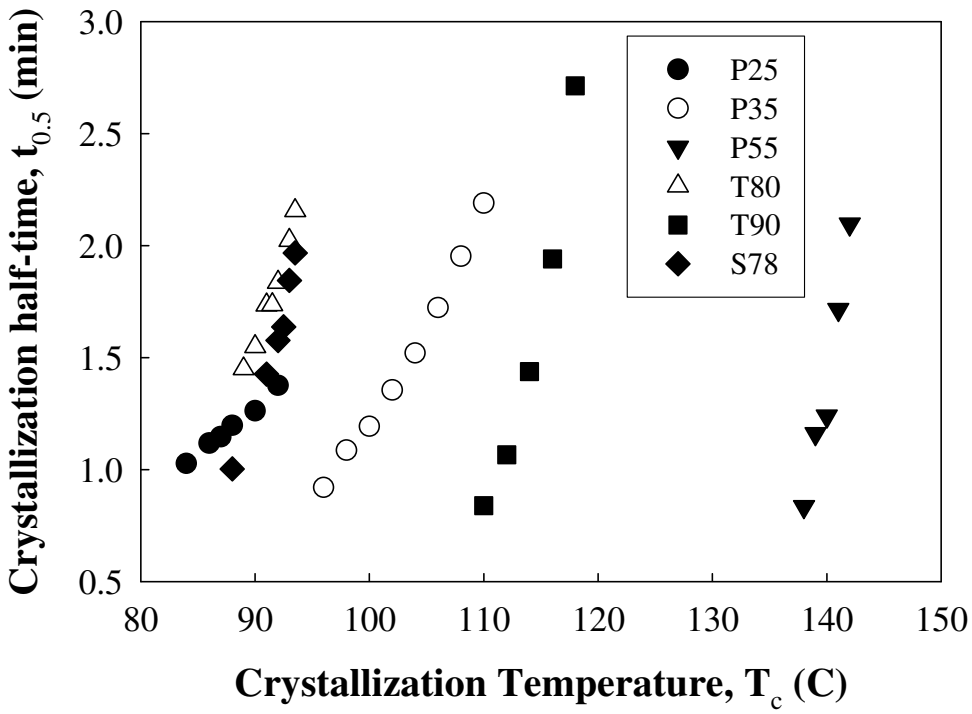

Figure 14: Crystallization half times of melt-blown webs as a function of T_c; Sample P25●, P35○, P55▼; T80Δ, T90■; S78♦

Typically, the crystallization half-time is used to represent the overall crystallization rate, which is assumed to be proportional to the inverse of crystallization half-time. Since the crystallization half-time depends on both n and k, comparison of the crystallization rates of different polymers having different n values is not appropriate. **[32]** However, as seen in Figure 10, the n values determined in this study for all different polymer types and hardness

grades do not change significantly and are all around 3. Therefore, the crystallization half-time can be used to compare the overall crystallization rates.

Figure 14 shows that in agreement with the results in Figure 13, the crystallization half-time increases with increasing temperature. The half-time also increases with increasing amount of non-crystallizable soft segment. This means the crystallization process of the crystallizable hard segment slows down since the non-crystallizable soft segment dilutes the probability for nucleation and crystal growth. **[35, 53, 70, 76]**

Figure 15 illustrates the dependence of the crystallization half-time on the degree of cooling, which allows comparison of different polymers under similar cooling conditions.

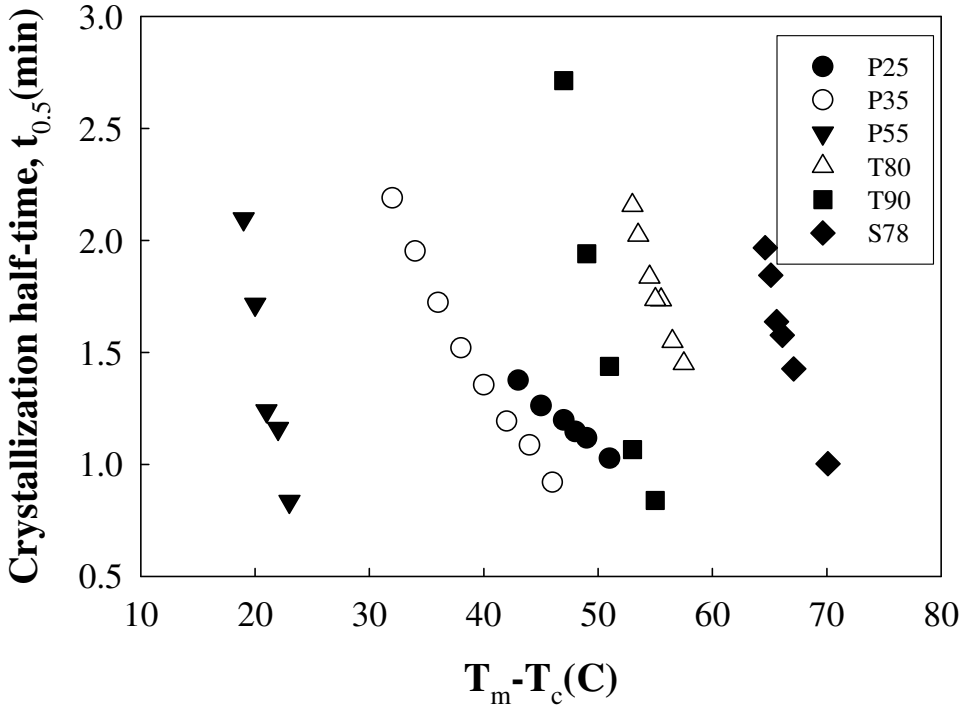

Figure 15: Crystallization half times of melt-blown webs as a function of degree of cooling; Sample P25●, P35○, P55▼; T80Δ, T90■; S78♦

In agreement with Figure 10, the degree of cooling required to reach the same crystallization half-time decreases with increasing crystallizable component in the order of P55 > P35 > P25 for PEBA, T98 > T90 > T80 for ether TPU, and S95 > S78 for ester TPU series. This means that for a given elastomeric copolymer, the increase in the overall crystallization rate is dependent on the relative concentration of the hard and soft segments under similar cooling conditions. This is also evident from the slopes of each curve, where the slope reflects the temperature and composition dependence of the overall crystallization rate.

IV. 4. Web Tensile Properties

The stress-strain behavior of melt-blown webs of PEBA, ether and ester TPUs under uniaxial extension at room temperature is shown in Figures 16 and 18 as a function of DCD. Regardless of the polymer type, hardness grade and DCD, the shapes of the curves are similar with the exception of strength and elongation at break values. At low extensions, the stress rises linearly with increasing elongations. This region is dominated by elastic rather than plastic deformation i.e. the web will relax to its original form with almost no tensile set upon stress removal. Beyond this region except for P55, the slopes of the curves gradually decrease until about 60-70%, above which the stress increases linearly with the applied strains at almost a constant slope until failure.

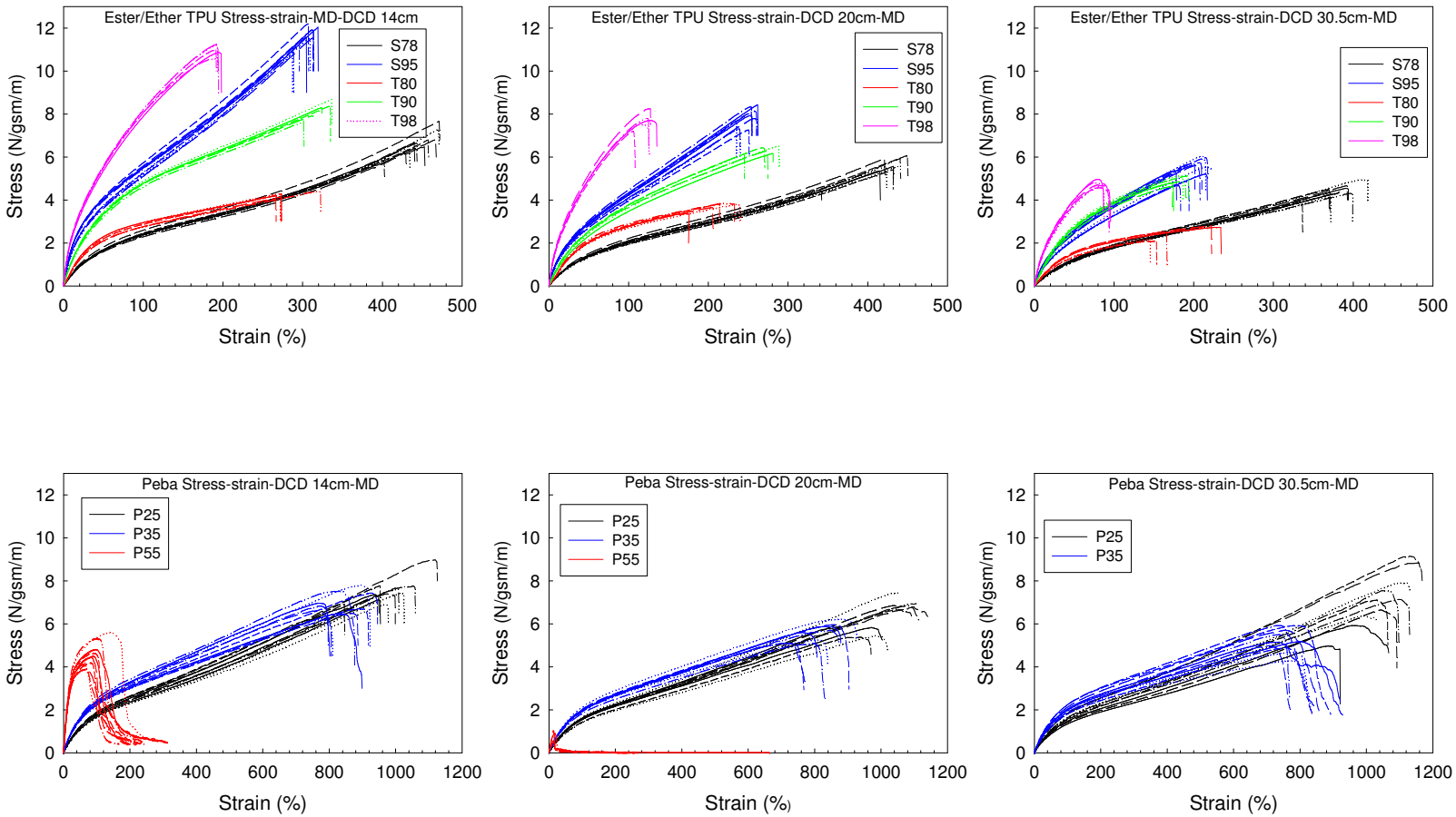

Figure 16: Stress-strain behavior of PEBA, Ether and Ester TPU webs in MD

No distinct yield point is observed and there's no necking, rather uniform reduction of the cross-sectional area of the dogbone sample during uniaxial extension is observed. The maximum stress is observed at break. [19, 64] The expected contribution of the polymer hardness on the tensile behavior is also confirmed in Figure 16, where with increasing crystallizable hard content the stress at a given strain, work to rupture and toughness increase, while the elongation at break decreases in the order of S95<S78 for ester TPU, T98< T90<T80 for ether TPU, and P55<P35<P25 for PEBA series. The dependence of the tensile behavior on polymer hardness grade is further illustrated in Figure 17, where 5% modulus is plotted as a function of DCD. As seen in Figures 16 and 17, at a given DCD, the 5% modulus increases with increasing polymer hardness grade for ether and ester TPU as well as PEBA series. This observed tensile behavior is typical reflection of the inherent elastomeric properties of these block copolymers. Tensile modulus of elastomeric polymers depends mainly on the crosslink density and the volume fraction of rigid fillers. Since both are represented by hard segments in TPU and PEBA elastomers, increasing polymer hardness grade should promote web tensile modulus and strength. **[63, 66, 77, 78]** However, at a given DCD, while web strength increases with increasing polymer hardness for both ether and ester TPU series, web strength of P55 decreases. P55 exhibits significantly lower strength than the softer grades even though it has the highest hard segment content within PEBA series. For well bonded elastomeric webs, the 5% strain should be much lower than those elongations corresponding to stress levels that exceed the cohesive strength of fiber-to-fiber bonding in melt-blowing web. Thus, we should expect to see the contribution of only the polymer properties on the observed tensile behavior.

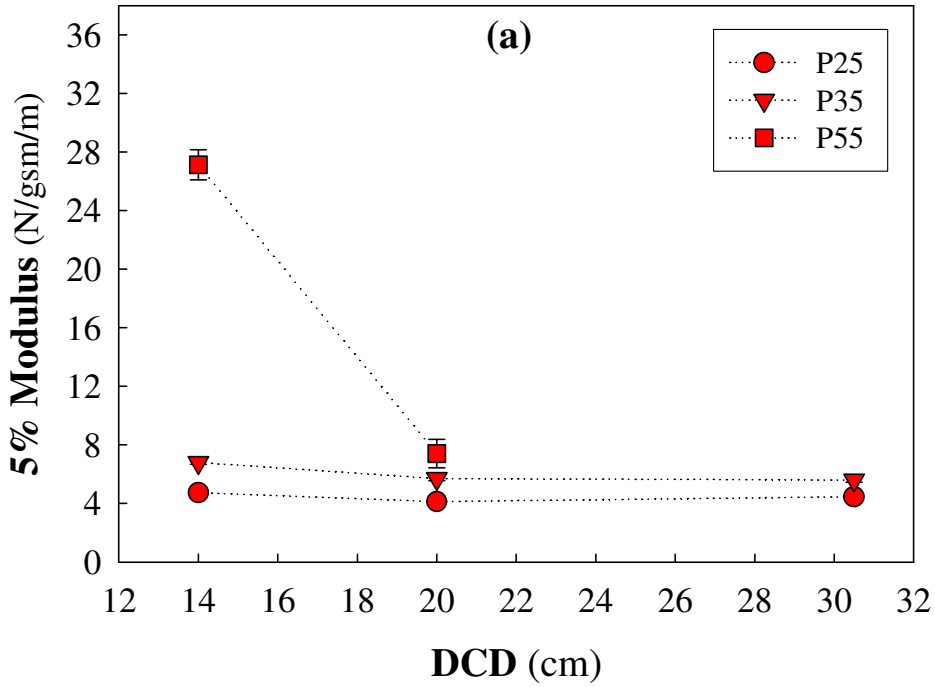

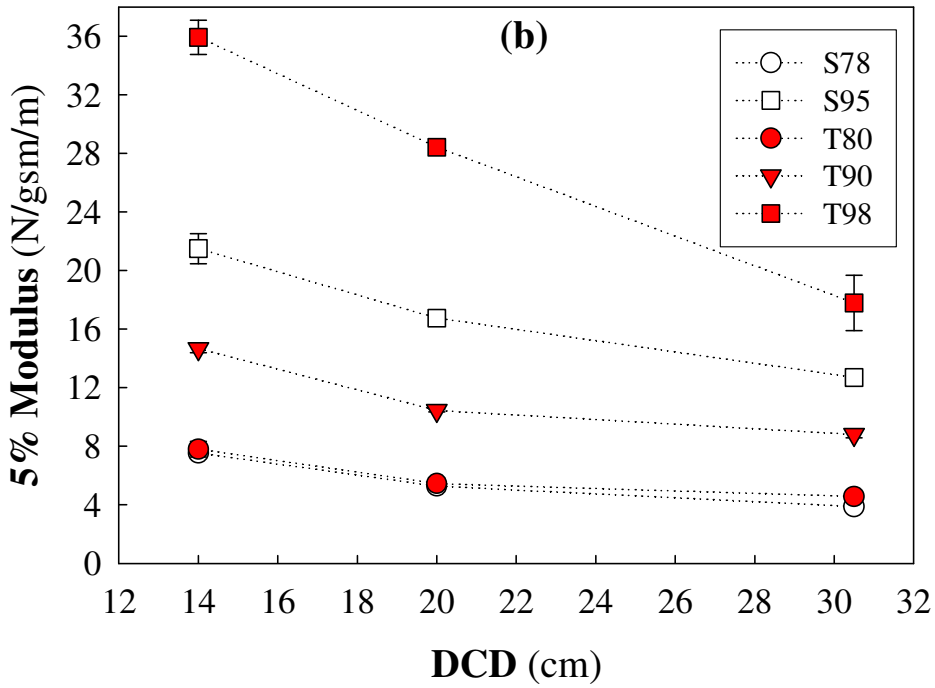

Figure 17: Tensile modulus @ 5% elongation **(a)** PEBA and **(b)** Ester and Ether TPU melt-blown webs in MD

But, as seen in Figure 17, 5% modulus of P55 also decreases with increasing DCD. To further understand this unexpected behavior, individual stress-strain curves are examined in Figure 18. In Figure 18, it is clearly observed that the web failure mechanism depends on the polymer type. I.e. upon application of the stress, the web stress increases to a maximum for both ether and ester TPU series. On reaching this point, the web sample fails abruptly. P25 and P35 also behave similarly, while P55 behaves quite differently. For P55, the web failure is gradual and separation of fiber layers within the web can clearly be observed during tensile testing. The gradual web failure is more pronounced with increasing DCDs, where the web strength for P55 drops to essentially zero. Observations of the melt-blown samples visually and under microscopy, P55 melt-blown webs consist of well-defined individual fibers rather than fused together as in the case of softer PEBA grades and TPU series. Upon application of stress, because the degree of fiber-to-fiber bonding in P55 is so low that fibers within the web debond very easily and tensile failure occurs through fiber-to-fiber bonding failure, not individual fiber failure. And, the failure stress is reached at lower elongations.

Since all factors except polymer hardness remain unchanged, this unexpected tensile behavior indicates that the polymer type and hardness grade are not the only factors responsible for the web strength, but there are other mechanisms that need to be considered. These are particularly important in melt-blowing since this process typically produces self-bonding webs that derive their strength from fiber to fiber contacts. Therefore, the ability of the newly formed fiber to stick to the other fibers already on the collector is critical to ensure efficient stress transfer within the web upon deformation.

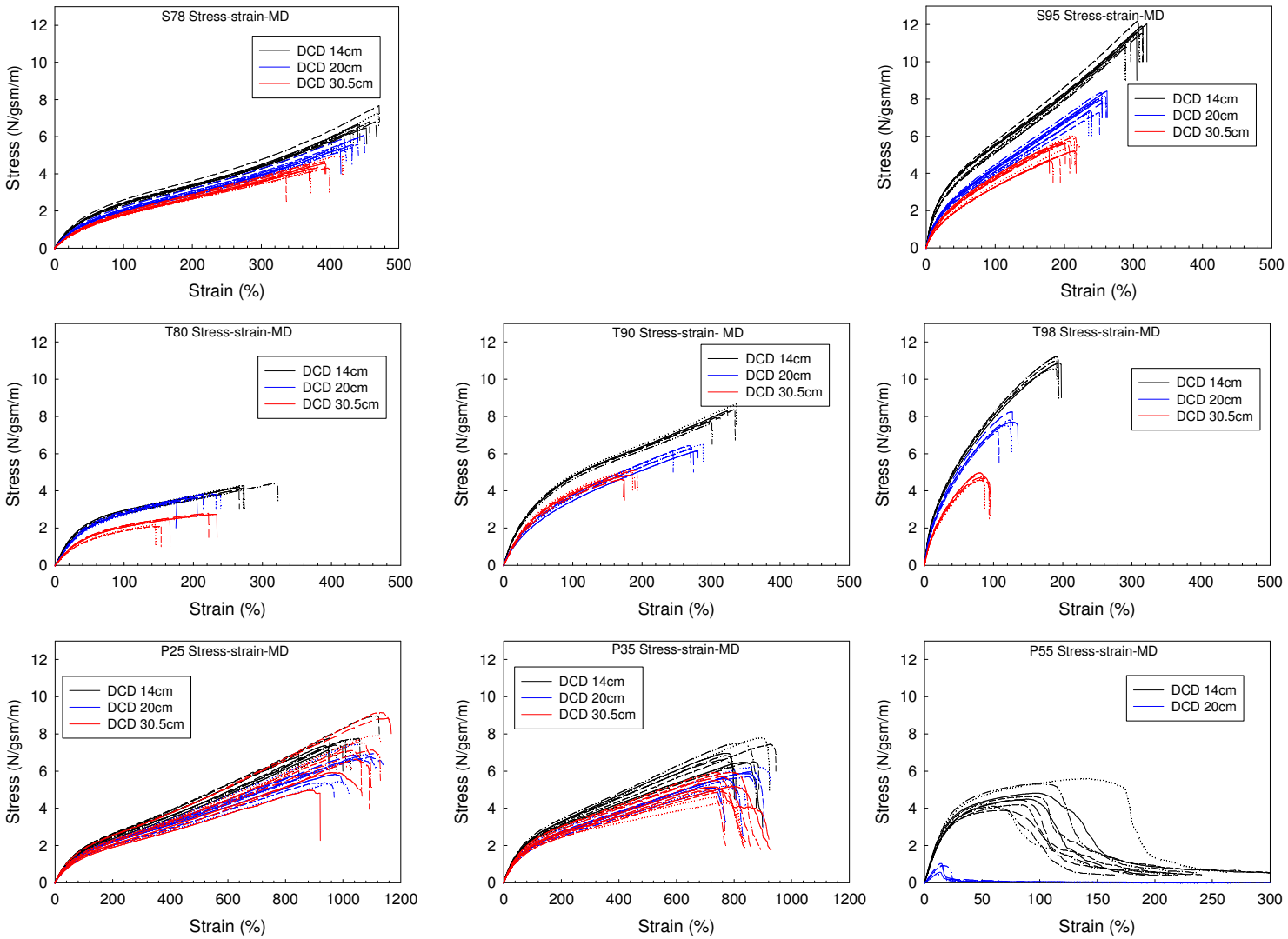

Figure 18: Stress-strain behavior of PEBA, Ether and Ester TPU webs in MD

The degree of attenuation and solidification attained when the fiber contacts with the others already on the collector will depend on the distances traveled between the die and the collector (DCD), the polymer extrusion and air temperatures, and the crystallization behavior of the polymer with changing polymer hardness. The effect of the DCD on the tensile strength and elongation at break of melt-blown webs of PEBA, ether and ester TPU is shown in Figures 19 and 20. As seen in Figure 19, for all studied polymers and DCDs, machine direction tensile values were noticeably higher than those in cross direction. This can be attributed to slightly higher fiber orientation in machine direction in these melt-blown web samples as shown in Figure 29.

For TPU series and for a single polymer grade, webs made at shorter DCDs have higher tensile strength and higher elongation to break than those made at greater distances. This clearly demonstrates the dependence of web properties on DCD. For PEBA series, the tensile strength and elongation to break of the P55 web decrease rapidly with increasing DCD. For a given polymer system regardless of the polymer type and hardness grade, the decrease in tensile strength and the decrease in elongation to rupture with an increase in DCD suggest that adhesion between fibers within the web decreases as DCD increases. However, the tensile strength and elongation to rupture remain relatively constant for P25 and P35 as a function of DCD. For these polymers, inter-fiber bonding appears to be independent of DCD over the range of DCDs tested.

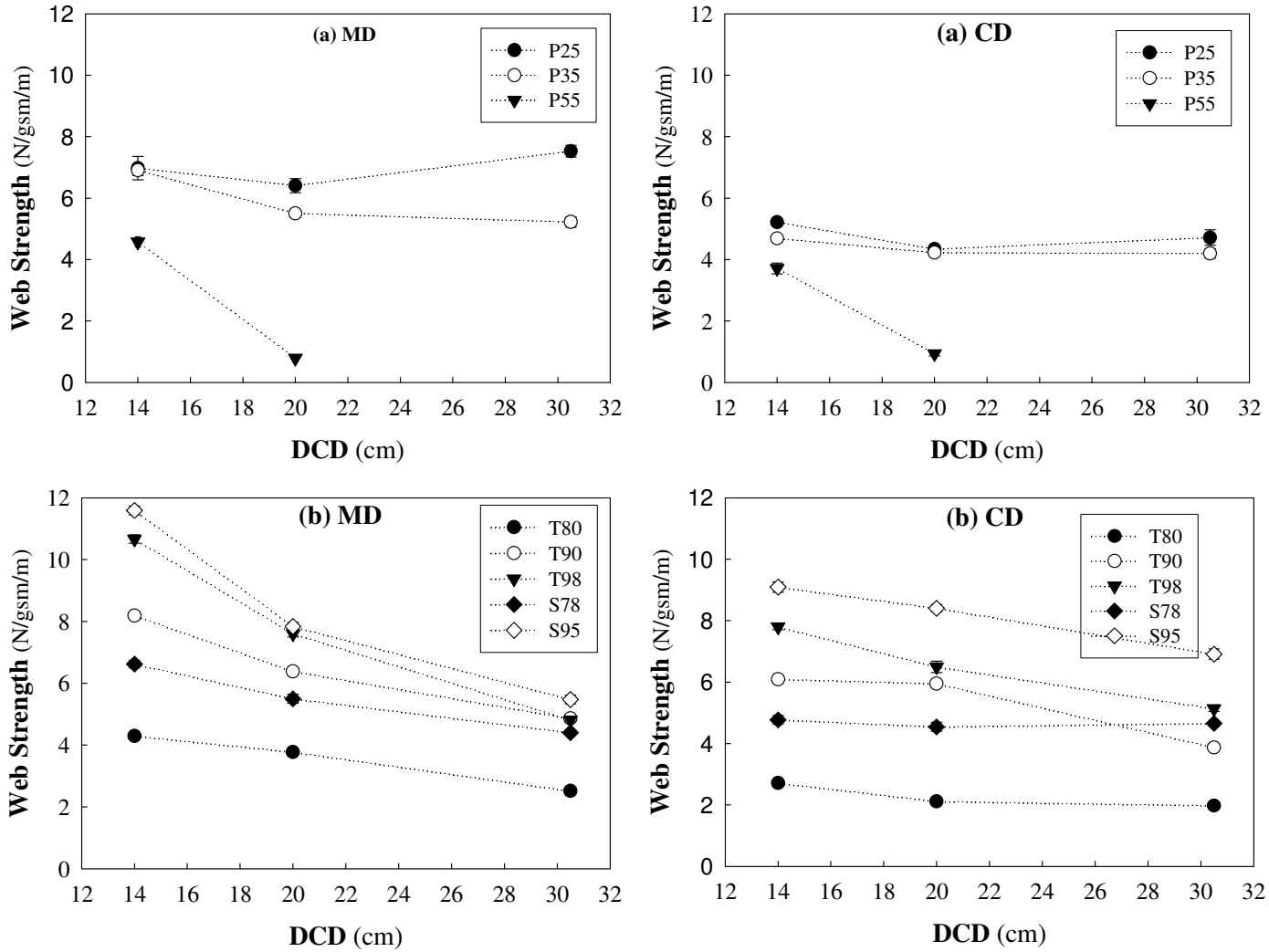

Figure 19: Tensile behavior of **(a)** PEBA and **(b)** Ester and Ether TPU melt-blown webs in MD & CD. Sample P25●, P35○, P55▼; T80●, T90○, T98▼; S78♦, S95◊

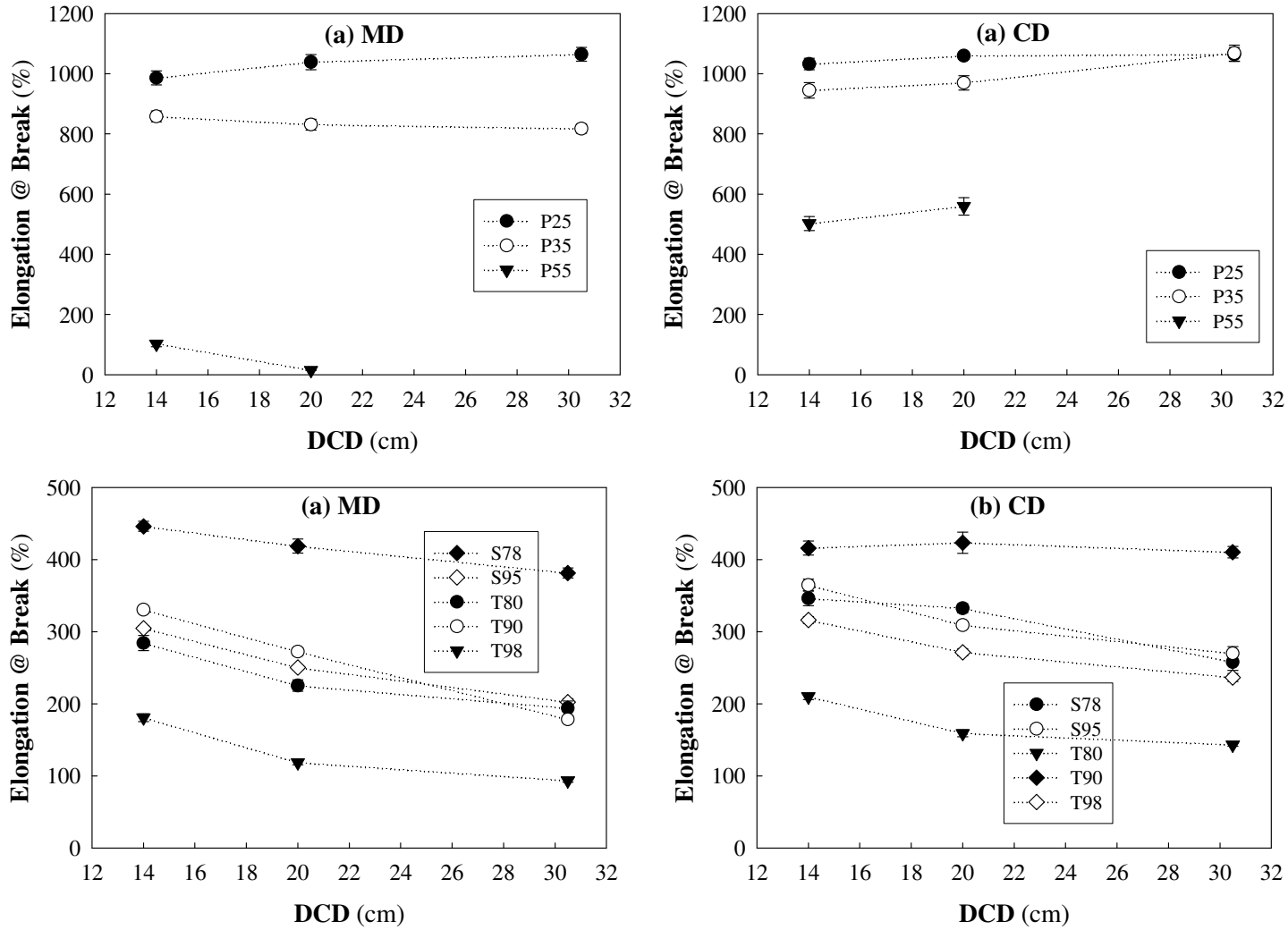

Figure 20: Elongation to break behavior of **(a)** PEBA and **(b)** Ester and Ether TPU melt-blown webs in MD & CD**.** Sample P25●, P35○, P55▼; T80●, T90○, T98▼; S78♦, S95◊

We propose that this behavior can be explained as follows. The melt-blown webs produced from the polymers studied were self-bonding structures, i.e. no mechanical and/or thermal bonding was employed after the fibers were deposited on the collector. This means the web structures derive their strength from fiber-to-fiber contacts and the ability of the fibers to stick to other fibers already on the collector is critical. Thus, the response of the melt-blown webs to applied mechanical forces depends on the constituent fiber properties, web structure and degree of fiber-to-fiber bonding.

IV. 4. 1. Polymer Orientation

In melt-blowing process, the fiber formation process and fiber strength depends on the stress applied on the polymer melt exiting the die until reaching the collector, and also the quenching conditions. Because at distances very close to the die the polymer melt is attenuated very rapidly by the high velocity air having temperatures close to polymer melt temperatures, the polymer chains have very little or no orientation. Lack of molecular orientation within the fibers was confirmed by the very low web shrinkage results of around 0- 1% as per AATCC 135/150-95 (120F wash, dry 160F). This is in agreement with Rovere and Shambaugh **[91]**, where they analyzed the fiber morphology in melt-blowing process by AFM. They observed spherulites covering the fiber surface, indicative of polymer crystallization under quiescent conditions but not under strain. Since there is no orientation of the polymer chains within the fibers, the strength of the fibers within the web should depend only on the amount of crystallization attained when deposited onto the collector. I.e. because fiber morphology is similar within all webs and DCDs, the fiber strength is dependent on the

polymer type and its crystallization behavior but not fiber morphology. This means that the differences in the web strength as a function of DCD does not depend on the constituent fiber properties, but rather on the web properties such as fiber orientation and bonding.

IV. 4. 2. Polymer Crystallization

To further illustrate that the fiber morphology is similar within melt-blown webs processed at different DCDs and extrusion temperatures, DSC heating scans were run as shown in Tables 6-8 and Figures 21-28 for PEBA, ester TPU and ether TPU series. As clearly observed, the DSC data and heating profiles of the melt-blown webs processed at different DCDs from PEBA, ester and ether TPU elastomeric polymers are almost identical for a given polymer hardness grade. Comparison of transition temperatures and corresponding melting enthalpies of melt-blown webs for different DCDs confirms that the fiber strength does not depend on the DCD but on the polymer type and hardness grade for these elastomeric copolymers.

Table 6: DSC heating scans and data for PEBA series

Sample	**DCD** (cm)	$\mathbf{T_{m1}}$ (°C) (T_{mPE})	$\mathbf{\Delta H_1}$ (J/g) (ΔH_{PE})	$\mathbf{T_{mPA}}$ (°C) $\mathbf{T_{m2}}$	$\mathbf{T_{m3}}$	$\mathbf{\Delta H_3}$ (J/g) (ΔH_{PA})
P25	14	6.2	32.4	60.0	135.2	24.9
	20	6.6	32.4	58.7	134.5	21.1
	30.5	6.7	32.0	55.1	134.9	22.4
P35	14	4.6	26.9	59.3	141.8	18.9
	20	4.4	27.4	58.8	140.9	21.8
	30.5	4.3	27.1	59.8	140.4	29.2
P55	20	***	***	****	160.1	36.9
	14	***	***	59.2	161.7	46.4

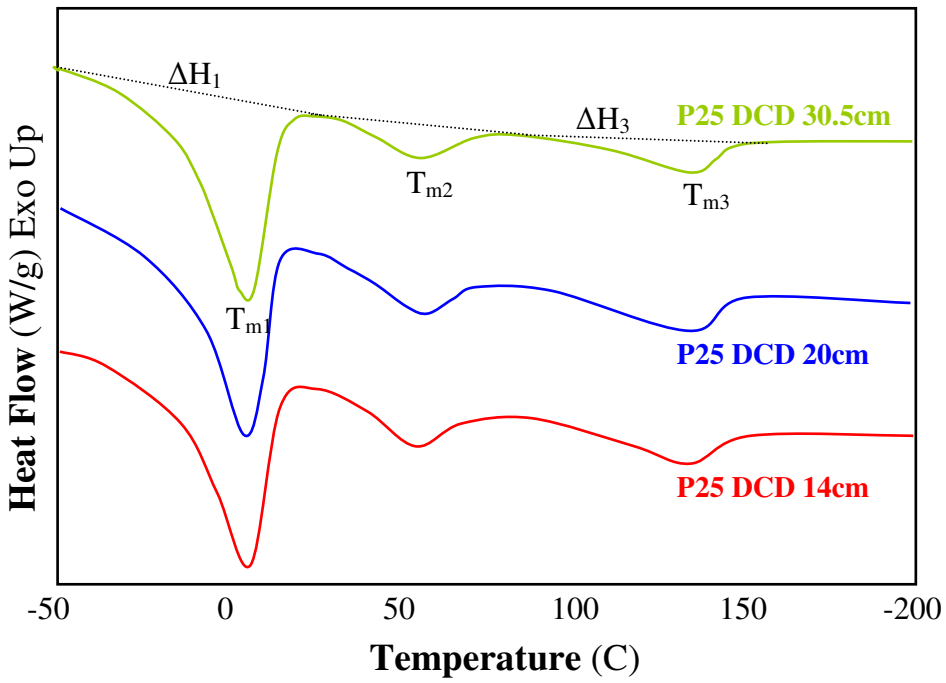

Figure 21: 1st heating DSC scans of P25 melt-blown webs

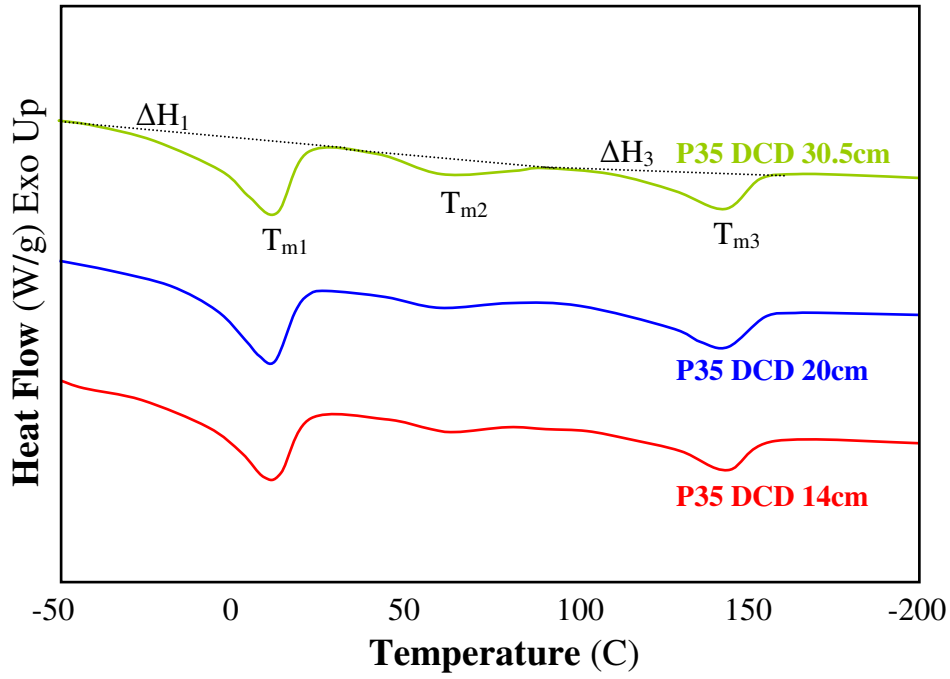

Figure 22: 1st heating DSC scans of P35 melt-blown webs

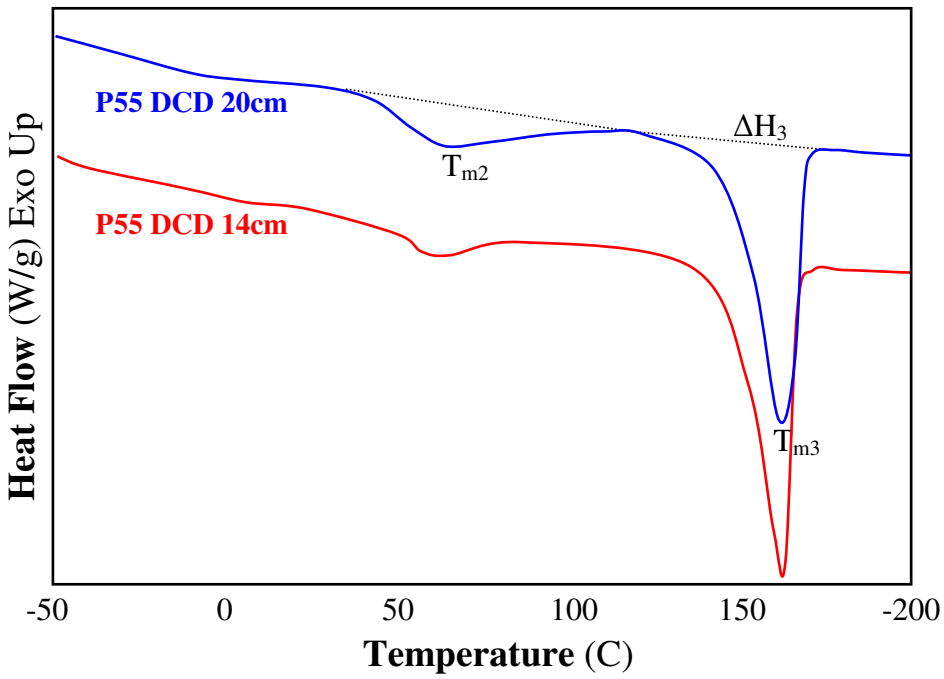

Figure 23: 1st heating DSC scans of P55 melt-blown webs

Table 7: DSC heating scans and data for ester TPU series (average values shown)

Sample	**DCD** (cm)	**Tg** (°C)	**T_{mhard}** (°C)		**ΔH_{hard}** (J/g)
			T_{onset}	**T_m**	
S78	14	-48.0	53.1	158.1	19.0
	20	-48.7	55.2	155.8	18.5
	30.5	-48.6	51.4	156.3	15.9
S95	14	-35.9	126.2	196.1	32.1
	20	-34.1	129.5	195.7	27.2
	30.5	-43.3	132.9	195.9	28.6

Table 8: DSC heating scans and data for ether TPU series (average values shown)

Sample	DCD (cm)	T_{mhard} (°C)			ΔH_{hard} (J/g)
		T_{onset}	T_{m1}	T_{m2}	$\Delta H_1 + \Delta H_2$
T80	14	28.3	73.7	146.5	32.1
	20	24.7	74.0	146.3	30.2
	30.5	27.3	73.7	145.6	32.8
T90	14	29.7	73	165.3	29.7
	20			166.2	29.5
	30.5	26.6	73.5	165	28.9
T98	14	23.4	72.1	183.3	44.7
	20	46	74.4	183.5	37.3
	30.5	21.3	71.3	184.5	45.4

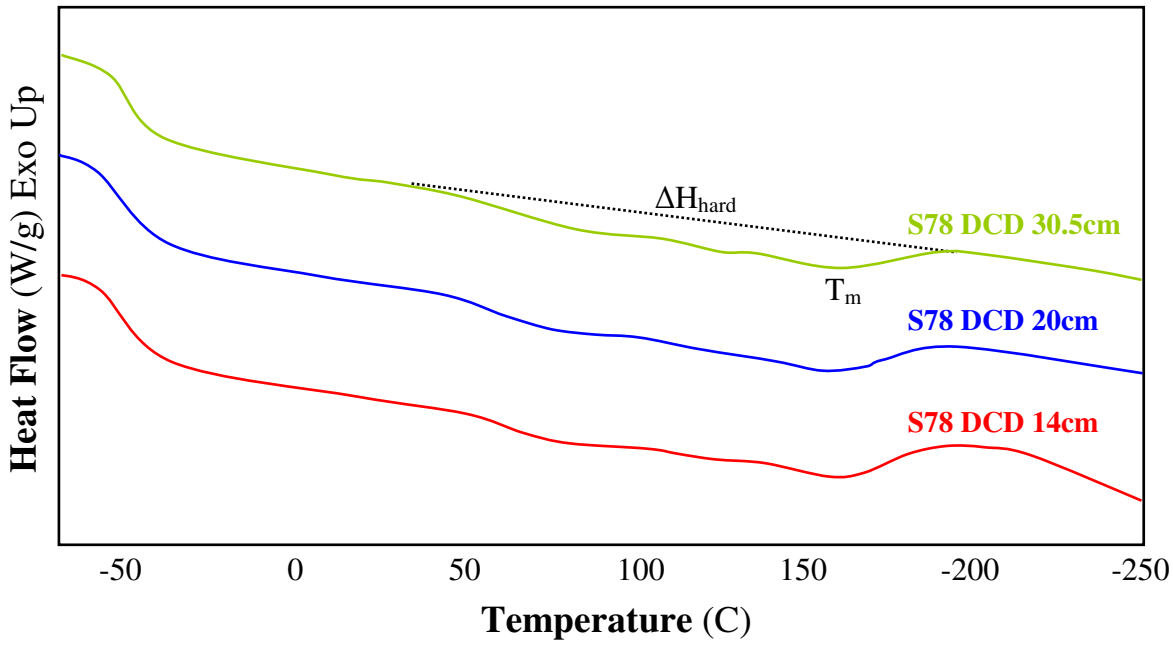

Figure 24: 1st heating DSC scans of S78 melt-blown webs

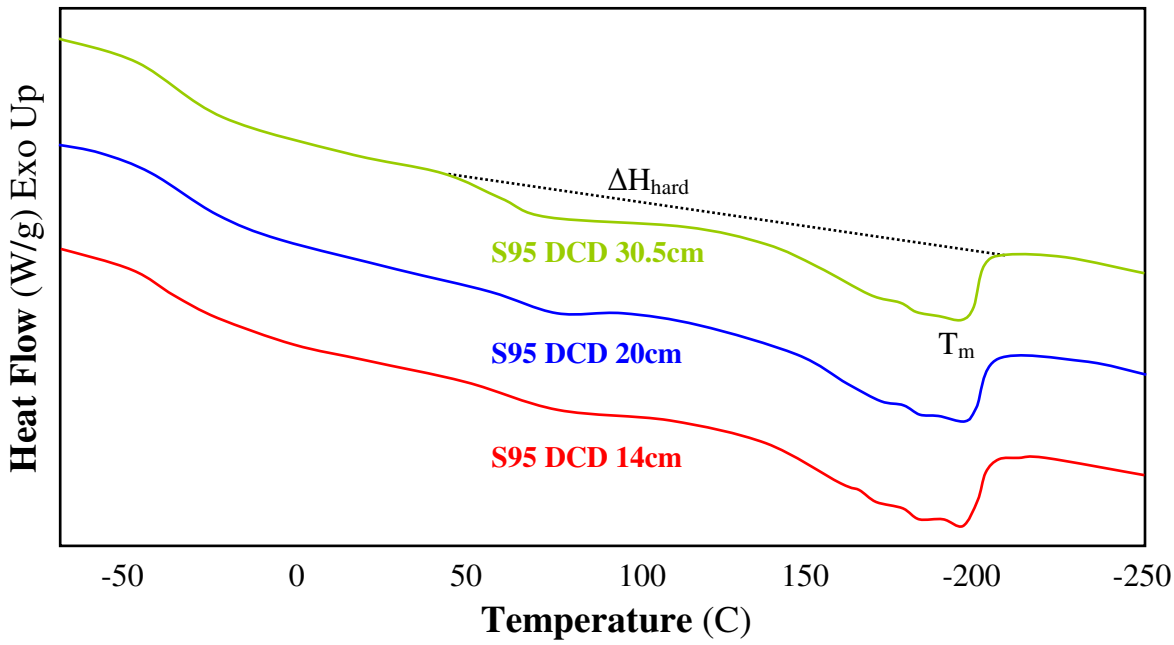

Figure 25: 1st heating DSC scans of S95 melt-blown webs

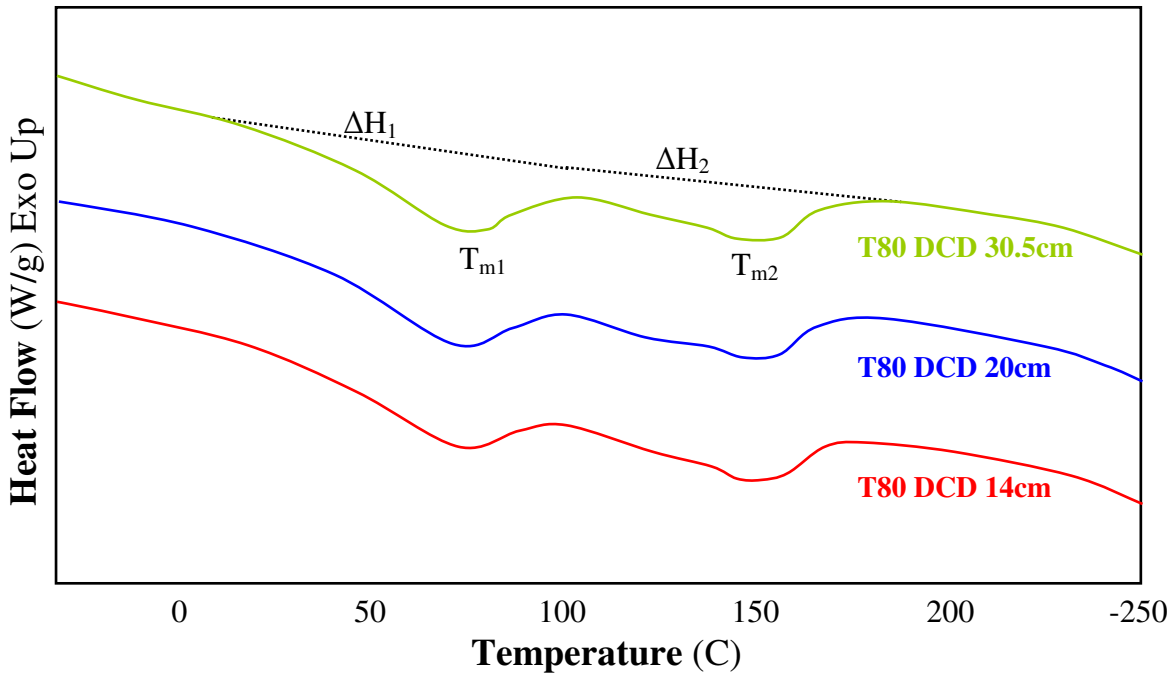

Figure 26: 1st heating DSC scans of T80 melt-blown webs

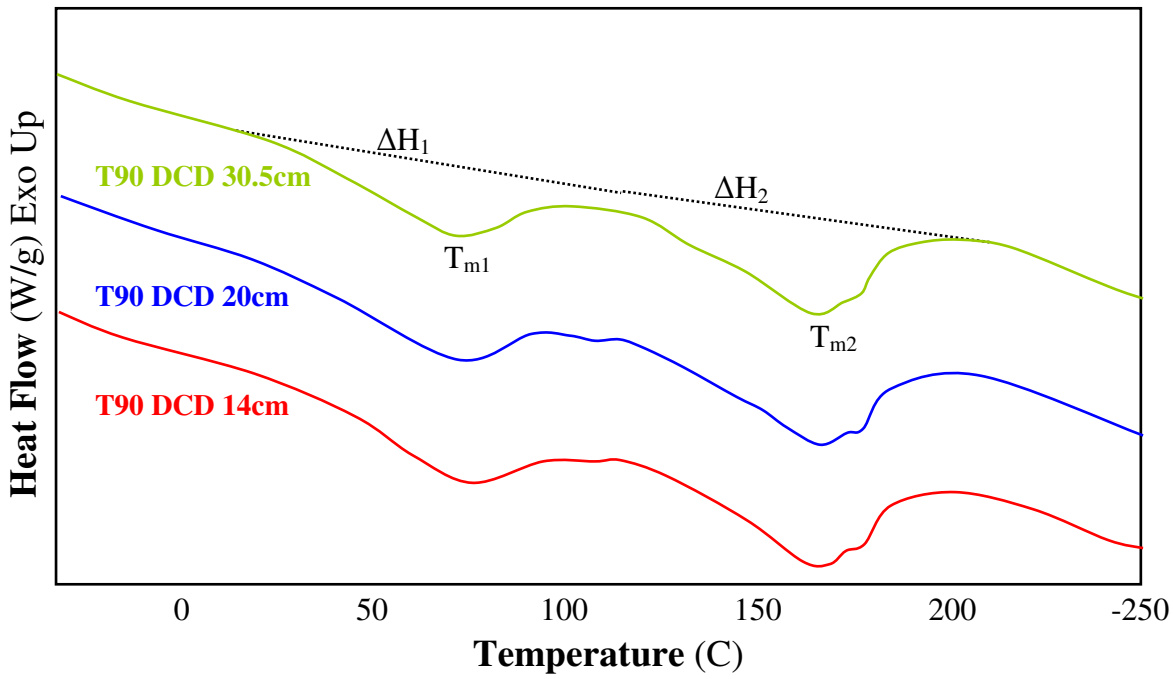

Figure 27: 1st heating DSC scans of T90 melt-blown webs

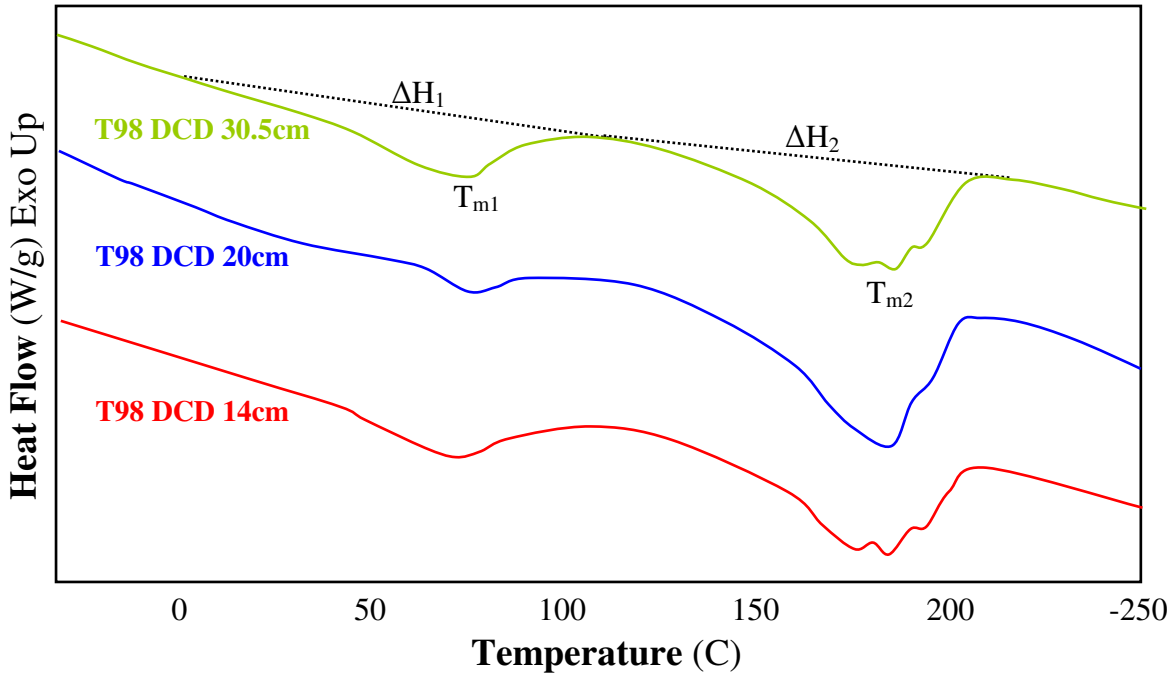

Figure 28: 1st heating DSC scans of T98 melt-blown webs

IV. 4. 3. Fiber Orientation

Since the fiber morphology is the same for a single polymer formed into a web at different DCDs, the difference in the web strength depends rather on the web properties mainly on fiber orientation and the degree of fiber-to-fiber bonding. The fiber orientation distribution function i.e. ODF of the produced melt-blown webs is shown in Figure 29. The fibers of PEBA and ether TPU webs are slightly oriented in the machine direction as typically expected from melt-blowing process and webs produced. As clearly illustrated, the fiber orientation within the web structure is not influenced by the DCD or polymer type. Thus the web strength for a single polymer should depend primarily on fiber-to-fiber bonding.

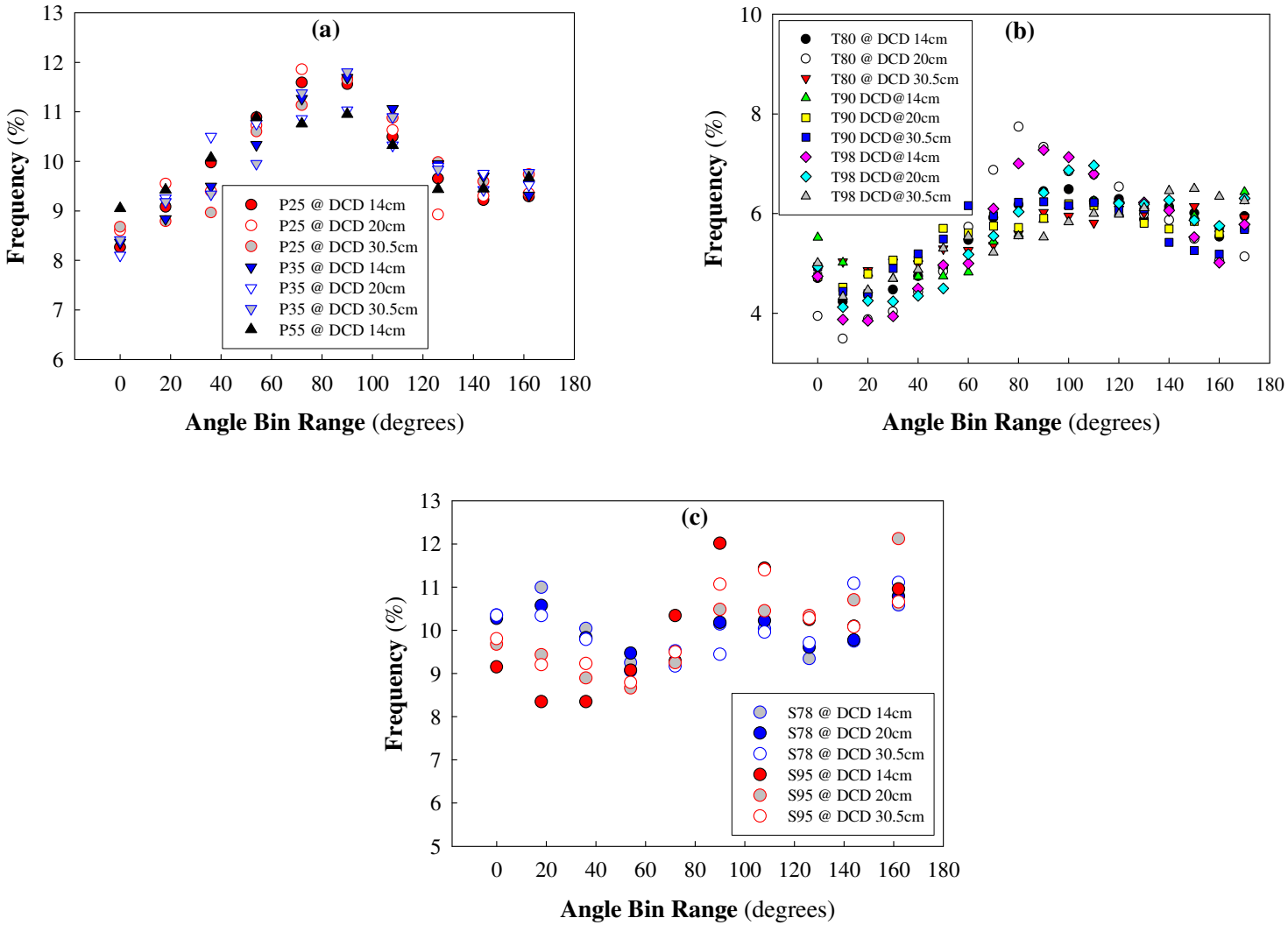

Figure 29: Orientation distribution functions of **(a)** PEBA and **(b)** Ether TPU and (c) Ester TPU melt-blown webs

IV. 4. 4. Inter Fiber Bonding

The dependence of the web strength on fiber-to-fiber bonding and polymer crystallization behavior can further be confirmed by the tensile behavior of the films produced from the same polymers and hardness grades. Since the film structure does not rely on fiber-to-fiber bonding, the observed tensile behavior should reflect the inherent properties of the studied elastomeric copolymers. As seen in Figure 30, for both TPU and PEBA series, the modulus i.e. the stress at a given strain and at break becomes larger with increasing polymer hardness, while the elongation at break decreases. The elongation at break values for S78 and P25 will be larger than observed in Figure 30 since these film samples had not broken even upon reaching the upper limit of the testing length of the equipment. In addition, slippage at the grips was observed for S95 and P55. Regardless, the tensile behavior of the film samples reflects the expected contribution of the elastomeric polymers, thereby confirming the importance of the inter-fiber bonding in the web strength.

To further confirm the dependence of the web strength on the polymer type and crystallization behavior as well as DCD, melt-blown webs were produced from 1,500MFR PP. This polymer is one of the most commercially used polymers in melt-blowing industry and well-known to be a fast crystallizing polymer. The web strength and elongation at break of the PP melt-blown webs as a function of DCD is shown in Figure 31.

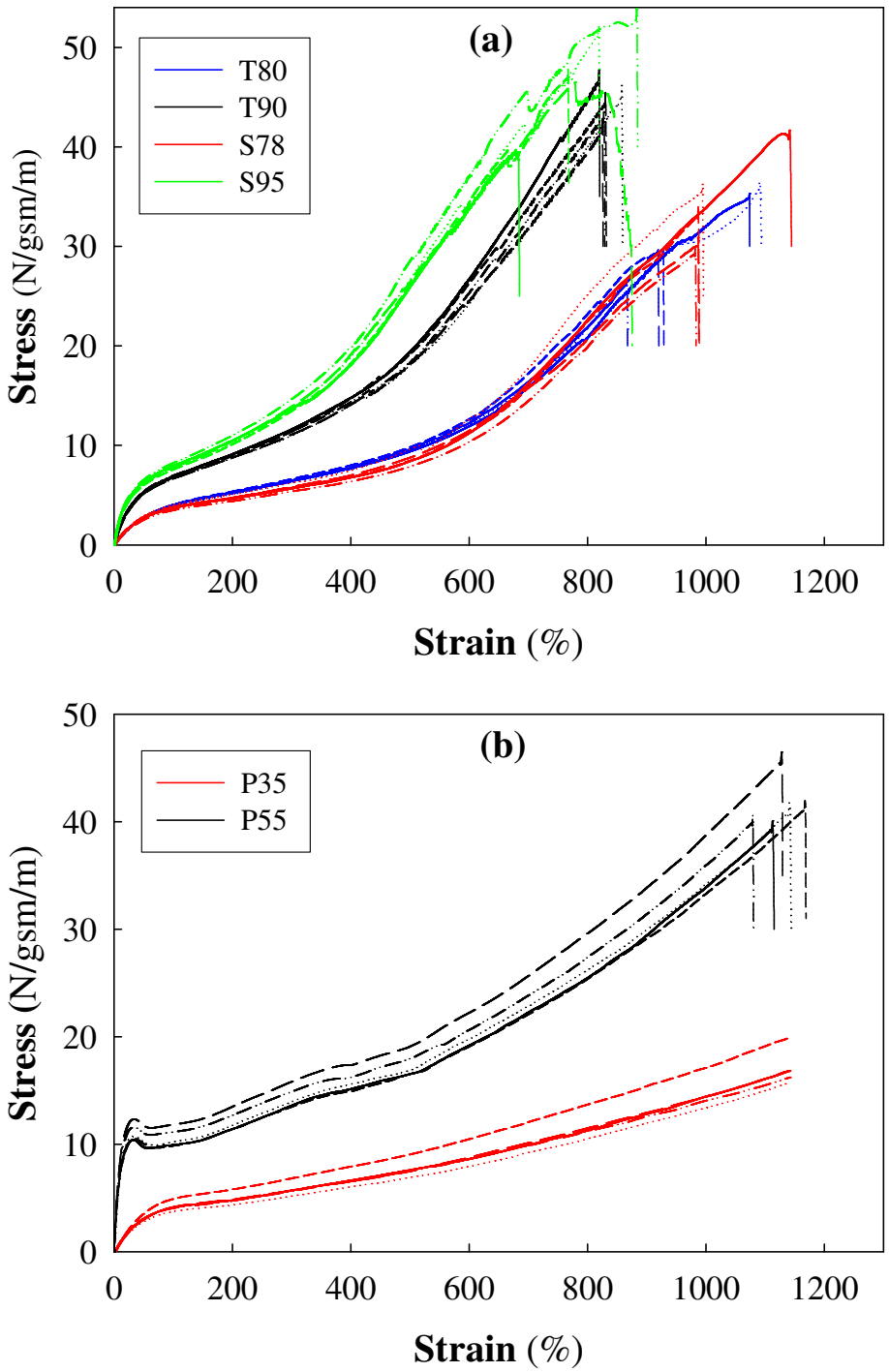

Figure 30: Tensile behavior of cast-film samples of **(a)** ether and ester TPU and **(b)** PEBA. For a single polymer type, individual stress-strain curves are shown for 5 replicates.

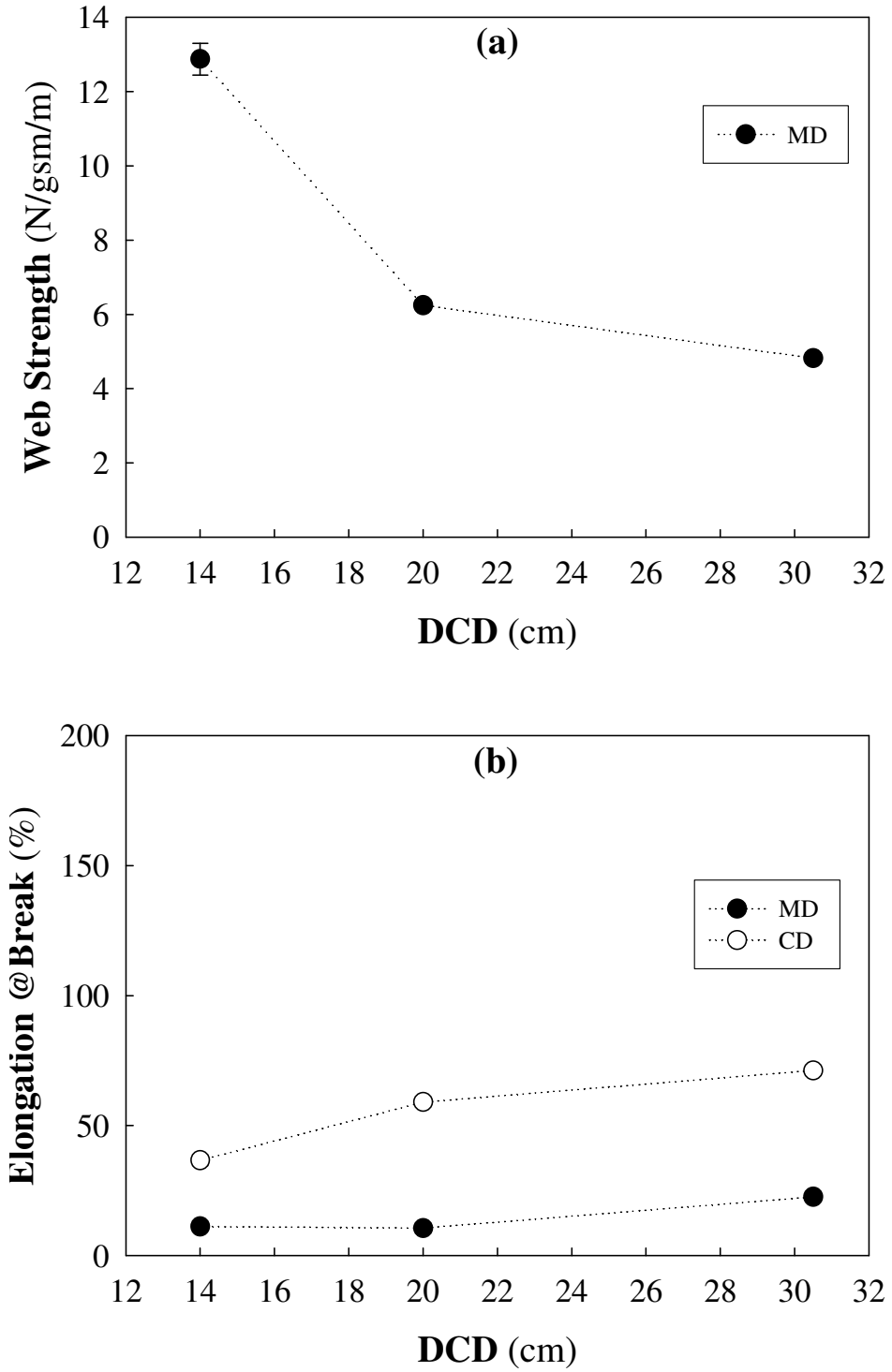

Figure 31: (a) Tensile and **(b)** elongation to break behavior of PP melt-blown webs in MD & CD**.**

Comparison of the TPU hard grades S95 and T98, Figures 19 to PP in Figure 31, the tensile behavior of PP melt-blown webs is strongly dependent on the DCD i.e. with increasing DCDs, the stress corresponding to the inter-fiber strength and therefore the web failure becomes lower since the fibers solidify more when reaching the collector. The web strength values for PP is higher than those of P55, and does not drop to 0 at DCD=20cm and DCD=30.5cm. This clearly indicates that P55 crystallizes much faster than PP even though the web failure mechanism of PP is very similar to that of P55. As seen in Figure 32, the PP melt-blown web fails by disassociation of individual fibers rather than breaking of the fibers. Also seen in Figure 31 is that the elongation at break values of PP melt-blown webs both in CD and MD increase with increasing DCDs, similar to P55 CD behavior in Figure 20.

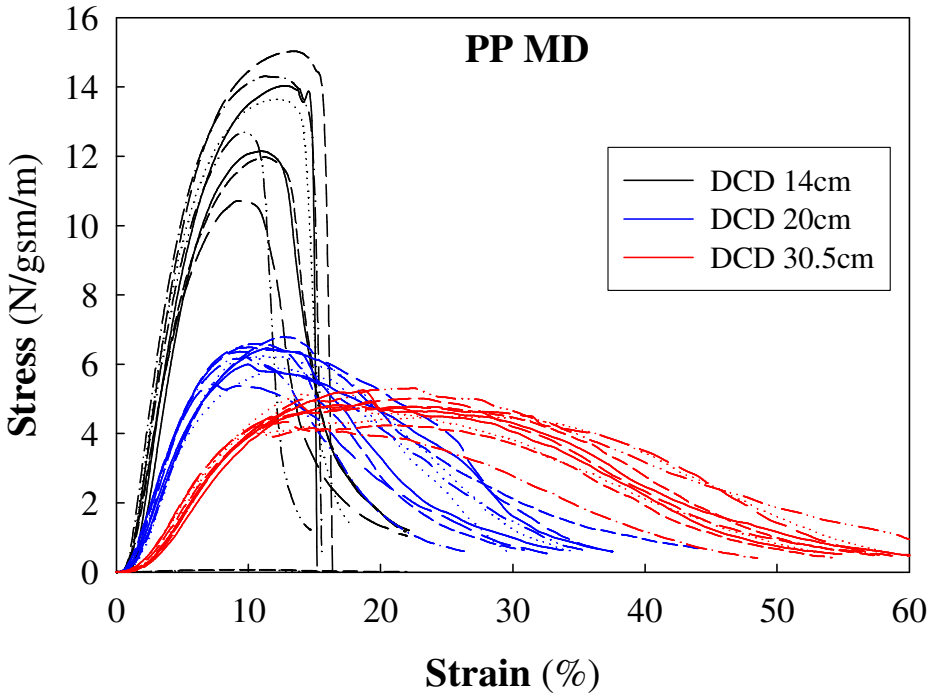

Figure 32: Stress-strain behavior of PP melt-blown webs in MD

Thus, the elongation values observed at the maximum stress were plotted for all the series studied, ether TPU, ester TPU, PEBA, and PP in Figure 33. As seen in Figure 33 (a) and (b), the elongation at maximum stress behavior is the same as that of elongation at break seen in Figure 20. While PP elongation at maximum stress increases slightly with increasing DCDs, the values are much lower than those in Figure 31(b). Even though the crystallization behavior of P55 and PP are similar from comparison of Figures 19-20 to Figures 31-33, PP has much lower elongation values than that of P55. This is expected since P55 is an elastomeric polymer while PP not.

Therefore, we propose that the observed web strength behavior with changing DCD can be attributed primarily to fiber-to-fiber bonding when the newly formed fiber contacts the others already on the collector. This in turn is determined by the distances traveled between the die and the collector (DCD) and the crystallization behavior of the polymeric material, i.e. polymer type. At shorter DCD, fibers are collected while they are still somewhat tacky from incomplete crystallization, promoting considerable self-bonding of fibers. Because fibers complete solidification after forming the web structure, fiber-to-fiber adhesion is strong, yielding a compact web with higher tensile strength. With increasing DCD, however, fibers travel longer distances and thus have more time to solidify before reaching the collector. Because the fibers will have lower temperatures, the level of interfiber adhesion decreases leading to a loftier and less coherent web.

To test this hypothesis, the air velocity and temperature were measured and the crystallization kinetics of the polymers studied were mapped onto the profiles obtained as described in the following sections.

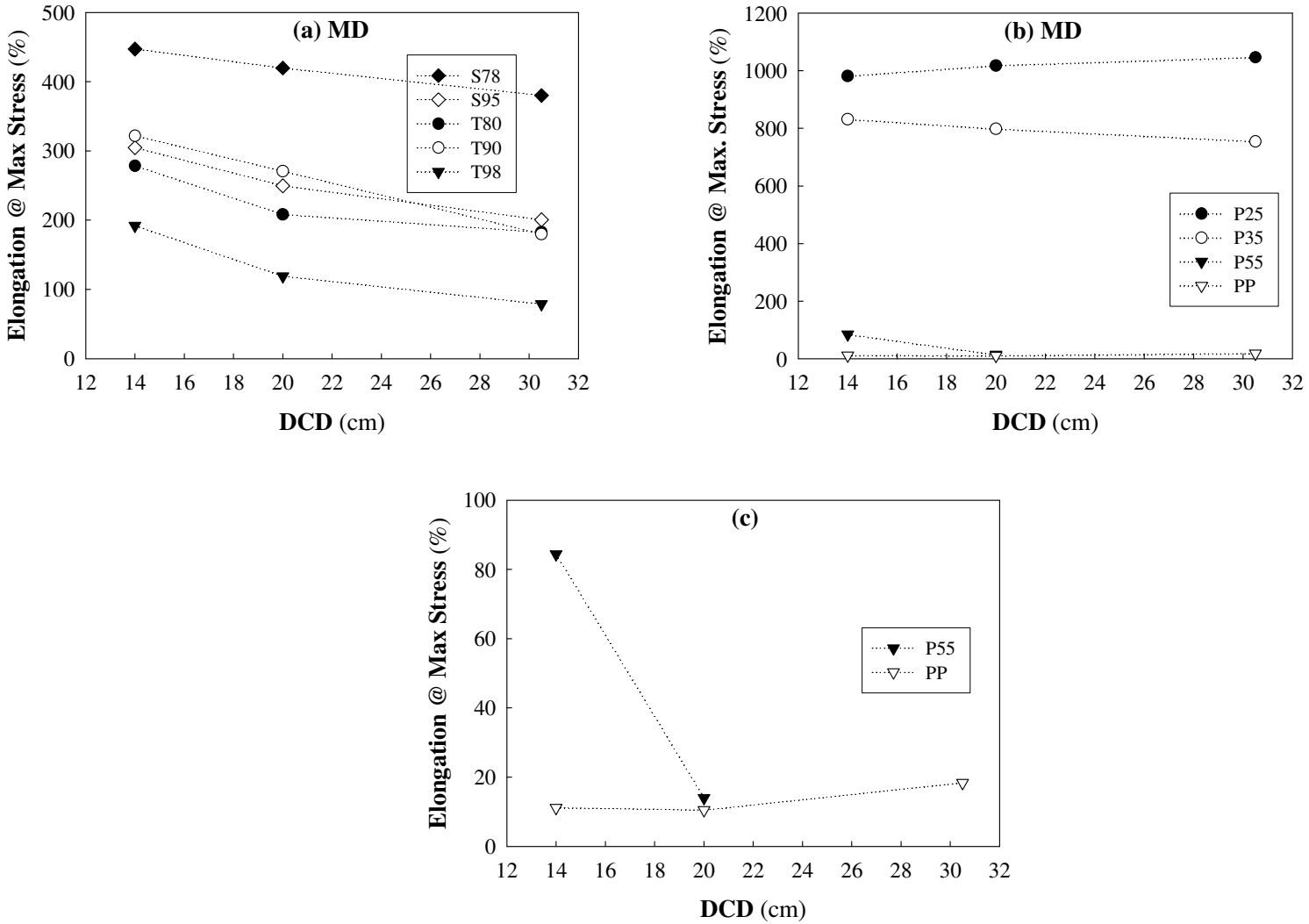

Figure 33: Elongation at maximum stress behavior (in MD) of **(a)** ester and ether TPU (**b**) PEBA, PP, and **(c)** P55 vs PP

IV. 5. Melt-Blowing Air Temperature and Velocity Profiles

Figure 34 shows the development of the air velocity profile at air temperatures of 260°C and 315°C. Figures 34a and b show that the axial air velocity at $x=0$ (centerline) decreases rapidly with increasing distance, z below the die until reaching a plateau for $z>5$ *cm*. For x = 1.59, 3.18 and 6.35 mm, the axial air velocity first increases to a maximum, then rapidly decays with further increasing z-distances until reaching a plateau. The spreading effects is further illustrated in Figure 34c, where for positions near the die a single maximum in the velocity profile is observed at the centerline just below the die face ($x=0, y=0$) and decreases rapidly with increasing distances in the x-direction. This means the air jets from the two individual slots have already merged at the centerline prior to or just exiting the die producing a single maximum velocity peak as expected due to the sharp, inset configuration of the melt-blowing die. **[44]** It is this first significant air velocity drop region, $0< z<5$ *cm,* where the polymer melt exiting the capillaries meets with the maximum, very high air velocity at the centerline. This results in a rapid attenuation of the polymer melt. In all cases, beyond this region, $z>5$ *cm*, the air velocity approaches a constant value and this velocity is nearly the same for all x-positions examined. This implies that drag force is important for z<5 cm, but negligible for z>5 cm.

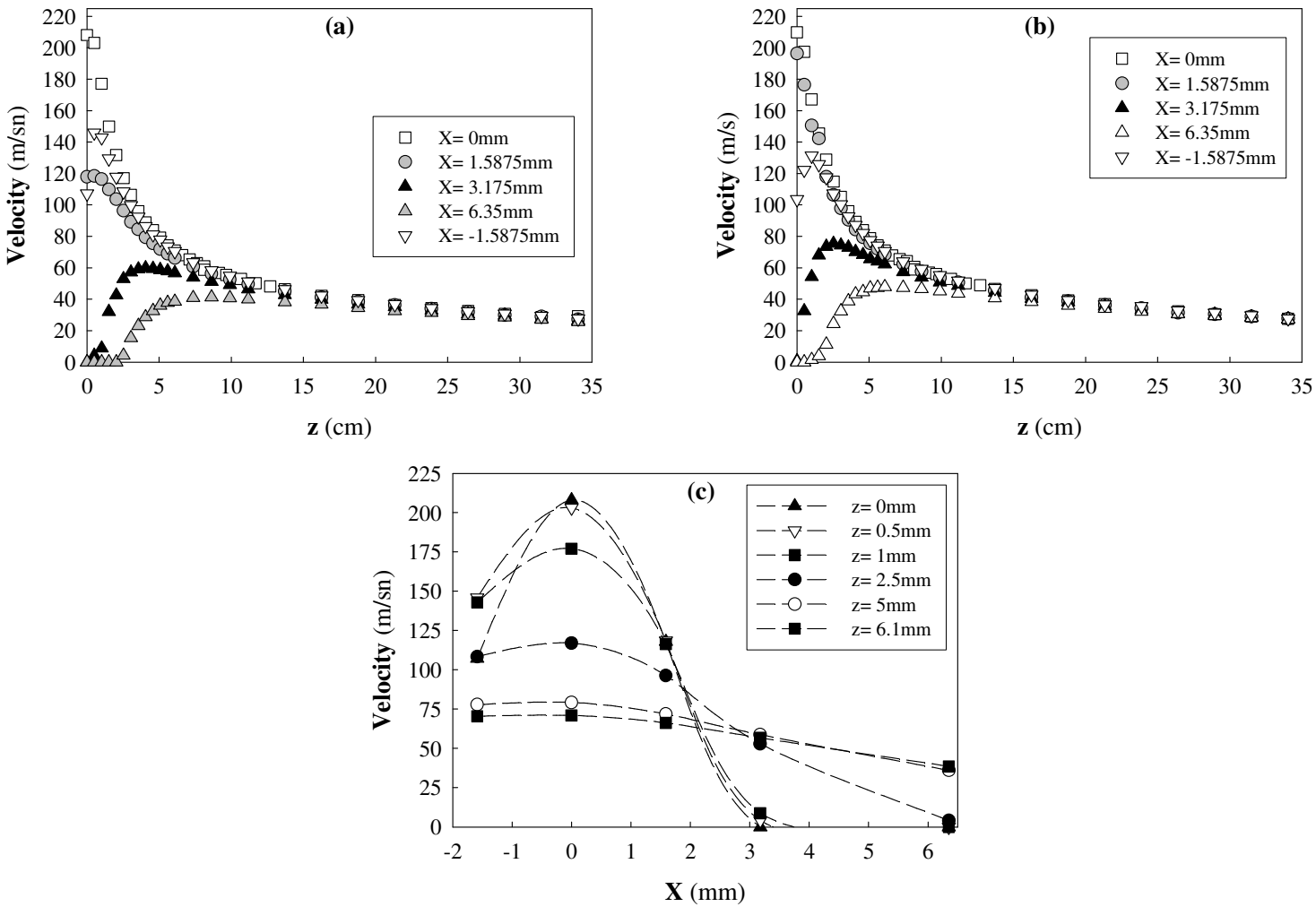

Figure 34: Air velocity profiles across melt-blowing die as a function of z (DCD) at air temperatures of **(a)** 260°C and **(b)** 315°C. And, **(c)** Air velocity profile at air temperature of 260°C in the x-direction (across the die face)

Figure 35 shows the air temperature profiles which accompany the velocity profiles in Figure 34. It can be seen that the air temperature at positions close to the center and at the centerline drops significantly even at the die tip. It is this temperature drop that is believed to be the driving force for crystallization of the polymer melt and fiber formation in melt-blowing process. Beyond z>5 cm crystallization continues to occur but under nearly isothermal conditions and at a slower rate. This is mainly because the fibers have fine diameters in this region and are exposed to uniform, almost flat air temperature and velocity profiles. Hence, fiber temperatures can be assumed to approximate the temperatures of the air surrounding the fiber, resulting in reduced heat transfer. **[43]** Comparing Figure 35a to Figure 35b, the initial air temperature has no effect on the *shape* of the air temperature profile as a function of *z*. Figure 35c shows the normalized centerline air temperature profiles where the normalized temperature, T_n is given by:

$$T_n = \frac{T_{measured} - T_{ambient}}{T_{set} - T_{ambient}} \quad \text{.....(8)}$$

where $T_{measured}$ is the temperature measured by the thermocouple, $T_{ambient}$ is the ambient temperature and T_{set} is the set-point temperature of the high velocity air. The normalized air temperature behaves in the same way as the velocity profile with increasing *z*. Due to ambient air entrainment and spreading effects, the air temperature and thus the heat content falls rapidly for z < 5 cm and reaches a plateau for z > 5 cm. Figures 34 and 35 illustrate that both the normalized centerline air temperature and the centerline velocity profiles are independent of the air exit temperature and are consistent with literature reports for dual air slot melt-blowing dies. **[41,42]**

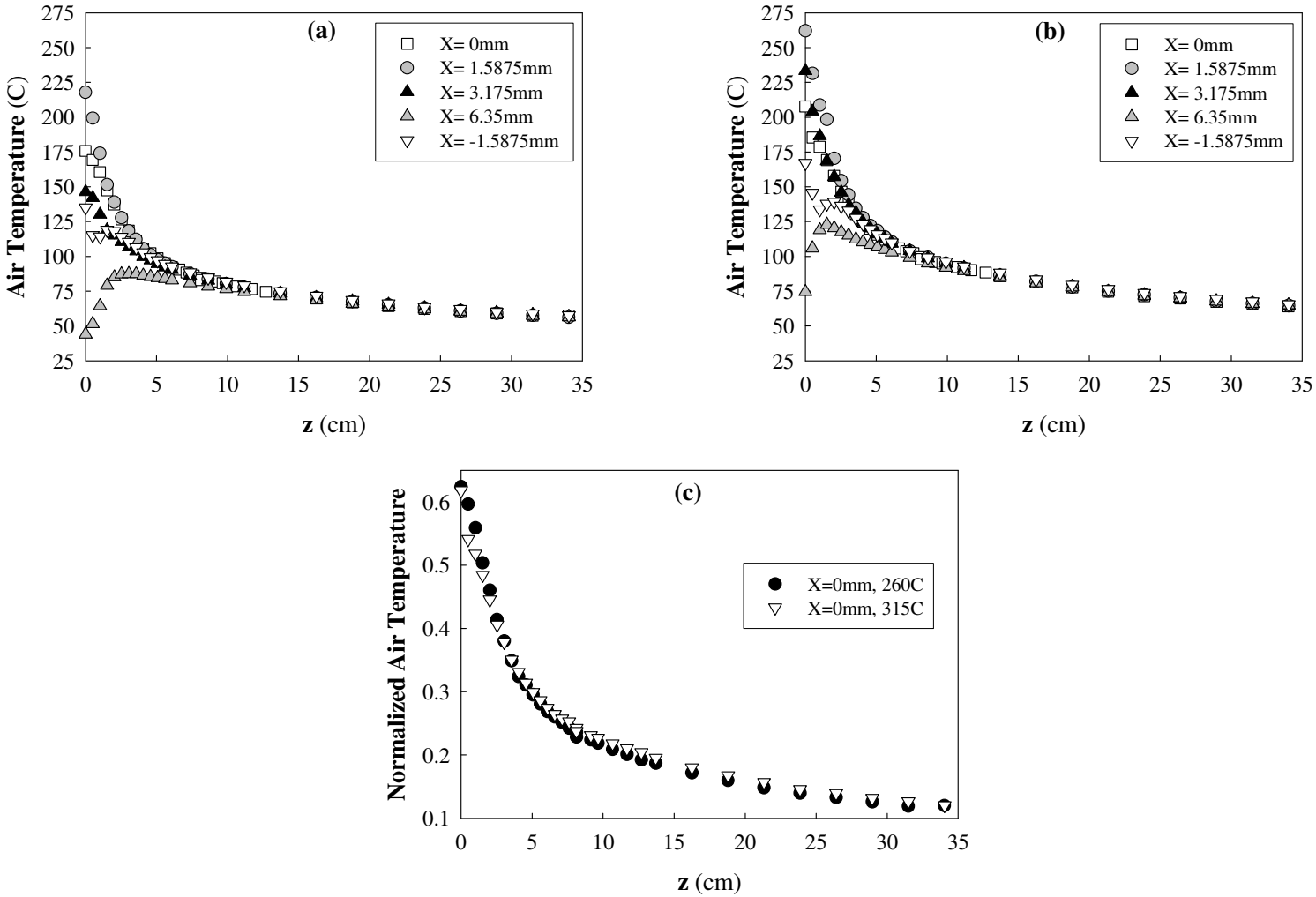

Figure 35: Air temperature profiles across melt-blowing die as a function of z (DCD) at air temperatures of 260°C **(b)** 315°C, and **(c)** normalized centerline air temperature

Increasing the air temperature surrounding a fiber, however will result in a reduced heat transfer rate from the polymer melt to the air and thus the fiber will be hotter at longer axial distances downstream.

IV. 6. Polymer Behavior

When the molten polymer stream has extended far enough below the die, the high velocity air impinges on it. At this point, the polymer has a low viscosity and is stretched rapidly due to high drag force of the air. Because rapid attenuation of polymer melt also results in reduced fiber diameter, the polymer melt cools faster in the region close to the die. In addition, convective cooling effects are dominant for $z < 5\ cm$. The resulting thin fibers cool quickly as the air temperature also drops. However, for $z > 5\ cm$ both the gradients in air velocity and temperature decrease markedly; and thus both the drag forces and the cooling rate decrease. If the drag forces drop below a certain level, the fiber ceases to attenuate. I n addition, if the polymer temperature falls below the temperature for the onset of crystallization, the fiber will begin to crystallize. At this point, the fiber diameter ceases to attenuate. If crystallization continues to a high enough extent, the fibers will no longer be tacky and will not adhere to one another upon impingement. In other words, the strength of the web builds as the fibers crystallize until a certain point is reached which occurs when the fibers cease to be tacky. If the fibers have not stuck together by this time, the web will have high loft and the fibers will be only mechanically stuck together. The web will have low strength.

Thus to form a strong web, the fibers must not complete their crystallization until after they come into contact with each other, which occurs primarily on the forming belt. It is worth noting that crystallization can begin before the forming or collector belt, but it must not proceed too far. Using the normalization method of equation (8), the temperature of the air stream was calculated for the spinning conditions used for each polymer according to the following:

$$\mathrm{T}(z) = T_n \times (T_{air} - T_{ambient})_{process} + T_{ambient} \quad \text{.....(9)}$$

and are shown as a function of z in Figure 36.

Figure 36: Air temperature profiles as a function of DCD for **(a)** PEBA, **(b)** ether TPU, **(c)** ester TPU. Ellipses indicate the position of the onset of crystallization in isothermal crystallization for each polymer as measured by DSC

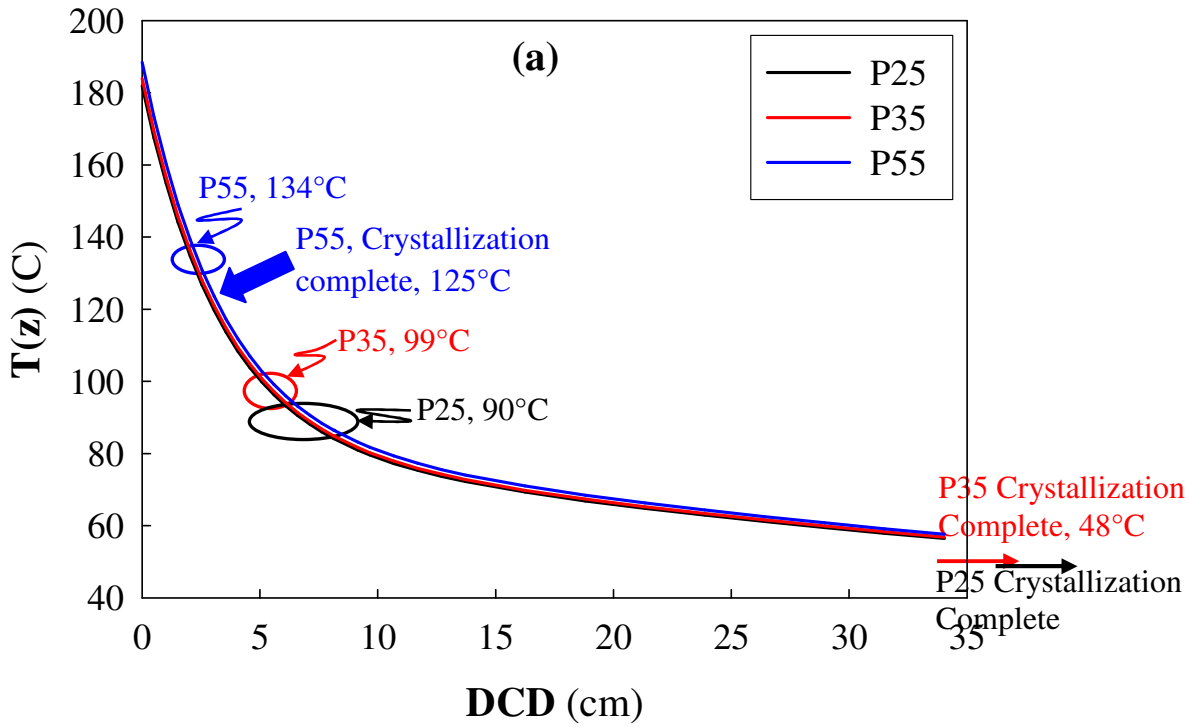
(a)
P25
P35
P55
P55, 134°C
P55, Crystallization complete, 125°C
P35, 99°C
P25, 90°C
P35 Crystallization Complete, 48°C
P25 Crystallization Complete
T(z) (C)
DCD (cm)
200
180
160
140
120
100
80
60
40
0
5
10
15
20
25
30
35

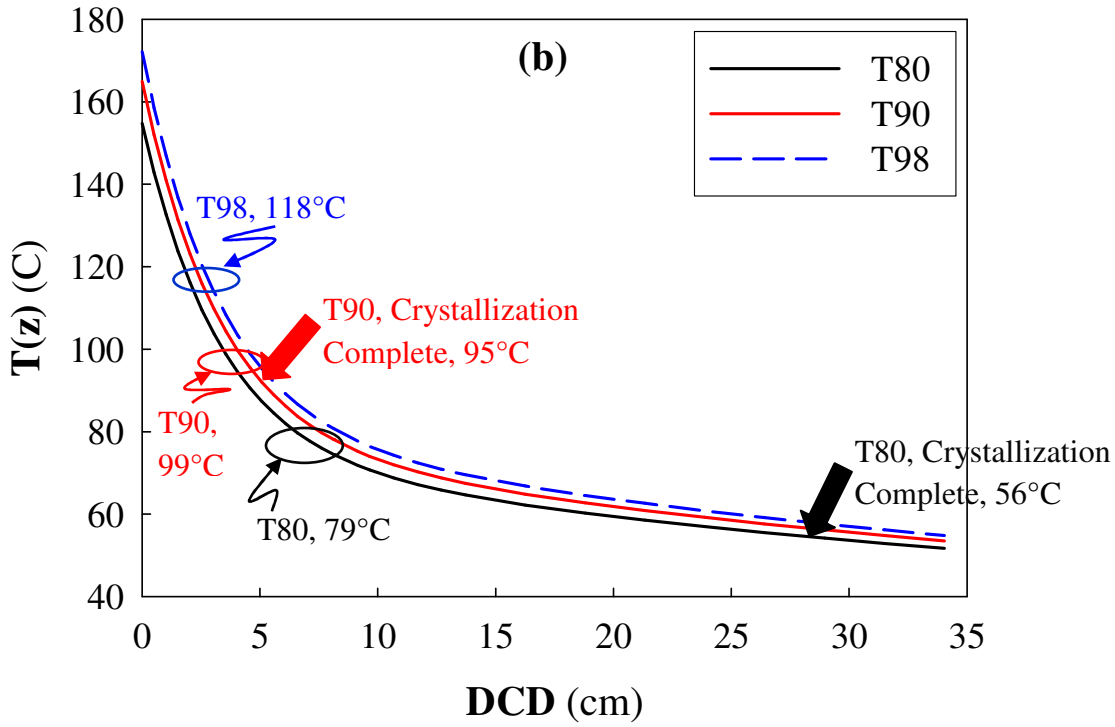
(b)
T80
T90
T98
T98, 118°C
T90, Crystallization Complete, 95°C
T90, 99°C
T80, 79°C
T80, Crystallization Complete, 56°C
T(z) (C)
DCD (cm)
180
160
140
120
100
80
60
40
0
5
10
15
20
25
30
35

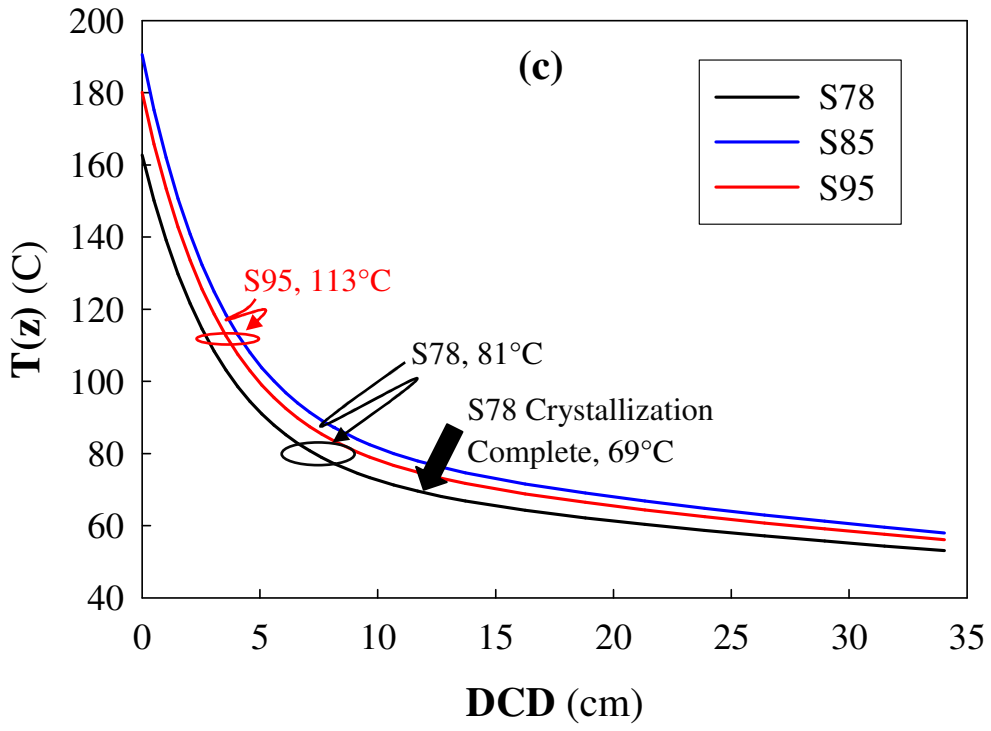

At this point, three explicit assumptions are made: (1) the fibers spend most of their time near the centerline position ($x = 0$, $y = 0$) and travel only in the z-direction parallel to the axial air velocity component (no fiber vibration and fiber moves in 1D). (2) The presence of the polymer does not affect the air temperature or velocity significantly. (3) The polymer temperature and velocity at position ($x = 0$, $y = 0$, z) is the same as the air temperature and velocity at the same coordinates. On viewing the polymer stream in the melt-blowing apparatus, assumption (1) is approximately met. If the fibers are thin enough, assumptions (2) and (3) should be approximately correct, however, the polymer temperature will be at least a few degrees warmer than the air stream. Assumptions (2) and (3) will be examined further in Section IV.8. Since all the polymers in this study are similar, the heat transfer coefficient should be similar and thus the trends in the solidification behavior should be correct, even if

the temperatures are not. Since for z > 5 cm, the temperature falls only slowly, a fourth assumption is made whereby (4) for z > 5cm, it is assumed that T_c ~ constant resulting in nearly isothermal conditions, and finally, (5) fiber-fiber interactions and DCD effects are negligible. Under these assumptions, the air temperature profiles can be used to estimate the location at which the fibers first begin to crystallize and where their crystallization is nearly complete. If it is assumed that fibers travel at centerline velocities similar to those of air, the time that it takes for the fibers to traverse the distance from the die to the collector belt is just the distance divided by the velocity. If the average velocity of the fiber is assumed to be greater than the velocity at the longest distance studied in this work, i.e. at z = 30.5 cm or v ~ 35 m/s, then the traversal time is less than 0.305m / 35m/s or less than 1 msec. This also corresponds to the maximum time allowed for crystallization to occur before the fibers reach the collector belt. Additional crystallization can occur after reaching the belt and is responsible for building fiber-to-fiber adhesion.

The crystallization onset temperatures reported in Table 2 are shown as ellipses in Figure 36 along with the air temperature profile. The crystallization half-times from Figure 14 were extrapolated linearly in temperature to a crystallization half-time of 0. These temperatures are shown in Table 9 and shown in Figure 36 with arrows. Although the extrapolation over time involves many decades, in temperature this extrapolation is only a few degrees. Next it is observed that for $z > 5\ cm$, the temperature falls relatively slowly with respect to distance. If crystallization occurs in this region, it can be assumed that the crystallization temperature T_c is approximately constant. I.e. it can be assumed that, for long distances below the die, crystallization occurs under nearly isothermal conditions.

Table 9: DSC Crystallization Temperatures at Crystallization Half-times=0sec

Sample ID		T_m (C)	Crystallization T_{onset} (C)	Crystallization T_{peak} (C)	Temperature @ $t_{0.5}$=0sec from Fig. 14
Ether TPU	T80	146.5	79.1	71.2	55.9
	T90	165	106.2	99.3	94.9
	T98	183.3	118.4	112.9	na
Ester TPU	S78	158.1	81.0	71.8	69.2
	S95	196	113.2	107.7	na
PEBA	P25	135	90.1	81.6	8.8
	P35	142	98.6	91.1	48.3
	P55	161	133.8	126.8	125.4

In Figure 36, it is clear that T_{onset} for the hard polymer grades occurs within the first *5 cm* for all polymer types reported here. T_{onset} for the medium hardness polymer grades all occur near *5 cm*, while for the softer grades T_{onset} occur at longer distances where the temperature drops slowly with increasing distance. From the data in Table 9, P55 begins to crystallize at 134°C and the crystallization half-time reaches 0 minutes at 125°C. Under the melt-blowing conditions used, P55 should have completed its crystallization before $z = 3\ cm$. This should result in a high loft fabric with very low strength since the fibers are not tacky enough to ensure sufficient fiber adhesion. This means P55 web strength should be strongly dependent on DCD i.e. decrease the most rapidly with increasing DCD. This can be clearly observed in Figure 19, where P55 is the weakest web and increasing the DCD i.e. to $z = 20\ cm$ it has nearly zero strength. At longer distances, webs could not be made from P55 as they were too weak to remove from the collector. The onset of crystallization for both S95 and T98 occurs at much lower temperatures, 113 and 119°C, respectively. Although the crystallization half-times could not be determined for these polymers, it is clear that their crystallization is

delayed over that of P55. Thus, they should form stronger webs than P55 since the fibers in these webs will have a better opportunity to adhere. However, as the distance between the die and the collector increases, their strengths should decrease rapidly. As seen in Figure 19, this behavior is indeed observed. For the softer grades, crystallization begins at lower temperatures, which correspond to longer distances below the die. P35 begins to crystallize at 99°C while P25 begins at 90°C. These temperatures occur approximately 6 and 7 cm below the die, respectively. The completion of crystallization should not occur until after these polymers reach the forming belt since the temperature where the crystallization half-time reaches 0 min is below the maximum travel distance from the die to the belt. In other words, they should form well adhered webs and the inter-fiber adhesion should be nearly independent of the distance between the collector and the die. This behavior is precisely what is observed in the tensile test results in Figure 19, where there is nearly no dependence of the strength on distance. The soft grades of the ether and ester TPUs have lower crystallization onset temperatures than the PEBA series, but the temperature at which their crystallization half-times reach 0 minutes is higher than the PEBA series. This means that they should form well adhered webs, but the dependence on z should be greater than observed for the PEBA series. Indeed, T80 and S78 both form strong webs, but their web strength has a significant dependence on z, unlike the PEBA series.

Finally, T90 has a crystallization onset temperature of 99°C and temperature at which its crystallization half-times reach 0 minutes is 95°C. This implies that it should form a web with better inter-fiber adhesion than the P55 webs. In addition, the high crystallization completion temperature indicates that the slope of the web strength vs. z curve should be

quite large. Again this behavior is exactly what was observed as shown in Figure 19b. However, one should expect a very weak web based on this model. This discrepancy can be explained by noting that crystallization takes a finite amount of time, hence delaying the time for the completion of crystallization.

Web strength also depends strongly on the polymer hardness as seen in Figure 19. At a single DCD, increasing polymer hardness increases the web strength for ether and ester TPUs. Because TPUs require more time for crystallization than PEBA, the polymer hardness contributes to the web strength and increasing hard segment content leads to a stronger web. In contrast, at a given DCD, the web strength of PEBA decreases with increasing polymer hardness. Since all factors except polymer hardness remain unchanged, this unexpected tensile behavior is attributed to differences in the crystallization kinetics with changing polymer hardness.

IV. 7. Elastic Properties

Tensile set or deformation behavior of PEBA, ether and ester TPU melt-blown webs at various extensions and DCDs are shown in Figures 36-40. The procedure for measurement of the tensile set and elastic limit was described in section III.4.3.2. based on Eqn. 5:

$$\%\ \text{Tensile Set} = \left(\frac{\text{Recovered Length} - \text{Initial Length}}{\text{Initial Length}}\right) \times 100 \quad \ldots\ldots\ldots\ldots\ldots\ldots\ldots\ldots (10)$$

Elastic limit was extrapolated from the regression fit of % tensile set plotted as a function of given extensions. In these figures, the tensile set is an indication of the permanent deformation i.e. upon stress removal the length of web specimen will be % tensile set value

larger than the original dimensions.

As seen in Figures 37-39, for all studied polymer systems, the tensile set or degree of permanent deformation is relatively independent of DCD but increases with increasing extensions and polymer hardness grade. This is further illustrated in Figures 40and 41, where the % elastic limit value represents the % elongation beyond which the web will be permanently deformed, the degree of which is determined by the applied extensions. As seen in Figures 40 and 41, the % elastic limit values become much lower with increasing crystallinity in the order of S95<S78 for ester TPUs, T98<T90<T80 for ether TPUs, and P55<P35<P25 for PEBA series. I.e. the polymers with lower hard segment content: S78, T80 and P25 exhibit better elasticity and lower tensile set. This is expected since more hard segments will undergo plastic deformation with increasing hard segment content. With increasing extension, on the other hand, greater deformation energy acts on the fibers within the web resulting in more disruption and break up of the short fibers, the extent of which depends on the applied extensions. Since studied extensions are well above the elastic limit values for all polymer grades (within the non-linear region of the stress-strain curves in Figures 16-17), the observed tensile set behavior is an indication of the contribution of polymer hardness and how well the fibers adhere to each other within the web to reduce the slippage and breakage upon stress application.

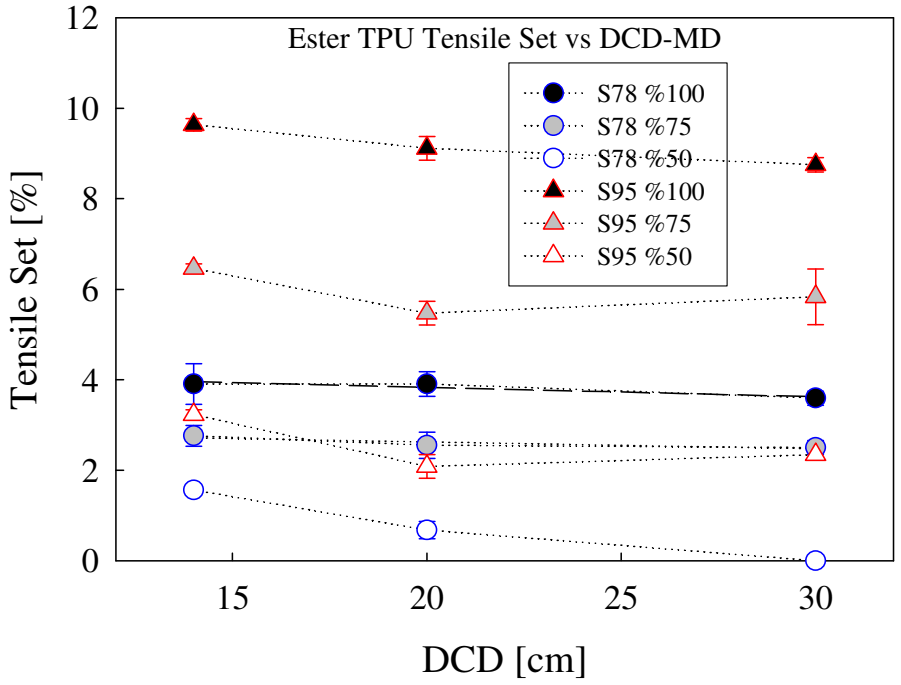

Figure 37: Tensile set of ester TPU webs in MD vs DCD and elongation (50-100%)

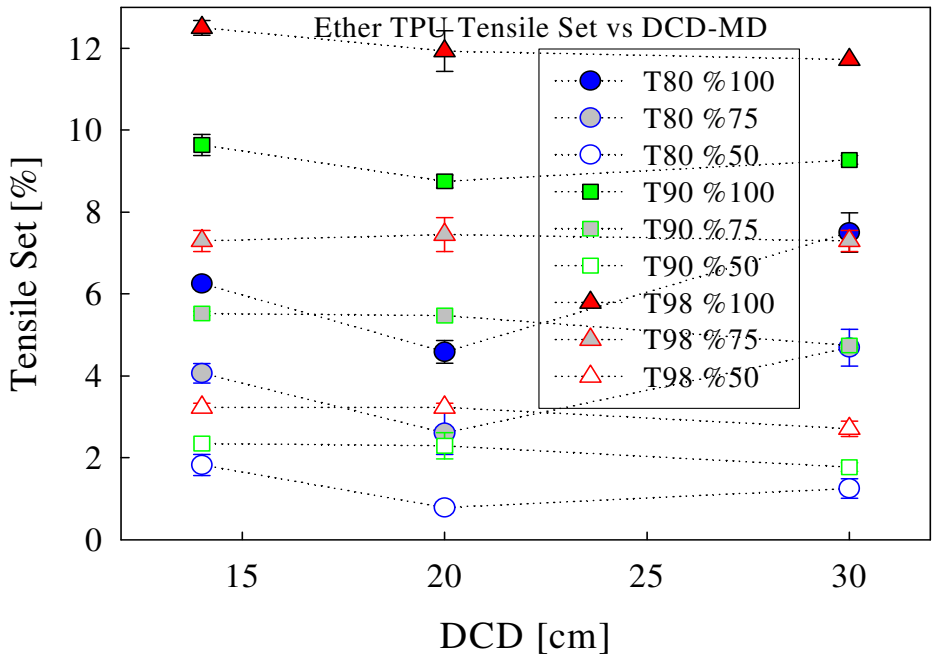

Figure 38: Tensile set of ether TPU webs in MD vs DCD and elongation (50-100%)

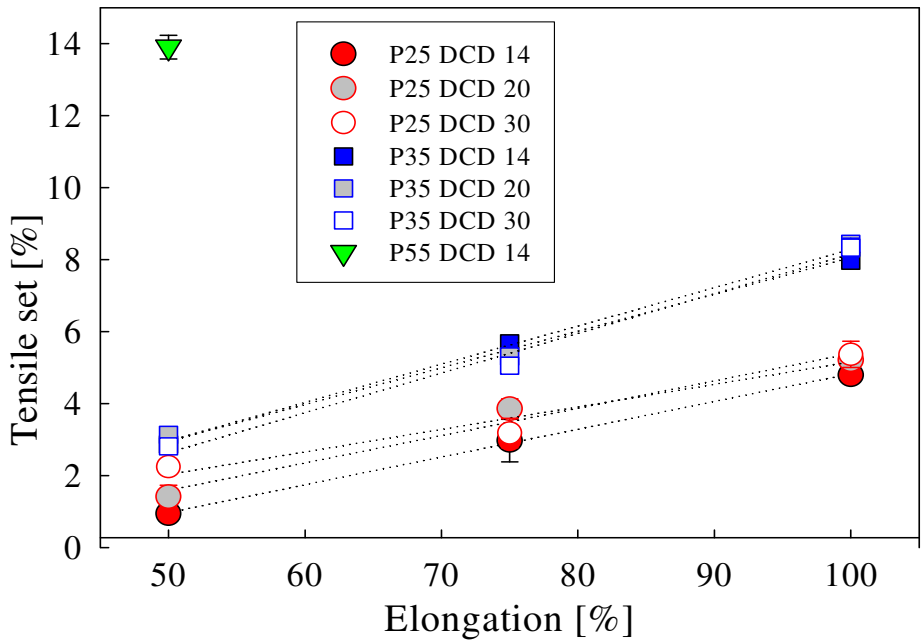

Figure 39: Tensile set behavior of PEBA melt-blown webs in MD vs elongation

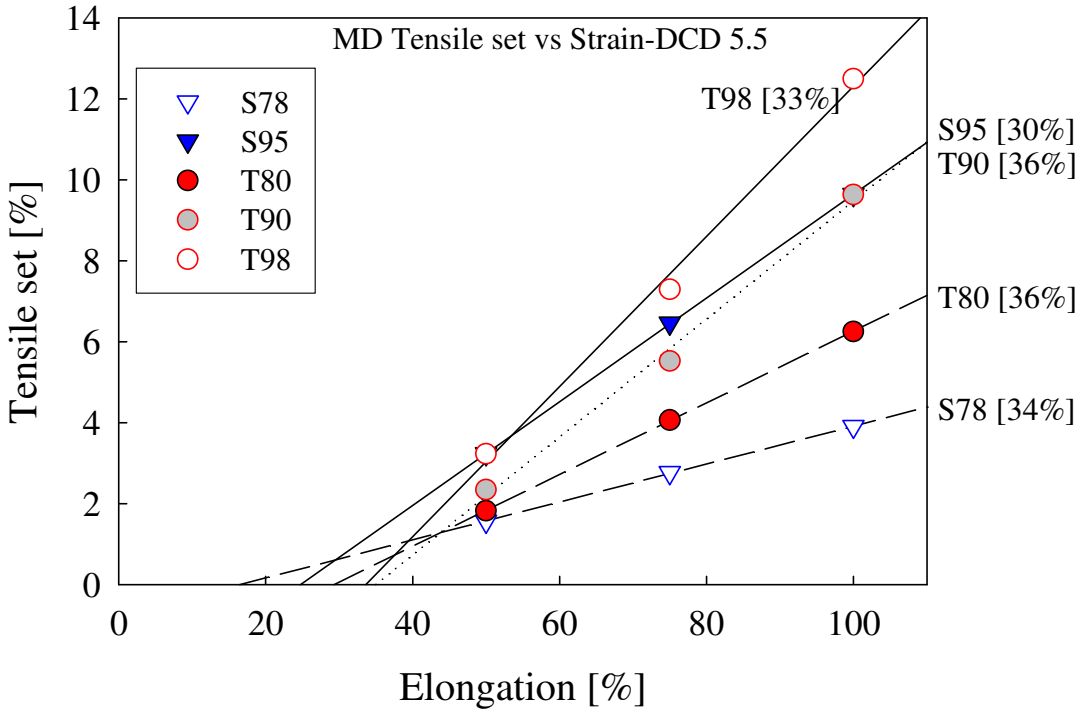

Figure 40: Tensile set of ether & ester TPU webs in MD, DCD 8inches at 50-100%. Numbers in brackets represent percent elastic limit

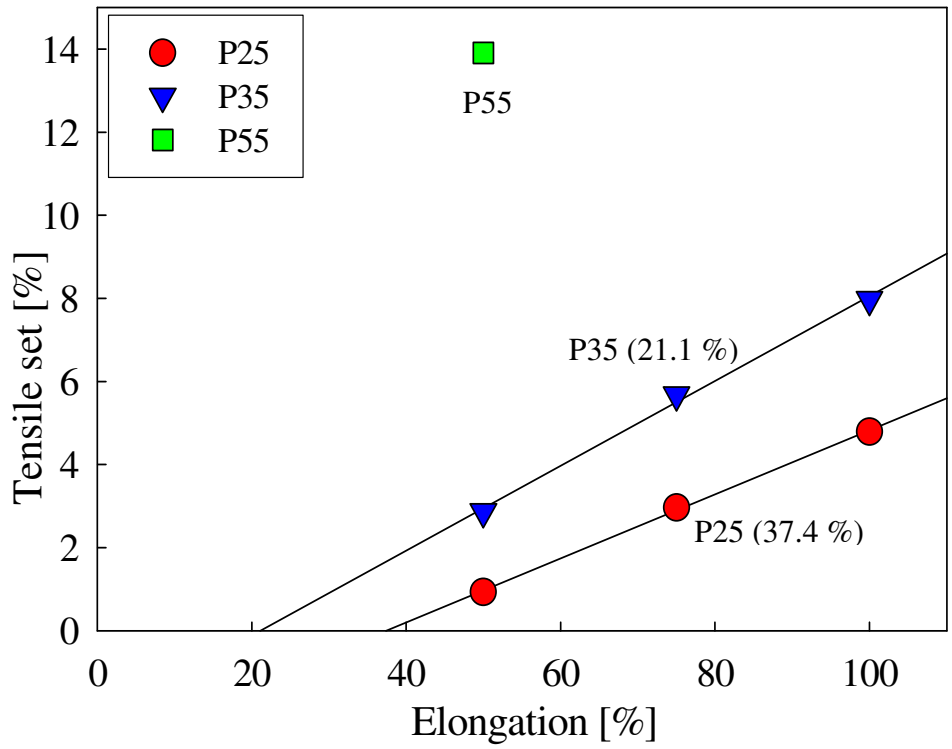

Figure 41: Tensile set of PEBA webs in MD, DCD 5.5inches at 50-100%. Numbers in brackets represent percent elastic limit

IV. 8. Melt-Blowing Simulations

In the earlier sections, the strong dependence of the fiber formation process and web strength on the interaction between the air flow field and polymer characteristics was discussed. To illustrate this relationship, on-line measurements of the air velocity and temperature profiles were correlated to DSC crystallization behavior of the TPU and PEBA elastomeric polymers. However, the air temperature and velocity profiles were measured without the polymer fiber and the effect of the presence of the polymer fiber on the air flow field was ignored since the polymer melt is attenuated very rapidly to fine diameter fibers. Moreover, it was assumed that the polymer melt temperature at position (x, z) is the same as the air temperature at position (x, z). But, fiber temperatures will be hotter than observed air temperatures, and thus

polymer crystallization will be delayed somewhat. Expensive techniques such as thermal imaging and Doppler velocimetry are required to make measurements with the inclusion of the polymer fiber and present difficulties at positions very close to the melt-blowing die. Unfortunately, these methods were not available for this study. Thus, modeling was used to provide the most cost effective and simplest technique to predict the polymer fiber temperatures below the die and answer how much polymer crystallization will be delayed.

The literature of modeling air and polymer flow field in melt-blowing has been dominated by Shambaugh and coworkers. Uyttendale and Shambaugh **[1]** developed a 1D model based on the steady-state solution of continuity, momentum and energy equations to predict fiber temperature and diameter profiles in melt-blowing at relatively low air velocities. They also showed that the polymer rheology can be approximated by the purely viscous Newtonian model rather than the viscoelastic model. **[48, 80]** This was attributed to very rapid fiber temperature changes in melt-blowing and that the temperature dependence of the polymer viscosity dominates fiber attenuation over visco-elastic effects. Rao and Shambaugh **[79]** extended this 1D model to 2D to include the transverse fiber vibrations at high air velocities and fiber breakage. In subsequent work **[80]** the model was expanded to predict 3D and time-dependent fiber motion. But, 1D Newtonian model was found to be as good as both 2D and 3D Newtonian models in predicting the fiber attenuation in melt-blowing at low air velocities when fiber vibrations are small. Using this model, Bansal and Shambaugh **[43]** showed favorable agreement between simulation results and experimental fiber diameter and temperature profiles. Marla and Shambaugh **[48]** also used this model to analyze the performance of a slot die.

In a series of dual-slot die modeling work, Krutka et al. **[45-47]** found that Reynolds Stress Model (RSM) can be used to predict the turbulent air flow field of a sharp die configuration but model default parameters suggested in Fluent software needed to be calibrated to obtain good qualitative agreement with the experimental data. Moore et al. **[81]** examined isothermal air flow field from different annular die geometries by further modifying RSM model parameters. Krutka et al. **[82, 83]** studied the velocity and temperature fields from multi-hole annular dies using the k-ε turbulence model, which predicted the centerline velocity decay as good as more sophisticated RSM model. The velocity and temperature field from multi-hole was also found to be quite different from that of the single jet. In a recent study, Krutka et al. **[84]** modeled the interactions between the turbulent air flow and polymer fiber for an annular die. They found that the polymer fiber affects the air flow field and air drag force at regions close to the die face.

In this study, commercial software Fluent 6.1.22 and Fiber Model was used to model the air and polymer flow field. Similar to 1D melt-blowing model developed by Uyttendale and Shambaugh **[1]**, Fluent Fiber Model uses a 1D approach based on the steady-state solutions of fundamental equations of the mass, momentum (force), and energy balance, originally developed for melt-spinning. **[85]** These tensile forces that act to deform the polymer fiber only in the axial direction are balanced by the inertial forces due to acceleration of the fiber, aerodynamic forces due to friction between the fiber and surrounding air moving with different velocity, and gravitational forces. **[86-90]**

Despite the take-up roll that provides attenuating force on the polymer melt in melt spinning is replaced by the high velocity heated air in melt-blowing, the fundamental equations developed for melt-spinning can be used to model fiber formation in melt-blowing as demonstrated by Shambaugh and coworkers. **[1, 43, 79, 80]** These studies suggested that the tensile forces can be balanced around the distances below the die where the polymer temperature reaches the solidification temperatures, beyond which fiber attenuation becomes negligible due to rapid increase of the viscosity of the crystallized fiber. Beyond solidification distances, fiber diameter and velocity profiles remain relatively constant. Similarly, Fiber model predicts the tensile forces that provide fiber attenuation to be applied at take-up point as fiber solidification distance.

In melt-blowing high velocity hot air impinges on the molten polymer as it exits from the nozzle. Because of the velocity difference between air and polymer melt, the resultant stress on the polymer melt elongates it to finer diameters very rapidly at distances close to the die. This means for the case of very high speeds used in melt-blowing, air drag force dominates the fiber attenuation over inertial and gravitational forces. **[1, 43, 79, 80]** With significantly high speeds in melt-blowing, the importance of the air drag was recognized by Majumdar and Shambaugh. **[91]** They modified the original Kase and Matsuo model in equation 11 to melt-blowing of speeds up to 18,000m/min with transverse fiber motions by defining the velocity, *V* in *Reynolds number* to relative velocity, V_{rel} as in equation 12. The original Kase-Matsuo correlation was developed to predict the air drag force on a stagnant wire as a result of the parallel air flow. **[89, 90]**

$$C_{f,par} = \beta(\mathrm{Re}_{rel})^{-n} \qquad \text{……..(11)}$$

Where C_f is the axial air drag coefficient in parallel flow at the turbulent air-fiber interface, β the leading coefficient constant, Re_{rel} is defined as

$$\mathrm{Re}_{rel} = \frac{\rho_{air}.d_{fiber}\left|V_{air} - V_{fiber}\right|}{\eta_{air}} \qquad \text{……..(12)}$$

Where η_{air} (Pa.s) is the dynamic viscosity of air, ρ_{air} (kg/m^3) air density, d_{fiber} is fiber diameter, and V_{air} (m/s) and V_{fiber} (m/s) axial air and fiber velocity, respectively.

Uyttendale and Shambaugh **[1]** reported more fiber attenuation and better fiber diameter predictions when β was increased from Kase-Matsuo value of 0.37 to 0.6 at low air velocities. Majumdar and Shambaugh **[91]** suggested that for melt-blowing conditions of high air velocities $\beta=0.78$ is appropriate in describing the significance of air drag force on the polymer melt. Rao-Shambaugh and Marla-Shambaugh **[79, 80]** also used $\beta=0.78$ in 2D and 3D modeling of air flow field. Bansal and Shambaugh **[43]** improved fiber diameter predictions by using β=0.78 but adjusted default value of the heat transfer coefficient to match experimental fiber temperature profiles. In a recent simulation study of annular die configuration, Krutka et al. **[84]** proposed β values in the range of 0.79-1.44. In agreement with these studies, Fluent Fiber Model uses β=1.24 and Re_{rel} is computed based on the relative velocity of the surrounding parallel flow as shown in equation 12 above.

IV. 8. 1. Air Flow Field Simulation

Figure 42a shows the computational domain used in the simulations, which was based on the melt-blowing die configuration in Figure 3.

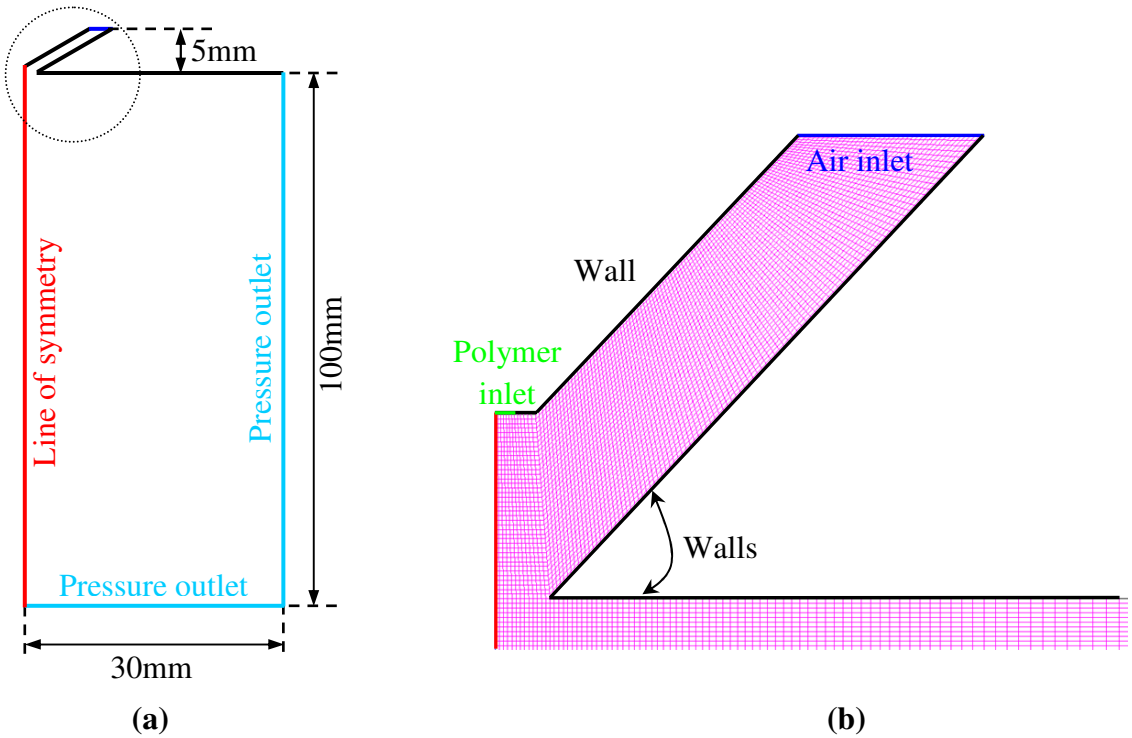

Figure 42: (a) Computational domain used for simulations, **(b)** close view of the grid resolution of the areas close to die face shown in dotted circle in (a)

The origin of the coordinate system is at the center of the air plates for the experimental measurement and simulation of the air velocity and temperature profiles. The *y*-direction is parallel to the air slots, while the *x*-direction (MD-machine direction) is across the die face. The positive *z*-direction (not shown) is downward direction below the melt-blowing die. A number of studies **[44-47]** reported that a melt-blowing die having a large air slot length-to-width ratio can be assumed to have infinite length and thus can be modeled as 2D. Since the aspect ratio of the melt-blowing die used is large i.e. l/b =1169.8, the die and flow field can

be modeled as 2D.

Because the polymer fiber spends most of its time at the *x=0* plane during attenuation and until reaching the collector, the domain dimensions were based on the measured velocity and temperatures at the centerline (*x=0*) (see Figures 34 and 35). Similar to Krutka et al **[45-47]**, the dimensions of the domain were 100mm and 30mm in *z* and *x*-direction, respectively. These dimensions are large enough to represent the experimentally measured air velocity and temperature profiles shown in Figures 34 and 35. In measuring the air temperature and velocity profiles, the die temperature was 260°C, while the air temperature was 260°C at a flow rate corresponding to 50% of the pump speed. These parameters approximate the processing conditions used in melt-blowing PEBA and ether TPU polymers, as shown in Table 10. Once the simulation results were validated by experimentally measured air velocity and temperature profiles, the polymer fiber was included to investigate the fiber temperature and diameter profiles.

Table 10: Melt-blowing Process Conditions and simulation results

Sample ID		**Die Temp** (C)	**Air Temp** (C)	**Air FR** (%)*	V_{max} (m/s)	**Polymer FR** (kghs)†	**Fiber Diam.** (μ)	V_{fiber} (m/s)
Ether Elastollan® TPU	T80	233	221	70	337	8.33e-06	5.00	382
	T90	251	241	70	337	8.33e-06	5.00	376
Ester Elastollan® TPU	S78	253	230	70	334	8.33e-06	9.10	109
	S95	262	261	50	257	8.33e-06	7.40	160
PEBA (Pebax®)	P25	287	258	25	98.7	4.00e-06	15.3	23.9
	P55	312	274	20	44.5	4.00e-06	16.3	21.2

*% of the pump speed in melt-blowing line
†kghs is kilograms per hole per second

The computational domain grid was generated in Gambit and quadrilateral cells were used. Since the 2D flow of two converging jets is symmetric about the $x=0$ plane, the left boundary in Figure 42a was designated as line of symmetry. This line of symmetry is also assumed to coincide with the path of the polymer fiber traveling in z-direction until reaching the collector. As suggested by Krutka et al. **[45-47]**, the grid resolution was the finest in the regions close to the air discharge and die face as seen in Figure 42b, where the air jets from the two individual slots converge. The grid cells within the air slots and just below the die face was 0.005mm by 0.005mm and was graded to coarsen the grid resolution for regions away from die face and line of symmetry, as can be observed in Figure 42b. The air temperature and velocity profiles were considered as boundary conditions and only z-components (axial) were used as input parameters. The air flow entering the domain 5mm above the air plate face was defined as the pressure inlet at boundary conditions of 264°C and 0.293atm pressure. The nonisothermal air flow was modeled as compressible flow and its density and viscosity were determined by using the ideal gas law and kinetic theory, respectively. The bottom and right boundaries were pressure outlets at atmospheric conditions of 21°C and 1atm pressure. All other boundaries were defined as walls. Even though the presence of the polymer was ignored in air flow field simulations, the polymer nozzle and die face were defined as walls having temperature of 260°C. In the simulations, the residuals converged to the order 10^{-7}.

Figure 43 shows the centerline air velocity and temperature profiles for different grid resolutions to examine the grid-independency of the simulation results.

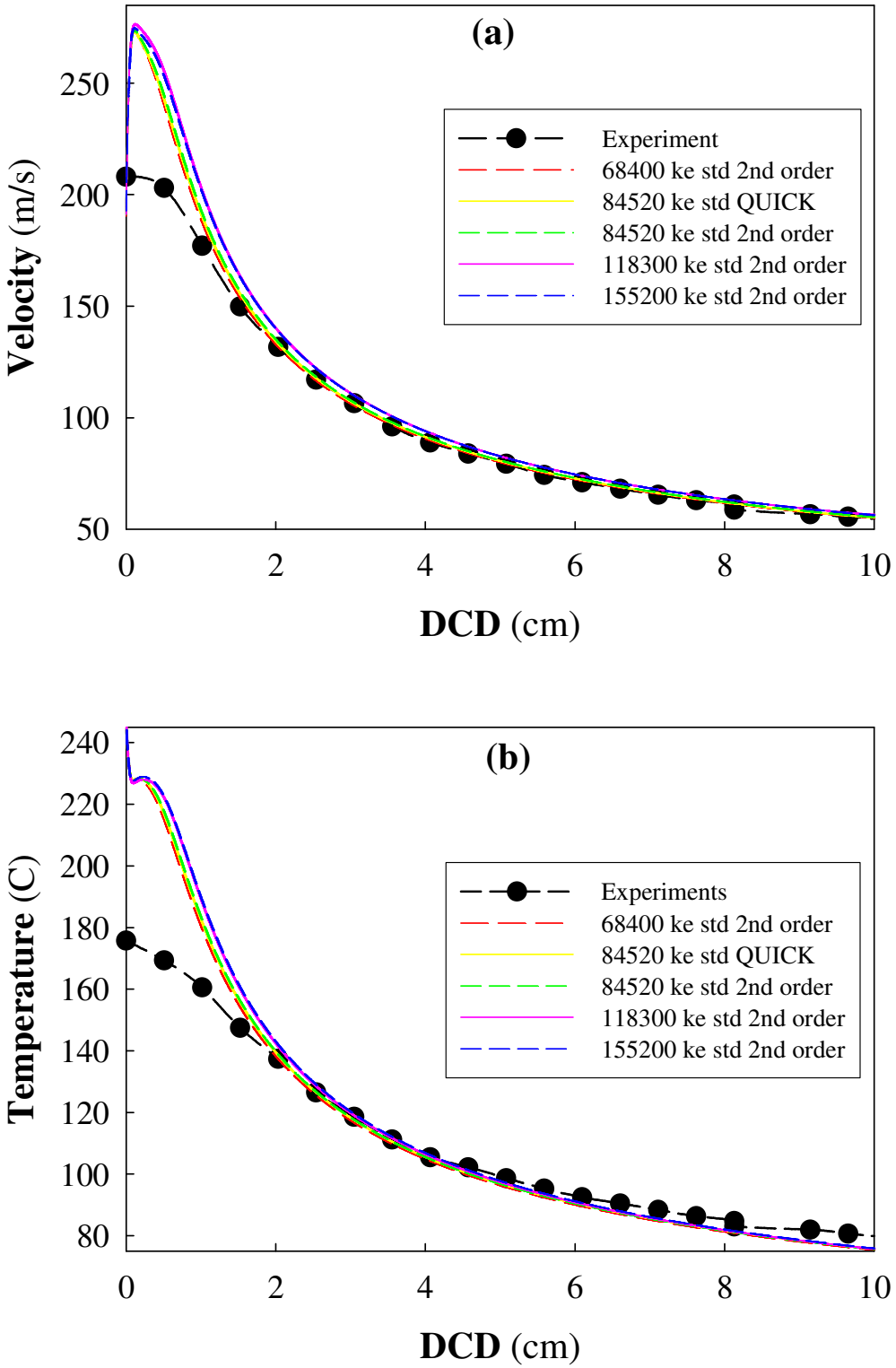

Figure 43: (a) Air velocity and **(b)** temperature profiles for different grid resolutions (standard k-ε model, second and third (QUICK) order discretization scheme)

Four different mesh sizes were examined using the same simulation parameters and boundary conditions: 68,400 cells, 84,520 cells, 118300 cells and 155200 cells. As seen in Figure 43, the results for the two lower resolutions: 68,400 cells, 84,520 cells and the two higher resolutions: 118,300 cells and 155200 cells are identical. And, there is almost negligible difference between the lower and higher resolution results to assume that the higher resolution does not affect the results. Because 118,300 cells and 155200 cells give identical results, the grid with the 118,300 cells was used in the simulations to save computational time. This resolution was found fine enough to describe grid-independent flow field of two converging jets from a dual-slot melt-blowing die of a similar configuration. **[46, 47]** Also, the results with third-order (QUICK) discretization scheme are identical to those of second-order schemes. This indicates that second-order scheme is as accurate as the third-order one.

Figure 43 also shows that for all resolutions examined, the agreement between the simulation and experimental results is very good except at distances very close to the die surface. Within the distances of 1.5cm below the die, the simulation over-predicts both the air velocity and temperature. To examine the reason for this over-prediction and determine the most suitable turbulence model that describes experimental air velocity and temperature profiles, both 84,520 cells and 118,300 cells were run with different turbulence models offered by Fluent 6.1.22: standard k-ε model, realizable k-ε model and Reynolds Stress Model (RSM). The details of these turbulence models can be found in Fluent 6.1.22 tutorial. **[85]**

Figure 44 shows the simulation results for the centerline air velocity and temperature profiles with different turbulence models by setting the model parameters to default values. Further, velocity and temperature field contours colored by the magnitude are illustrated in Figure 45.

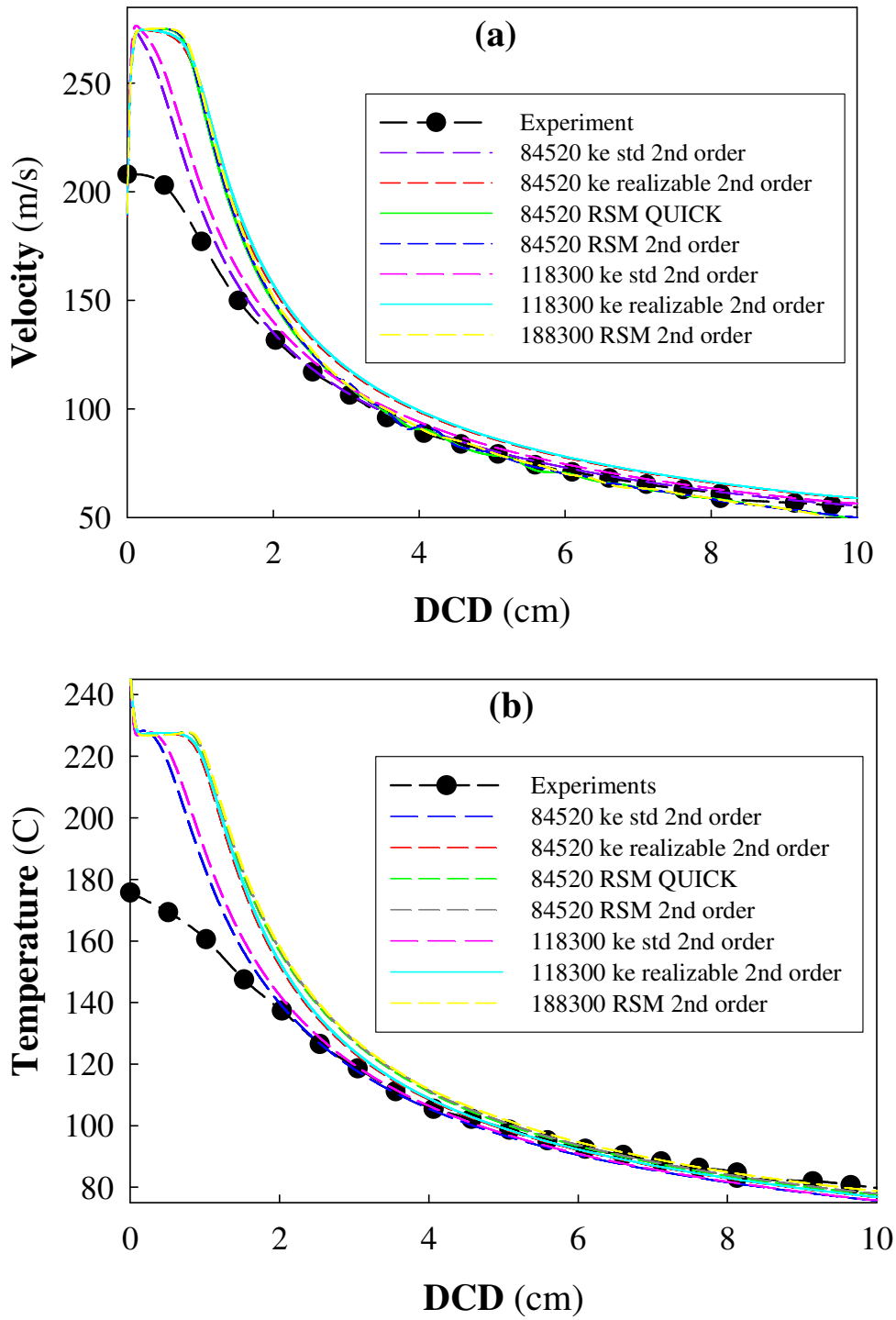

Figure 44: Comparison of different turbulence models to the experimental data **(a)** velocity, **(b)** temperature profiles with the k-ε standard model (model parameters set to default values)

As clearly observed in Figure 44, the simulation profiles are in good agreement with the experimental results within the examined region below the die face, but the values are different within the first 1.5cm for all different turbulence models.

For all examined resolutions, the standard k-ε model with default settings provided better fit to the experimental velocity and temperature profiles than those of realizable k-ε and RSM model. The realizable and RSM models failed to predict a smooth velocity decay profile at further distances away from the die face where the simulation. This is in agreement with Krutka et al. **[82, 83]** who reported that simpler *k-ε* model with default parameters was satisfactory for simulations of air flow field from annular geometry. An alternative explanation of the lack of agreement within the first 1.5cm below the die can be attributed to the limited upper velocity range of the pitot tube of around 210m/s and experimental difficulty of measuring the air velocity and temperature very close to the die surface.

Figure 45 displays air velocity and temperature contours for the whole domain and closer to the die face. From velocity contours in Figure 45a, it's clear that the air jets from the two individual air slots completely merged into a single centerline jet just below the die face within the first 1-2mm, where the maximum peak in the air velocity profile is observed. This is expected due to recessed, sharp die configuration. **[41, 42, 44-49]** The distance from the melt-blowing die at which individual air jets merge to produce the maximum centerline velocity for a sharp, flush die configuration was correlated to die angle by Krutka et al. **[47]** as follows:

$$z_{\max} = 0.0629\Phi - 0.875 \quad (13)$$

where Φ is the die angle or the angle between the two converging air streams.

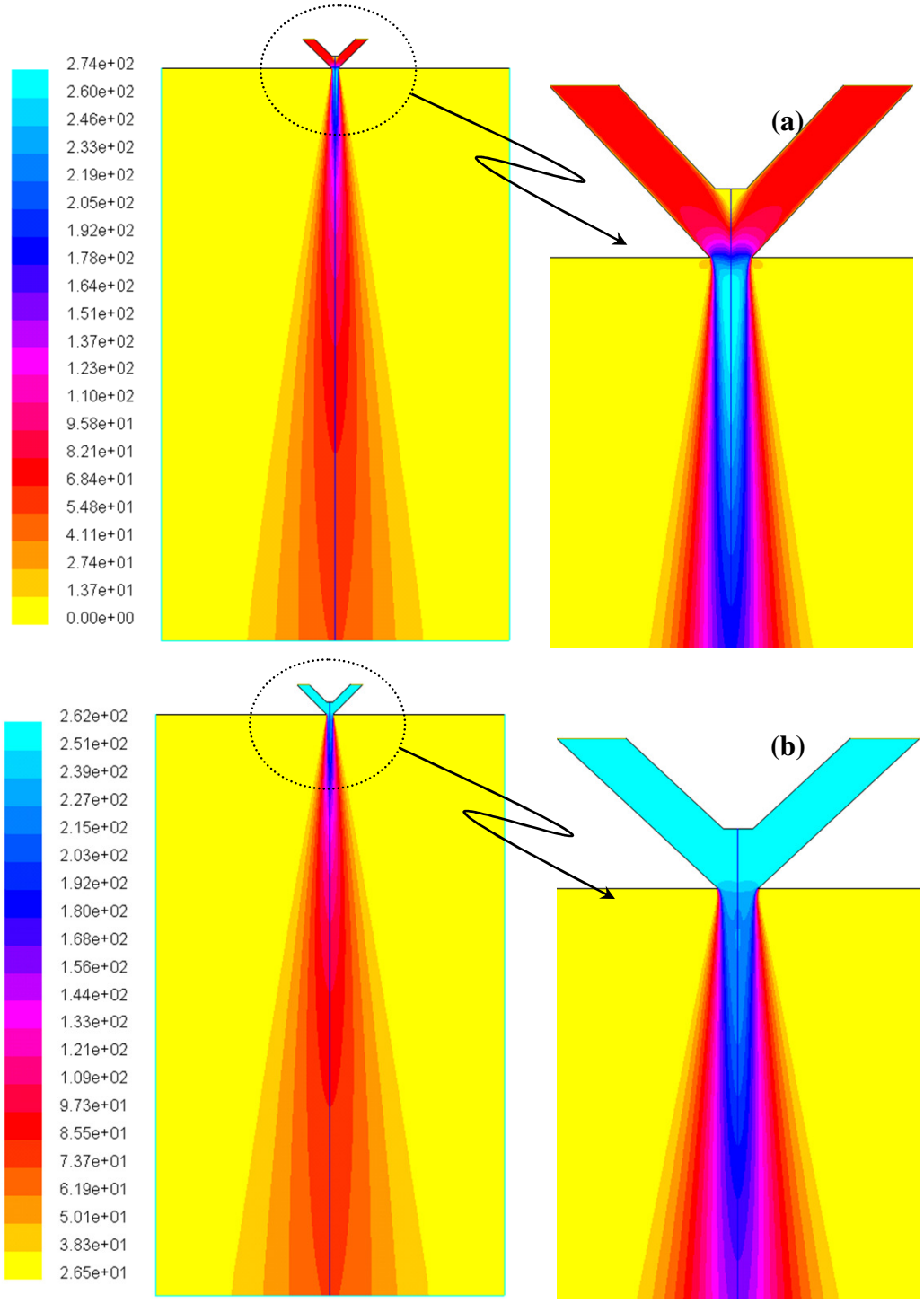

Figure 45: (a) Velocity (velocity magnitude, m/s) and **(b)** Temperature (static temperature, degrees Kelvin) contours for air flow field. 118,300 mesh resolution, k-ε standard model (default values), second-order discretization scheme. The images on the left are the whole domain of 3cmx10cm across and below the die face.

For our melt-blowing die angle of 45º, our simulations should produce z_{max}=1.96mm, while the maximum is observed at 1.42mm. This is as expected due to recessed configuration of the die used, which is shown to produce maximum velocities at closer distances than flush dies. Since polymer melt having low viscosity meets directly with this maximum air velocity when exiting the die, air drag force acting upon the polymer melt will be the greatest, thereby providing the most significant fiber attenuation rate i.e. fiber diameter reduction. **[47, 48, 52]** The maximum axial fiber elongation rate and rheological stress were also shown to correspond to around the same distances below the die, regardless of the presence of fiber vibration, and moved to closer distances to the die with increasing air velocities. **[48]**

The processing conditions employed in melt-blowing ether TPU, ester TPU and PEBA elastomeric polymers are shown in Table 10 These parameters were used as inputs to simulate the air flow field for each specific processing conditions used in processing these polymers. The die temperatures seen in Table 10 were used as the polymer melt temperatures at the nozzle exit. The die temperatures were shown to be accurate in representing polymer melt temperature exiting into melt-blowing air flow field. **[92]**

Figure 46 shows air velocity and temperature profiles as a function of different domain dimensions: 30mm in the *x*-direction, and 140mm, 200mm, and 300mm in the *z*-direction, which represents three different die-to-collector distances (DCD) used in melt-blowing TPU and PEBA polymers. The 118,300 mesh resolution used for domain 30mmx100mm for experimental verification was scaled to these dimensions in the *z*-direction. Resulting mesh resolutions for DCD 140mm, 200mm, and 300mm are 160,600 cells, 198,200 cells, and 235,800 cells, respectively.

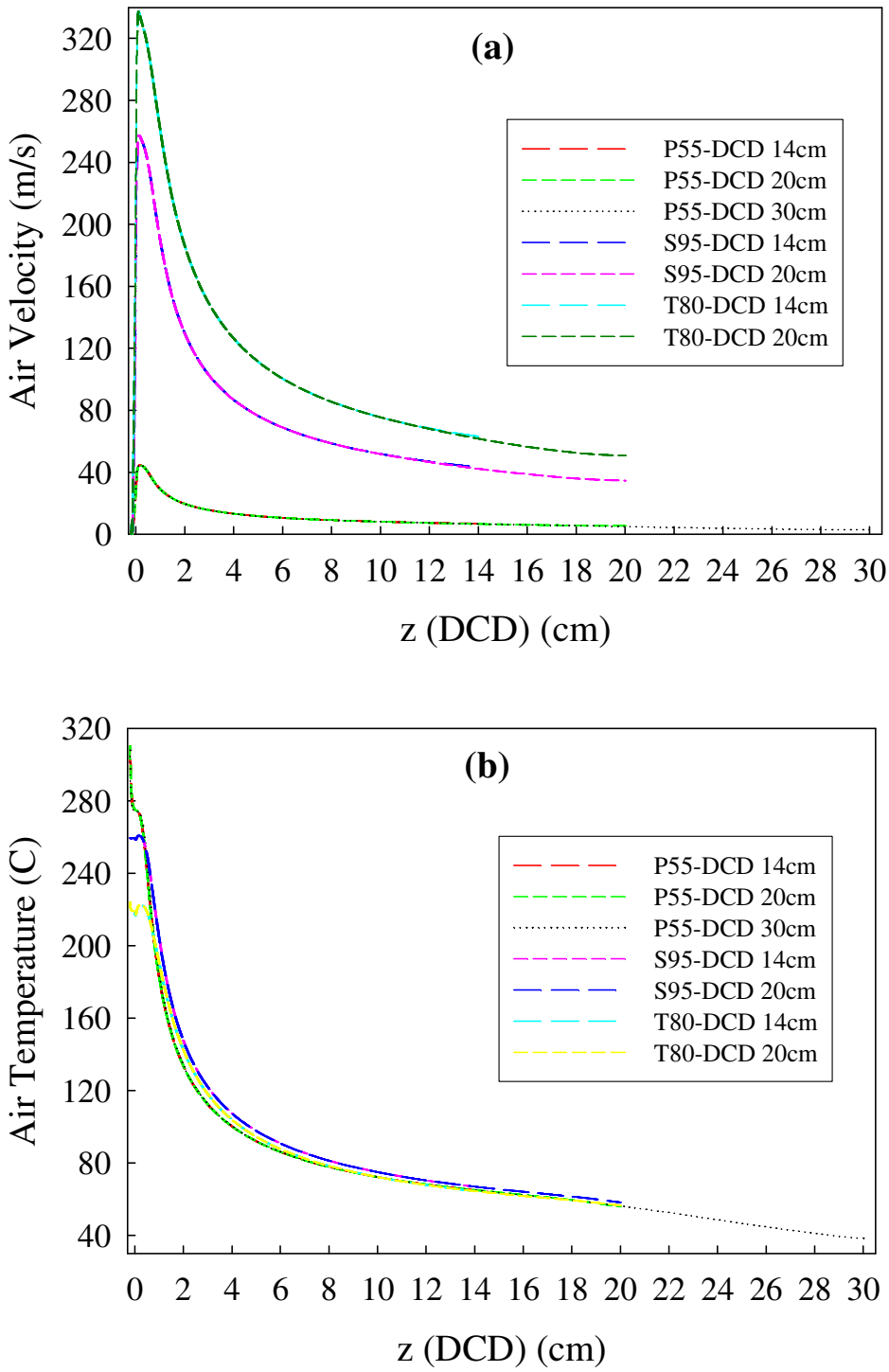

Figure 46: **(a)** Air Velocity (velocity magnitude, m/s) and **(b)** temperature (static temperature) profiles for P55, S95 and T80 processing conditions. k-ε standard model (default values), second-order discretization scheme

As seen in Figure 46, air flow rates used in melt-blowing PEBA and TPU elastomers in the range of %20-70 produced average discharge velocities from 33.2m/s to 230m/s ($x=y=0$), respectively. The air streams from the two individual air slots completely merged into a single, maximum centerline jet below the die face within z=0.998mm to z=1.565mm with corresponding maximum air velocities of 337m/s to 44.5m/s for TPU and PEBA series, respectively, as shown in Table 10. As expected, with increasing air flow rates the maximum air velocity and merging positions moved to nearer distances to melt-blowing die. In Figure 45, air velocity and temperature profiles were illustrated for only T80, S95 and P55 since the air flow rates and temperatures used in melt-blowing these polymers cover the velocity and temperature ranges shown in Table 10.

IV. 8.2. Polymer Melt Simulation-Fiber Modeling

Once the air flow field simulations converge, Fiber model was activated to include and model the polymer fiber from a single nozzle of having diameter 0.381mm. The interaction between the adjacent filaments in multi-hole extrusion was assumed to be negligible. The simulations were run by using actual melt-blowing conditions of TPU and PEBA polymers as summarized in Table 10.

Since the Fluent Fiber Model requires specification of the fiber velocity at the take-up or solidification coordinates, the fiber diameters and distributions were measured using NCRC Image Analysis software from SEM images of melt-blown webs. **[56]** SEM images were provided by BASF and Arkema and 100 diameter measurements were obtained for each polymer type. A typical SEM image of melt-blown web and fiber diameter distributions are

shown in Figures 47 and 48. The fiber diameter distribution data is comparable with those obtained for melt-blown fabrics made with more conventional polymers.

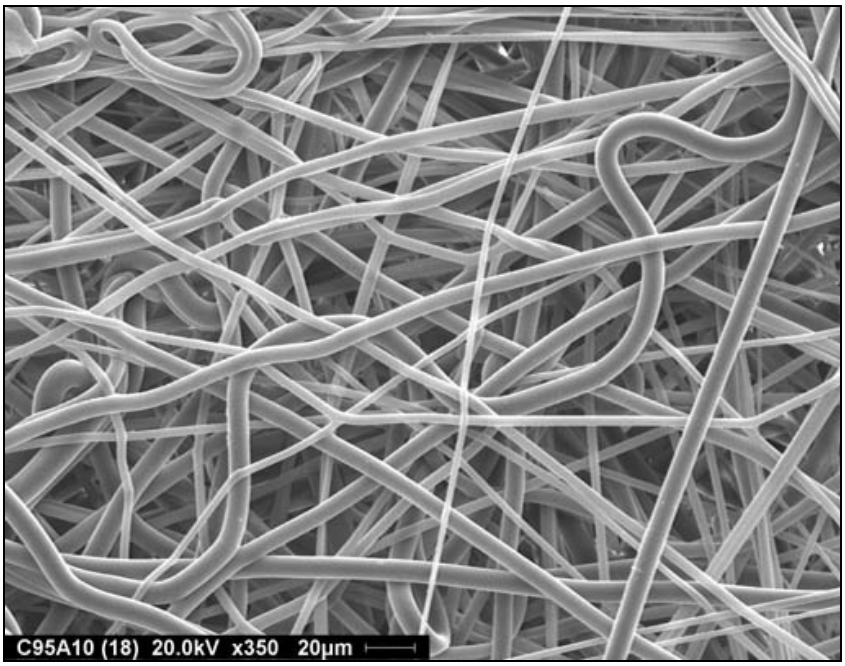

Figure 47: 350X SEM image of S95 melt-blown web at DCD=30.5cm. Courtesy of BASF

Regardless of the DCD, the most probable fiber diameters appear to be in the vicinity of 8 microns for ester TPU, 5 microns for ether TPU and 16 microns for PEBA series. The fiber diameters of the melt-blown webs produced from PEBA series are larger than those of ester and ether TPU since PEBA melt-blown webs were produced at considerably lower air flow rates, as seen in Table 10. Lower air flow rates produce lower air velocities, and the difference between air and fiber velocities is less, thereby leading to less air drag forces or stress on the polymer melt. These low stresses result in less attenuation and larger fiber diameters.

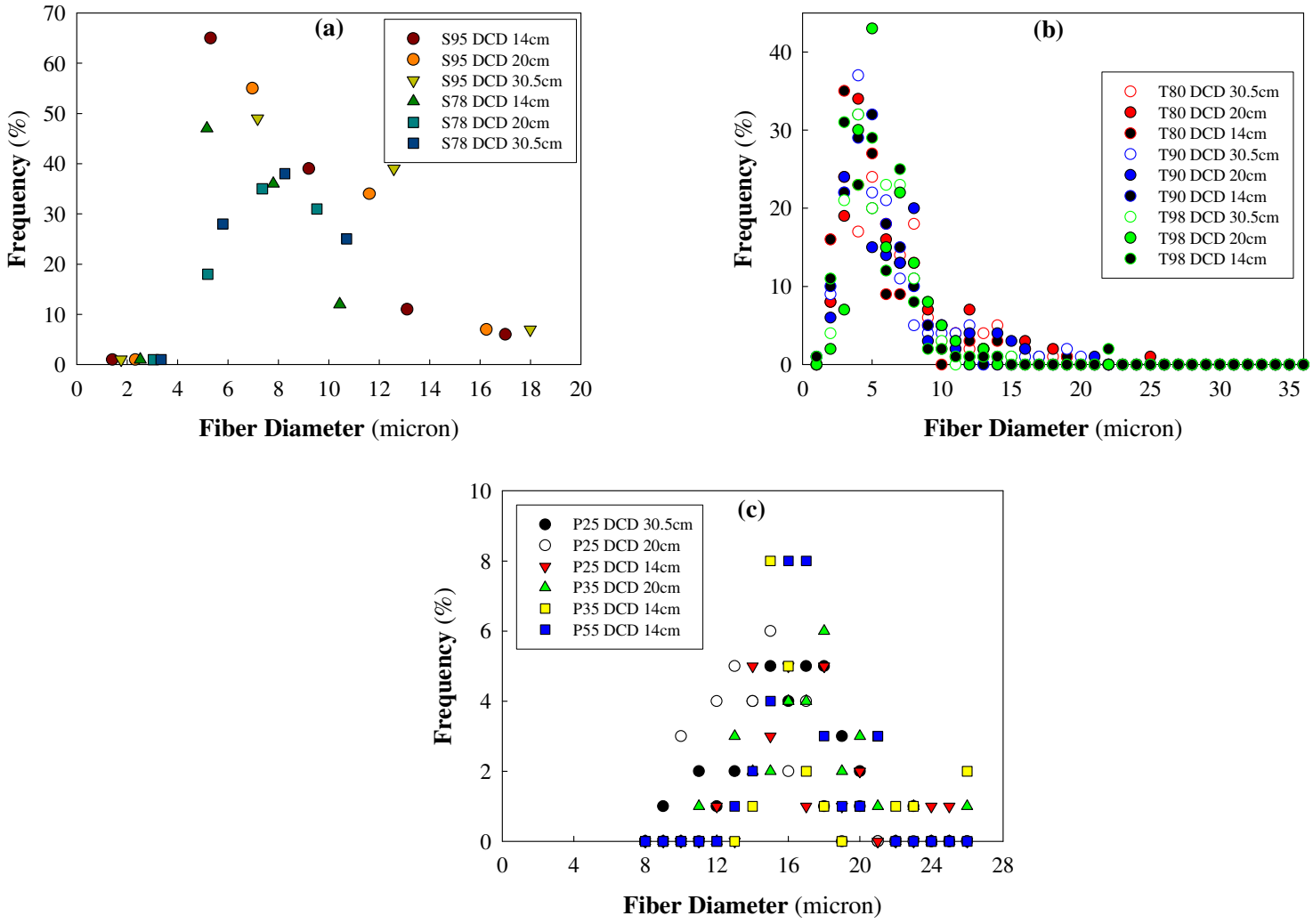

Figure 48: Fiber Diameter Distributions of **(a)** Ester TPU, **(b)** Ether TPU and **(c)** PEBA

At this point, following assumptions are made: (1) Fibers spend most of their time near the centerline position ($x=y=0$) and travel only in the z-direction i.e. do not vibrate. (2) The polymer density does not change as a function of temperature and crystallinity. (3) Fibers are circular in cross-section. (4) The polymer melt exiting melt-blowing die does not exhibit die-swell. (5) The polymer melt does not break by the large drag forces due to very high air velocities until reaching the collector i.e. a continuous fiber is produced. With these assumptions, at any position below the die, fiber velocity as a function of fiber diameter is calculated from the mass conversation (continuity) for steady-state conditions as follows:

$$Q = A_n(z)V_n(z) = A_f(z)V_f(z)$$

$$V_f(z) = \frac{4Q}{\pi d_f^2(z)} \quad \text{.....} \quad (14)$$

Where Q (m^3/s) is the polymer volumetric flow rate exiting the nozzle and is constant at any point along the fiber between the die and collector, A_n (m^2) and A_f (m^2) cross-sectional area of polymer melt at nozzle exit and final fiber, respectively, V_n (m/s) axial polymer velocity at the die exit and V_f (m/s) axial fiber velocity to achieve final fiber diameter. **[86]** The calculated fiber velocity values to achieve the final fiber diameters are shown in Table 10. Comparison of maximum air velocity values to those of fiber for ether TPU in Table 10, predictions of fiber velocities are much higher than the maximum air velocities. This can be explained as follows: Ether TPU series was processed with the highest air flow rates producing highest air velocities impinging on the polymer melt. This air velocity falls in the range of melt-blowing, where the fibers will travel parallel to the axial air flow only at very close distances to the die.

Beyond this, due to high air turbulence they will move in transverse positions leading to fiber entanglements, which were suggested to further elongate the fiber diameters. **[93]** Also unlike PEBA series, both ether and ester TPU series were processed with cross quench air flow in addition to the processing hot air flow, which is not represented in this geometry. Therefore, for ether TPU series, we suggest that higher fiber velocities calculated to reach the final fiber diameters reflects combined effect of large air drag forces and fiber entanglements on fiber attenuation. Therefore, in fiber modeling, PEBA series was studied only to predict fiber diameter and temperature profiles.

The rheological and thermal properties of the polymers used are given in Tables 11 and 12, respectively. Fluent Fiber Model treats the polymer melt as a Newtonian fluid until the temperature of the polymer melt falls below the solidification temperature. Newtonian approximation was demonstrated to adequately describe the polymer rheological forces in melt-blowing since large temperature gradients affect the polymer viscosity more strongly than the elongation rates. **[1, 48]** Agreeing, the model estimates the melt zero shear viscosity as a polymer property and considers being a function of temperature only as follows:

$$\eta_0 = A \exp\left(\frac{B}{C + T_f}\right) \quad \text{.....} \quad (15)$$

where T_f is the polymer temperature in Kelvin (K), η_0 is the polymer zero shear viscosity at T_f in Pa.s.. When T_f is measured in K, C=0. **[48, 85, 94]** The elongational viscosity is approximately three times the melt zero shear viscosity, 3η. The zero shear rate viscosities of the polymers, η_0 for different range of temperatures were provided by BASF and Arkema.

The values of the input parameters A and B shown in Table 11 were found by plotting ln η_0 against $1/T_f$, where A is the anti-log of the y-intercept, and B is the slope of the linear fit. The plots of $ln\ \eta_0$ against $1/T_f$ are shown in Figure 49.

Table 11: Rheological properties of the polymers used in the simulation

Polymer		**A** (kg/m.s)	**B** (K)	**Solid state viscosity** (kg/m.s)	**Zero shear viscosity** (kg/m.s)	**Polymer Blending Interval**
Ether Elastollan® TPU	T80	3.1e-16	20,488	10^8	117.11	84
	T90	2.9e-14	18,273	10^8	40.90	70
Ester Elastollan® TPU	S78	1.6e-27	33,491	10^8	18.53	96
	S95	4.2e-42	50,535	10^8	7.52	92
PEBA (Pebax®)	P25	2.6e-03	5,843.7	10^8	88.99	61
	P55	2.1e-04	7,677.5	10^8	104.36	38

Table 12: Thermal properties of the polymers used in the simulation

Polymer		**T_m** (C)	**T_{solid}** (C)	**Specific Heat** (J/kg-deg)	**Thermal Conductivity** (W/m-K)	**Density** (kg/m^3)
Ether Elastollan® TPU	T80	233	63	1,700	0.190	1110
	T90	251	95	2,000	0.220	1130
Ester Elastollan® TPU	S78	253	62	1,700	0.190	1180
	S95	262	104	2,300	0.250	1210
PEBA (Pebax®)	P25	287	74	2,660	0.175	909.8
	P55	312	123	3,280	0.290	905.6

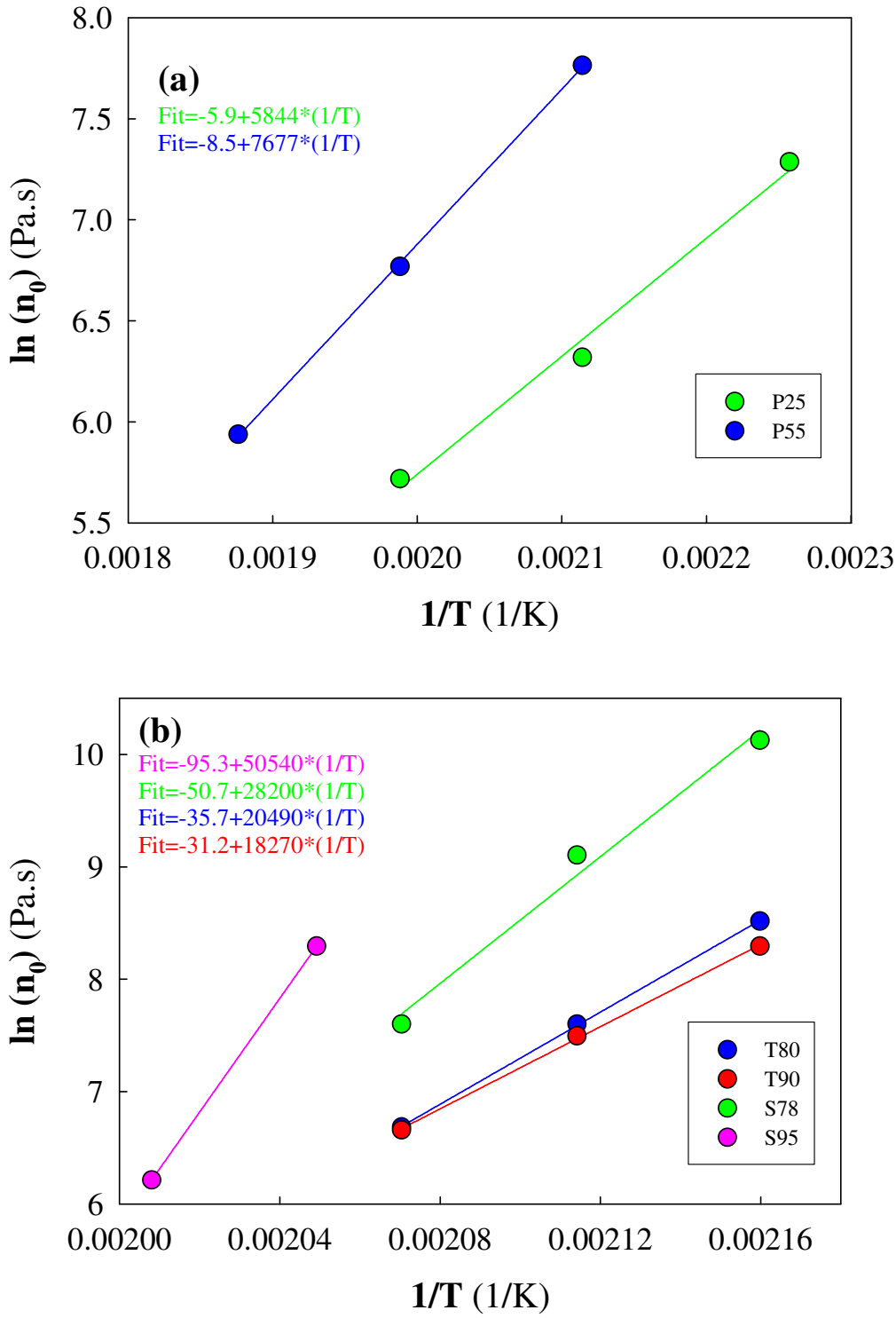

Figure 49: $\ln(\eta_0)$ vs. *1/T* for **(a)** PEBA and **(b)** Ether and Ester TPU

T_{solid} in Table 12 is the temperature where the DSC polymer crystallization is complete on cooling from the melting temperature at a rate of 20°C/min. In modeling the polymer flow, it was assumed that DSC quiescent crystallization kinetics data is adequate in describing the fiber solidification behavior in melt-blowing, i.e. stress-induced crystallization effects on crystallization kinetics are negligible. Because fibers within melt-blown web structures are highly entangled and fused at contact points rather than being individual fibers, AATCC 135/150 (120F wash, dry 160F) was used to measure fiber orientation. All melt-blown web samples exhibited very low web shrinkage results of around 0–1%, indicating lack of molecular orientation within fibers. This means in melt-blowing, polymer crystallization should be temperature driven but not by molecular orientation. I.e. development of crystallization depends on rate of crystallization, how quickly polymer melt reaches crystallization temperatures, and how much time it spends in the crystallization zone before being deposited on the collector. This can be explained as follows: Upon exiting the die, the low viscosity polymer melt is stretched significantly at distances very close to die due to large air drag force. This significant and rapid attenuation will develop molecular orientation along the fiber axis. Polymer melt stretching and orientation continue until reaching distances beyond which fiber attenuation ceases and both fiber diameter and velocity profiles reach their final values. Thereafter, both remain constant with further distances as the deformation becomes negligible. If polymer material is cooled rapidly and reaches solidification temperatures while molecules are in their oriented state, molecular orientation will be maintained. However, in melt-blowing the polymer melt does not cool rapidly to temperatures low enough to freeze the molecular orientation.

This is mainly because melt-blowing is a process designed to produce micro-fibers, which requires significant polymer melt attenuation. In order to achieve fiber stretching temperatures of the air impinging on polymer melt are typically similar to polymer melt temperatures exiting the die, and maintained high enough to yield low polymer melt viscosity for sufficiently long distances toward the die. Thus, as the polymer melt travels below the die toward the position of final diameter; it does not reach the solidification temperatures rapidly enough to avoid relaxation of the molecules to their original states at the die exit. The orientation introduced during the stretching zone is not frozen into the fiber; rather the fiber solidifies with unoriented molecules. I.e. polymer crystallization in melt-blowing is dominated by cooling and orientation effects are negligible. Thus, the stress acting on the fiber does not enhance crystallization kinetics and our assumption that DSC quiescent crystallization data can be used to model fiber formation is adequate. This is particularly true for PEBA, which were melt-blown at relatively low speeds where the crystallization kinetics was shown to depend on temperature but not orientation effects. **[95]** Fluent Fiber Model predicts tensile or rheological forces that drive fiber formation to be applied at the take-up point. As seen in Figure 48, for a given polymer type, fiber diameters have very similar values for different DCDs used to collect melt-blown fibers. This means that DCDs less than 14cm, 20cm, and 30cm should be designated as the take-up point to predict fiber diameter and temperature profiles. This is illustrated in Figure 50, where fiber diameter profiles ester TPU and PEBA series are predicted at various DCDs as the take-up point. As expected from Figures 43-46, most of the fiber deformation is limited to the region of significant air velocity drop, $0< z<5$ *cm,* where polymer melt exiting the die meets with very high air velocity.

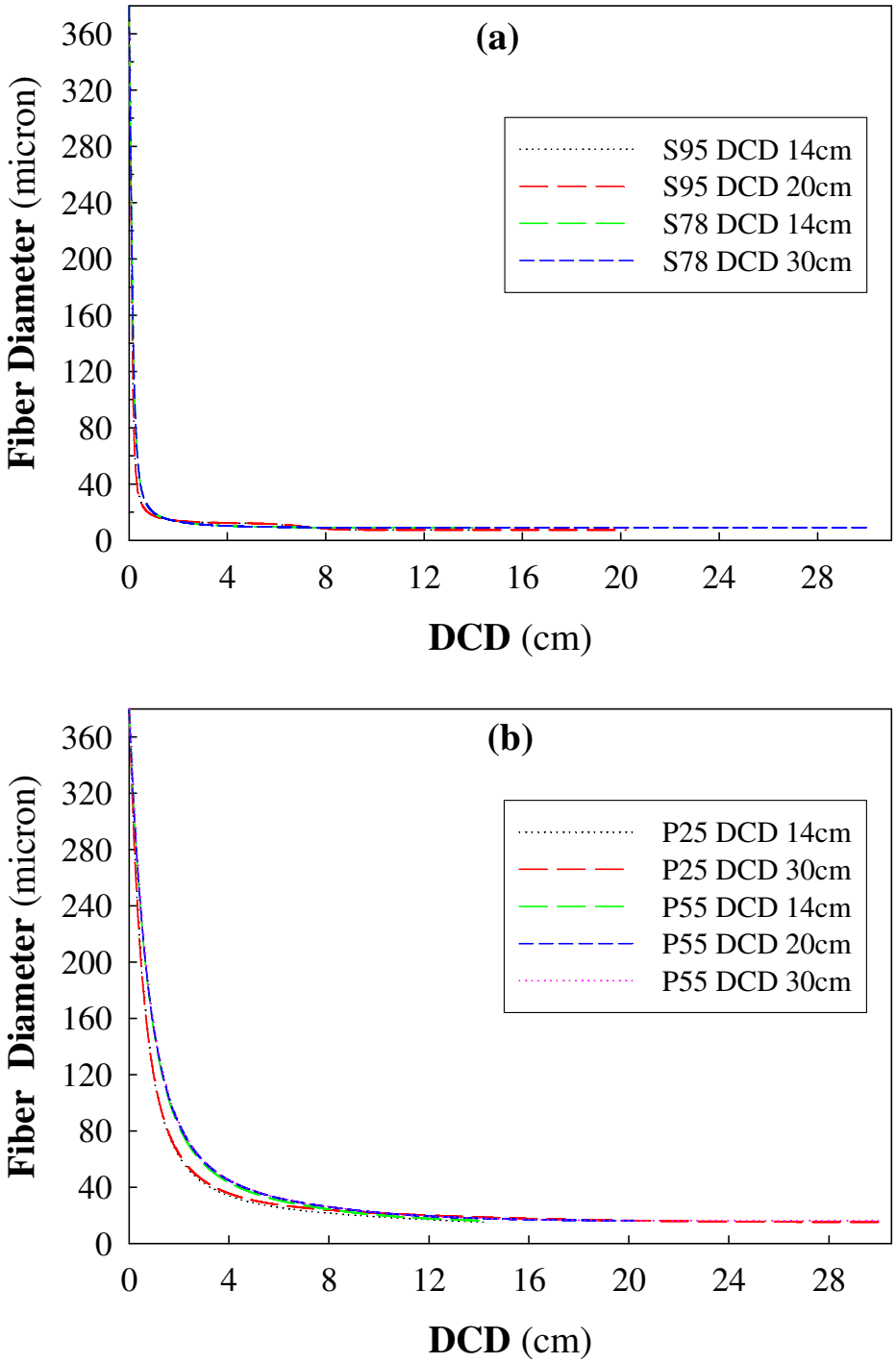

Figure 50: Simulated fiber diameter profiles for **(a)** S78 and S95 with a mass flow rate of 8.33e-06kg/s, **(b)** P25 and P55 with a mass flow rate of 4e-06kg/s

Beyond this region, the profile reaches a plateau of almost final fiber diameter values with further increasing DCDs. Figure 50 also shows that ester TPU series is stretched to finer diameters at relatively shorter distances than PEBA series even though the polymer mass flow rate for ester TPU series was more than twice. This is due to significantly higher air velocities of ester TPU series as seen in Table 10 but also the additional effect of the quench air, which was turned off in melt-blowing PEBA series.

However, in melt-blowing the air impinges on polymer melt upon exiting the die, thereby stretching the polymer melt to final fiber diameters at much closer distances than DCDs studied. Thus, for an improved prediction of fiber diameter profiles, the so-called stop point suggested by the literature was used as the take-up position. The stop point corresponds to the distance below the die where fiber velocity from continuity in Eqn. 14 approaches to air velocity. **[1, 79, 80]** Beyond this point fiber diameter and velocity profiles remain essentially unchanged at final values until reaching the collector. Because additional quench air was turned off in melt-blowing PEBA series, we can suggest that the fiber velocities from Eqn. 14 to predict measured fiber diameters can be accurately used to estimate the stop distance. For ester TPU series, the effect of additional quench air was ignored.

Figure 51 shows comparison of fiber diameter profiles predicted from the simulations when DCD=14cm and stop point are used as take-up coordinates. For hard grades i.e. P55 and S95, fiber velocities shown in Table 10 correspond to stop point of ~5cm and for soft grades i.e. P25 and S95 to ~1.36cm. At the stop point, fiber diameter reaches 11.2microns for ester TPU series, 15.4 microns for P25 and 16.5microns for P55.

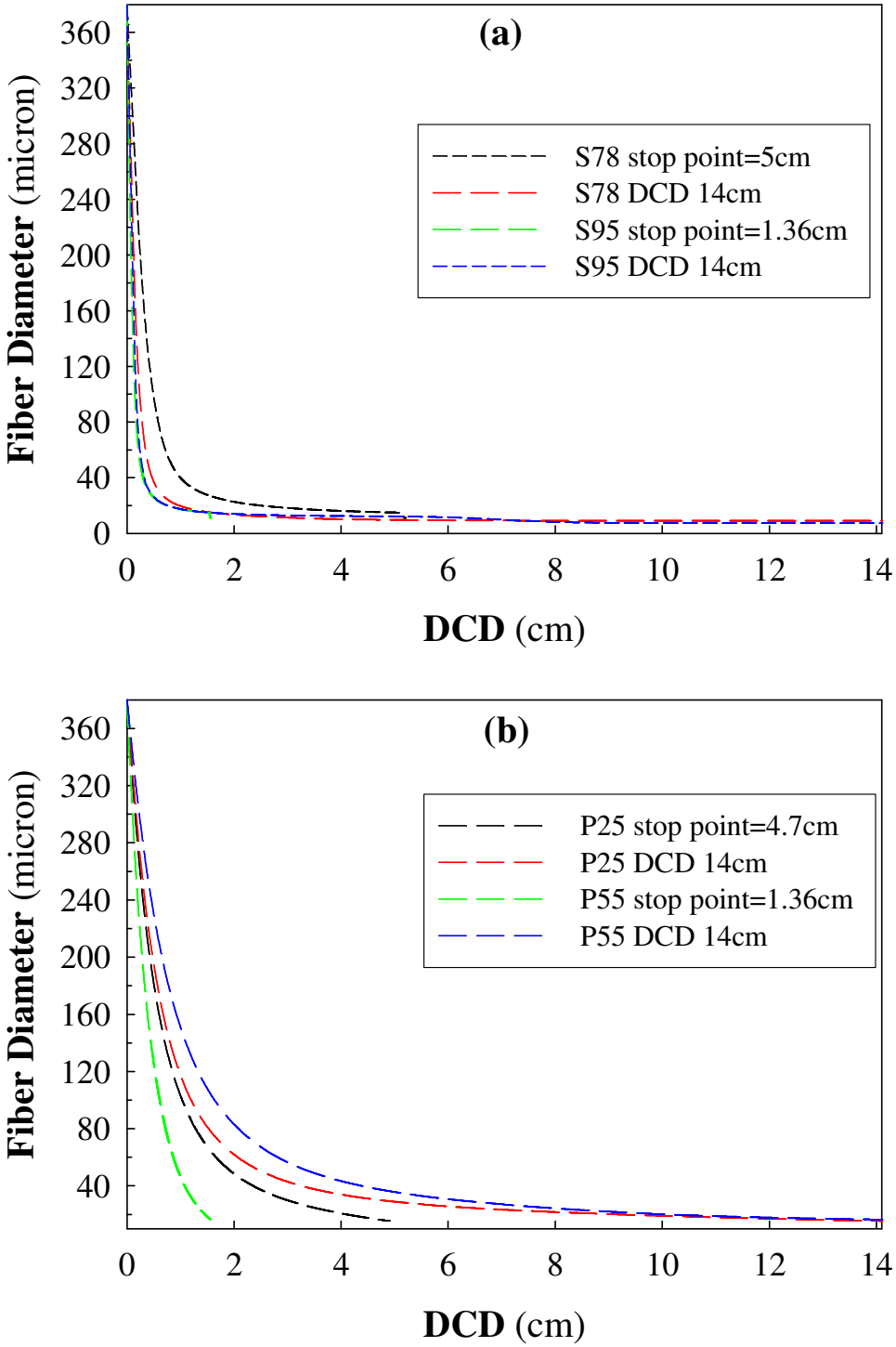

Figure 51: Fiber diameter profiles for **(a)** S78 and S95 with a mass flow rate of 8.33e-06kg/s and **(b)** P25 and P55 with a mass flow rate of 4e-06kg/s

This means at the designated stop distances below the die both P25 and P55 complete attenuation to final fiber diameter values measured at DCD=14cm. S78 and S95, on the other hand, was stretched to around %77 and %52 of their final diameter, respectively. Further fiber stretching beyond the stop point can be attributed to the presence of the quench air in ester TPU series. However, in this significant fiber diameter reduction region, air velocity dropped %72 for S78, %38 for S95, %67 for P25 and %45 for P55, meaning fiber attenuation should still continue after the stop point. In contrast, beyond this point fiber attenuation ceases as both fiber diameter and velocity reach final values, and their profiles become relatively flat, in particular for PEBA series. This is mainly because the air drag force responsible for fiber diameter reduction becomes negligible since constant fiber velocity will be higher than the air velocity at the same z position. Unlike melt-spinning process where polymer melt is typically injected into ambient or cool air, in melt-blowing polymer temperatures do not reach solidification temperatures at positions where fiber attenuation ceases. Thus, fiber diameter plateau observed in Figure 49 does not correspond to crystallization as suggested in melt-spinning and polymer fiber is still a flowing fluid. **[87, 88, 95, 96]** The model cannot predict fiber temperature profiles beyond the stop point. Therefore, to explore the distances where polymer melt solidifies, fiber temperature profiles need to be estimated by using studied DCDs as the stop point. This assumption will, however, over predict the fiber temperature profiles since fiber diameters will be much larger as seen in Figure 51, thereby reducing the heat transfer from the hot polymer melt to the surrounding air.

Fluent fiber model predicts fiber temperature profiles from the following energy conservation and heat transfer correlations that describe the convective heat transfer from polymer fiber surface to surrounding parallel air flow **[89, 90]**

$$\rho_{fiber} C_{p,fiber} V_{fiber}(z) \frac{dT_{fiber}(z)}{dz} = -\frac{4h(z)}{d_{fiber}(z)} \left(T_{fiber}(z) - T_{air}(z)\right)$$

$$Nu_z = \frac{h(z) d_{fiber}(z)}{k_{air}} = 0.42 \left(\mathrm{Re}_{rel}\right)^{0.334} \quad \text{.....Eqn. (15)}$$

Where ρ_{fiber} is fiber density (kg/m^3), d_{fiber} fiber diameter (m), $c_{p,fiber}$ specific heat of polymer fiber (J/kg.K), V_{fiber} fiber velocity (m/s), $dT_{fiber}(z)/dz$ axial gradient of the fiber temperature, T_{fiber} fiber temperature (K), T_{air} air temperature (K), h coefficient of convective heat transfer at the polymer fiber surface (W/m^2.K.s), k_{air} air thermal conductivity (W/m.K) and Re_{rel} is relative Reynolds number as defined in Eqn. 12. Here, fiber temperature is assumed to be uniform across the cross-section, axial heat conduction is ignored; radiation and free convection are negligible as well as viscous heating. Eqn (15) is the relation expressing forced-convection transfer suggested by Kase and Matsuo. **[89, 90]** In predicting fiber temperature profiles constant values of ρ_{fiber} and $c_{p,fiber}$ are assumed as shown in Table 12. Fiber temperature profiles of ester TPU and PEBA from Fluent Fiber model, which uses the heat transfer correlation of default values in Eqn. 15 are shown in Figure 52. The release of heat of crystallization when the polymer solidifies is not included in these correlations. This effect typically causes fiber temperature profile to plateau. **[87, 95]** Thus, we would not expect to observe the plateau at fiber solidification point.

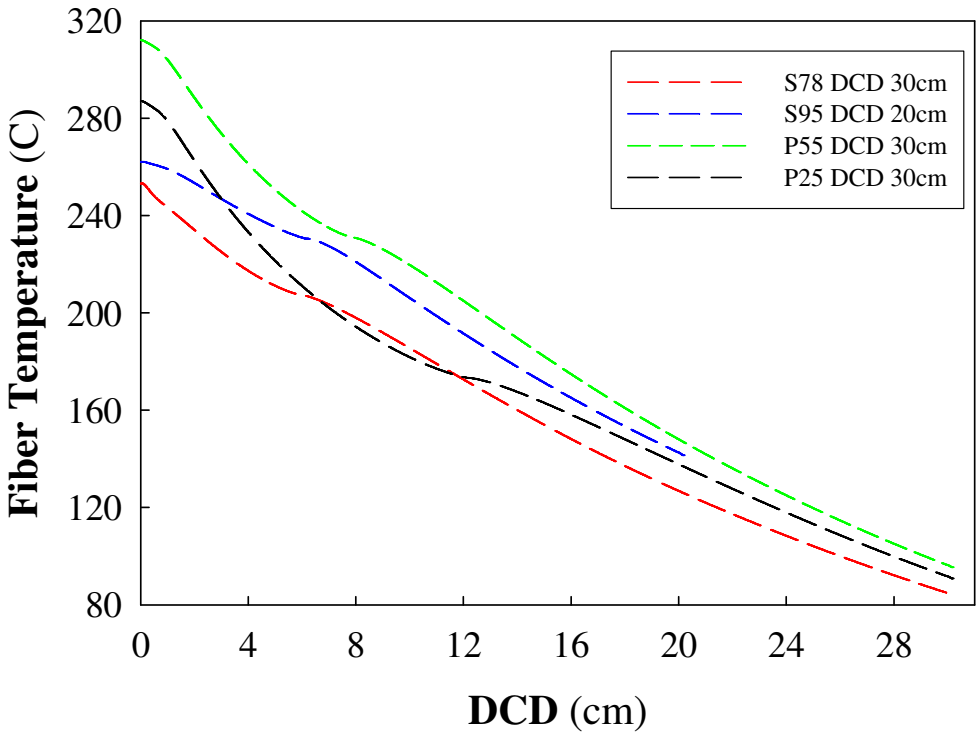

Figure 52: Fiber temperature profiles of ester TPU and PEBA series

As seen in Figure 52, fiber temperature profiles do not reach the solidification temperatures at distances hypothesized in Figure 36, where DSC crystallization kinetics data was mapped onto measured air temperature profiles. In agreement with Shambaugh's experimental and simulation results for PP fiber, fiber model under predicts fiber temperatures in melt-blowing. This is mainly because fiber model uses the heat-transfer correlation in Eqn. 15, which was originally developed for a stationary hot wire in parallel air flow rather than moving polymer. **[86, 89, 90]** It also neglects the effect of crystallization questioning its applicability to fast crystallizing hard polymer grades like S95 and P55.

Bansal and Shambaugh **[43]** observed that experimental fiber temperature profiles do not reach lower temperatures as quickly as that of the simulated air profile since ambient air entrainment causes more rapid drop of the air temperature. They also demonstrated that the heat-transfer coefficient in Kase-Matsuo's heat transfer correlation in Eqn. (15) was inadequate in modeling fiber temperature profiles in melt-blowing. Based on experimental measurements of fiber temperatures, they modified the constant value 0.42 in Eqn. (15) to a value of 4.14 and improved fiber temperature profiles. Because fiber model uses default value of 0.42, we cannot further improve our fiber temperature predictions illustrated in Figure 52 by calibrating this constant.

Even though the fiber simulations do not provide quantitative agreement with the web tensile properties explained in terms of crystallization kinetics, Figure 52 demonstrates qualitative agreement. The softer grades i.e. S78 and P25 have significantly lower crystallization rates than S95 and P55 and require much larger cooling for crystallization to occur. Thus, the polymer solidification for softer grades is delayed to much further distances below the die than those of harder grades.

V. CONCLUSIONS

Melt-blown webs were produced from elastomeric copolymers: (1) BASF Elastollan® Ether TPU series (Shore A): 1180A10, 1190A16, and WY5352D-1; (2) BASF Elastollan® Ester TPU series (Shore A): C78A15, and C95A10; and (3) Arkema Pebax® series (Shore D): 2533, 3533, 5533. The isothermal crystallization kinetics of these melt-blown webs were analyzed through differential scanning calorimetry (DSC) by two different models:

(1) the Avrami analysis, which requires transformation of the DSC data from differential to integral form making this traditional method very sensitive to errors, and (2) a model proposed by Kurajica et al., which is the derivative of the Avrami equation and could be fitted directly to the untransformed DSC data. The crystallization kinetics parameters: Avrami *n* and crystallization rate, *k* derived from both models were comparable and exhibited similar crystallization temperature, polymer type and hardness dependence. Since the Kurajica model could be directly fitted to the DSC heat flow data, the possible errors involved in the Avrami model were reduced, thereby improving the accuracy of the derived kinetic parameters. The values of the Avrami exponent, *n* range between 2.59 and 3.41, suggesting all webs produced from these polymer types have similar nucleation and growth mechanisms, even under different melting and crystallization conditions. These *n* values of around 3 along with morphological observations indicate that the crystallization mechanism is similar to that of homopolymers involving formation of macroscopic three dimensional crystal structures that nucleate and grow with instantaneous nucleation under isothermal conditions. The crystallization rates of all polymer types and hardness grades decreased with increasing crystallization temperatures for lower degree of cooling and concentration of non-crystallizable soft segment. The extent of cooling required to achieve a given crystallization rate followed the order of P55 < P35 < P25 for PEBA series, T98 < T90 < T80 for ether TPU series and S95 < S78 for ester TPU series. While among all polymers, P55, the hardest grade of PEBA series, crystallized the fastest at a given extent of cooling, the crystallization rates and half-times of the soft hardness grades for all polymer types i.e. P25, T80 and S78 were comparable within similar isothermal crystallization temperature ranges.

This means that for a given elastomeric copolymer, the overall crystallization rate is dependent on the relative concentration of the hard and soft segments under similar cooling conditions.

Process air velocities and temperatures were measured for various distances below the die. The air flow field was also modeled by using Fluent software for melt-blowing process conditions of all the studied polymers. The air flow field predicted from simulations showed good agreement with the experimental profiles and enabled modeling of fiber formation in melt-blowing. It was found that the air velocity drops rapidly as the distance from the melt-blowing die increases until approximately 5-6 cm below the die. After that, the velocity approaches a constant value. The process air temperature follows a similar profile where the temperature drops rapidly for the first 5-6 cm below the die and then varies only slowly thereafter.

Tensile properties of these webs produced at various die-to-collector distances, DCDs were measured and explained in terms of the crystallization kinetics along with the temperature profile of the process air. By mapping the crystallization behavior onto air temperature profile, the polymer crystallization kinetics was observed to have a profound effect on the web strength. Due to its significantly higher crystallization rate, P55 was found to crystallize prior to reaching the forming belt, resulting in a weak web. On the other hand, softer grades: P25, S78, and T80 begin to crystallize just before reaching the forming belt and continue to crystallize on the belt. This provides good inter-fiber adhesions since fibers are still tacky and results in a strong web. On increasing DCD, the fibers have traveled longer distances and crystallized more before reaching the forming belt.

The fibers thus have lower temperatures before they contact with others already on the collector, thereby reducing inter-fiber adhesion and the web strength. Therefore, it is concluded that the web strength is a strong function of the degree of fiber solidification achieved within the web. This is determined by the crystallization kinetics of the polymers, the polymer extrusion and air temperatures and the amount of time it takes the polymer melt to reach the collector, which depends on the air velocities and distances traveled between the die and collector (DCD).

VI. RECOMMENDATIONS

In this work, it was demonstrated that the properties of melt-blown webs produced from elastomeric copolymers can be predicted from constituent polymer material properties and processing conditions. This provides a fundamental understanding of the interaction between polymer material, melt-blowing process and web properties in melt-blowing elastomeric copolymers. It was shown that the following protocol can be used to estimate melt-blown web tensile properties for elastomeric copolymers or semi crystalline polymers by (1) analyzing polymer crystallization kinetics through a simple method: differential scanning calorimetry (DSC), (2) modeling air flow field of melt-blowing equipment with simulation tools, and (3) correlating polymer crystallization behavior to melt-blowing air flow field characteristics and distances between the die and collector. This suggested protocol not only eliminates the need to run numerous expensive trials on melt-blowing equipment but also allows modification of polymer material properties to achieve desired web attributes. The flexibility of calibrating the polymer material and melt-blowing process conditions by the

suggested protocol presents a relatively simple and cost effective technique to predict melt-blown web tensile properties of elastomeric copolymers and semi crystalline polymers.

The fiber formation in melt-blowing was analyzed only between the die and the collector. I.e. the effect of the history of the polymer flow prior to exiting the die was ignored. The contribution of the rheological properties of polymer materials on the fiber formation and the dependence of polymer flow on the nozzle configuration needs to be explored.

The importance of the fiber solidification mechanism on fiber formation in melt-blowing was demonstrated. DSC isothermal crystallization kinetics was used in explaining polymer solidification behavior along its path until reaching the collector. However, polymer crystallization does not take place at a fixed temperature but rather a temperature range. In addition, melt-blowing involves large fiber temperature gradients and the cooling rate used in DSC analysis was significantly slower than those encountered in melt-blowing. Therefore, non-isothermal crystallization behavior of polymer materials needs to be analyzed to improve the prediction of fiber solidification behavior.

Finally, computational modeling of the homocomponent fiber spinning could not predict the fiber solidification temperatures within studied DCD ranges. The available fiber model simulation tool allows using only the default values for heat transfer correlations originally developed for a stationary hot wire in parallel air flow rather than moving polymer. And, it does not include the effects of polymer crystallization. Thus, the modeling efforts need to expanded to better simulate the fiber formation in melt-blowing. Or, fiber diameter or velocity profiles need to be measured online to input in analytical analysis of fiber temperature profiles.

In addition, melt-blowing involves extrusion of the polymer melt from a number of nozzles typically arranged in a row. This requires extension of the fiber modeling to multi fiber configuration to study the interaction between the adjacent fibers, which will likely delay fiber crystallization to longer distances than that of a single fiber and process air.

VII. REFERENCES

[1] Shambaugh, R., Uyttendaele, M.; Melt Blowing: General Equation Development and Experimental Verification; AIChE Journal Vol. 36 (2) (1990)

[2] USP 2003/0171052 A1; Stretchable Nonwoven Web and Method Therefore; E I Du Pont De Nemours and Company (2003)

[3] USP 6,225,243; Elastic Nonwoven Fabric Prepared From Bi-Component Filaments; BBA Nonwovens Inc. (May 2001)

[4] USP 4,923,742; Elastomeric Polyether Block Amide Nonwoven Web; Kimberly-Clark Corporation (1990)

[5] USP 4,741,949; Elastic Polyetherester Nonwoven Web; Kimberly-Clark Corporation (1988)

[6] USP 4,775,579; Hydroentangled Elastic and Nonelastic Filaments (1988)

[7] USP 4,663,221; Fabric Comprising Composite Sheath-Core Fibers, Fabric Comprising Bicomponent Fiber Bundles And Process For Its Preparation; Kuraray Co., Ltd. (1987)

[8] Legge, N.R., Holden, G., Schroeder, H.E.; Thermoplastic Elastomers A Comprehensive Review; Hanser Publishers New York (1987)

[9] BASF literature, www.basf.com, July 2005

[10 Shiomi, T. Takeshita, H., Kawaguchi, H., Nagai, M., Takenaka, K., Miya, M.; Crystallization and Structure Formation of Block Copolymers Containing a Rubbery Amorphous Component; Macromolecules Vol. 35 8056-8065 (2002)

[11] Mandelkern, L.; Crystallization of Polymers. New York McGraw Hill (1964)

[12] Rangarajan, P., Register, R.A.; Morphology of Semicrystalline Block Copolymers of Ethylene-(Ethylene-alt-propylene); Macromolecules Vol. 26 4640-4645 (1993)

[13] Alberola, N.; Micromechanical Properties of Polyether Block Amide Copolymers; Journal of Applied Polymer science Vol. 36 (4) 787-804 (1988)

[14] Xu, M., Liu, W.G., Wang, C. L., Gao, Z. X., Yao, K.D.; Surface Crystalline Characteristics of Polyurethane Investigated by Atomic Force Microscopy; Journal of Applied Polymer Science Vol. 61 (12) 2225-2228 (1996)

[15] McLean, R.S., Sauer, B.B.; Tapping-Mode AFM Studies Using Phase Detection for Resolution of Nanophases in Segmented Polyurethanes and Other Block Copolymers; Macromolecules Vol. 30(26) 8314-8317 (1997)

[16] Kurajica, S., Schmauch, J., Tkalcec, E.; Application of a Numerical Method for the Analysis of Metglas 2826 MB Crystallization Kinetics; Croatica Chemica Acta Ccacaa Vol. 75 (3) 693-699 (2002)

[17] Lie-Zen, C., De-Lun, K., Andrew, T., Hong-Bing, T.; Block Copolyetheramides. II. Synthesis and Morphology on Nylon-6 Based Block Copolyetheramides; Journal of Polymer Science: Part A: Polymer Chemistry Vol. 30 951-953 (1992)

[18] Konyukhava. E.V., Buzin, A.I., Godovsky, Y.K.; Melting of Polyether-Block-Amide (Pebax): The Effect of Stretching; Thermochimica Acta Vol. 391 (1-2) 271-277 (2002)

[19] Jignesh,P. S., Jiannong, X., Garth, L. W.; Solid State Structure-Property Behavior of Semicrystalline Poly (Ether-Block-Amide) PEBAX Thermoplastic Elastomers; Polymer Vol. 44 743-756 (2003)

[20] Nojima, S., Kato, K., Yamamoto, S., Ashida, T.; Crystallization of Block Copolymers. 1. Small-Angle X-Ray Scattering Study of an E-Caprolactone-Butadiene Diblock Copolymer; Macromolecules Vol. 25 2237-2242 (1992)

[21] Rangarajan, P., Register, R.A., Adamson, D.H., Fetters, L.J., Bras, W., Naylor, S., Ryan, A.J.; Dynamics of Structure Formation in Crystallizable Block Copolymers; Macromolecules; Vol. 28 1422-1428 (1995)

[22] Nojima, S., Nakano, H., Ashida, T.; Crystallization Behavior of a Microphase Separated Diblock Copolymer; Polymer Vol. 34 (19) 4168-4170 (1993)

[23] Nojima, S. , Nakano, H., Takahashi, Y., Ashida, T.; Crystallization of Block Copolymers: 3. Crystallization Behavior of an e-Caprolactone-Butadiene Diblock Copolymer; Polymer Vol. 35 (16) 3479-3486 (1994)

[24] Loo, Y., Register, R.A.; Polymer Crystallization in 25-nm Spheres; Physical Review Letters Vol. 84 (18) 4120-4123 (2000)

[25] Chen, H., Wu, J., Lin, T., Lin, J..; Crystallization Kinetics in Microphase-Separated Poly (etyhleneoxide)-block-poly (1, 4-butadiene); Macromolecules Vol. 34 6936-6944 (2001)

[26] Loo, Y. et al., Register, R.A.; Polymer Crystallization Confined in One, Two, or Three Dimensions; Macromolecules Vol. 34 8968-8977 (2001)

[27] Chen, H., Hsiao, S., Lin, T., Yamauchi, K., Hasegawa, H., Hashimoto, T.; Microdomain-Tailored Crystallization Kinetics of Block Copolymers; Macromolecules Vol. 34 (4) 671-674 (2001)

[28] Loo, Y. et al., Register, R.A.; Modes of Crystallization in Block Copolymer Microdomains: Breakout, Templated, and Confined; Macromolecules Vol. 35 1365-2374 (2002)

[29] Wegner, G., Zhu, L., Lieser, G., Tu, H.; A New Staining Technique for Electron Microscopy of Poly (ester) s and Segmented Copolymers with Ester Linkages; Makromol. Chem. Vol. 182 231-235 (1981)

[30] Zhu, L., Wegner, G.; The Morphology of Semicrystalline Segmented Poly (ether ester) Thermoplastic Elastomers; Makromol. Chem. Vol. 182 3625-3638 (1981)

[31] Zhu, L., Wegner, G.; The Crystallization Behavior and the Mechanical Properties of Segmented Poly (ether ester) Thermoplastic Elastomers; Makromol. Chem. Vol. 182 3639-3651 (1981)

[32] Ho, R., Hseih, P., Yang, C., Lin, J.; Crystallization Kinetics for Low-Ether-Content Polyether-Polyester Block Copolymers with Amide Linkages; Journal of Polymer Science: Part B: Polymer Physics Vol. 39 (20) 2469-2480 (2001)

[33] Seymour, R.W., Overton, J.R., Corley, L.S.; Morphological Characterization of Polyester-Based Elastoplastics; Macromolecules Vol. 8 (3) 331-335 (1975)

[34] Boublil, H., Okoroafor, E., Belhoucine, M., Rault, M., Atochem, M.G.; Morphology of Polyamide and Polyether Block Amide Blends; Polymer Engineering and Science Vol. 29 (10) 679-684 (1989)

[35] Supaphol, P., Spruiell, J.E.; Isothermal Melt- and Cold-Crystallization Kinetics and Subsequent Melting Behavior in Syndiotactic Polypropylene: A Differential Scanning Calorimetry Study; Polymer Vol. 42 (2) 699–712 (2001)

[36] Zhang, Q., Yu, M., Fu, Q.; Crystal Morphology and Crystallization Kinetics of Polyamide-11/clay Nanocomposites; Polymer International Vol. 53 (12) 1941-1949 (2004)

[37] Mezghani, K.; Crystallization Kinetics of Polymers; Chapter 3; Physical Properties of Polymers Handbook, AIP Press New York (1996)

[38] Sharples, A.; Polymer Crystallization; London, Edward Arnold (Publishers) Ltd. (1966)

[39] Wente, W.; Superfine Thermoplastic Fibers; Industrial and Engineering Chemistry Vol. 48 No. 8 (1956)

[40] Wadsworth, L., Lee, Y.; Effects of Melt-blowing Process Conditions on Morphological and Mechanical Properties of Polypropylene Webs; Polymer Vol. 33 (6) (1992)

[41] Harpham, A.S., Shambaugh, R.L.; Flow Field of Practical Dual Rectangular Jets; Industrial and Engineering Chemistry Research Vol. 35 3776-3781 (1996)

[42] Harpham, A.S., Shambaugh, R.L.; Velocity and Temperature Fields of Dual Rectangular Jets; Industrial and Engineering Chemistry Research Vol. 36 3937-3943

(1997)

[43] Bansal, V., Shambaugh, R.; On-line Determination of Diameter and Temperature During Melt Blowing of Polypropylene; Industrial and Engineering Chemistry Research Vol. 37 (5) (1998)

[44] Tate, B., Shambaugh, R.; Modified Dual Rectangular Jets for Fiber Production; Industrial and Engineering Chemistry Research Vol. 37 No. 9 (1998)

[45] Krutka, H., Shambaugh, R., Papavassiliou, D.; Analysis of a Melt-Blowing Die: Correlations of CFD and Experiments; Industrial and Engineering Chemistry Research Vol. 41 (20) (2002)

[46] Krutka, H., Shambaugh, R., Papavassiliou, D.; Effects of Die Geometry on the Flow Field of the Melt-Blowing Process; Industrial and Engineering Chemistry Research Vol. 42 (22) (2003)

[47] Krutka, H., Shambaugh, R., Papavassiliou, D.; Effects of Temperature and Geometry on the Flow Field of the Melt Blowing Process; Industrial and Engineering Chemistry Research Vol. 43 (15) (2004)

[48] Marla, V. and Shambaugh, R.; Modeling of the Melt Blowing Performance of Slot Dies; Industrial and Engineering Chemistry Research Vol. 43 (11) (2004)

[49] Tate, B. and Shambaugh, R.; Temperature Fields Below Melt-Blowing Dies of Various Geometries; Industrial and Engineering Chemistry Research Vol. 43 (17) (2004)

[50] Harding; J. W., Keller; J. P., Buntin; R. R.; Melt Blowing Die for Producing Nonwoven Mats, USPTO 3,825,380 (1974)

[51] Mohammed, A., Shambaugh, R.L.; Three-Dimensional Flow Field of a Rectangular Array of Practical Air Jets; Industrial and Engineering Chemistry Research Vol. 32 976-980 (1993)

[52] Shambaugh, R.; A Macroscopic View of the Melt-Blowing Process for Producing Microfibers; Industrial and Engineering Chemistry Research Vol. 27 (12) (1988)

[53] Ho, R., Hseih, P., Yang, C., Lin, J.; Crystallization Kinetics for Low-Ether-Content Polyether-Polyester Block Copolymers with Amide Linkages; Journal of Polymer Science: Part B: Polymer Physics Vol. 39 (20) 2469-2480 (2001)

[54] Gu,Q., Wu, L., Wu, D., Shen, D.; Effect of Self-Nucleation on the Crystallization of Segmented Copolymer Poly (Ether Ester); Journal of Applied Polymer Science Vol. 81(2) 498-504 (2001)

[55] Jeddi A.; Kim H. S.; Pourdeyhimi B.; Measurement of Fiber Orientation in Nonwovens: Optical Fourier Transform; International Nonwovens Journal Vol. 10 Issue 3 (Fall 2001)

[56] Pourdeyhimi, B., Dent, R.; A Note on the Measurement of Fiber Diameter Distribution in Nonwovens; Textile Research Journal Vol. 69 (4) 233-236 (1999)

[57] Niesten, M. C. E. H., Gaymans, R. J.; Comparison of Properties of Segmented Copolyetheresteramides Containing Uniform Aramid Segments with Commercial Segmented Copolymers; Journal of Applied Polymer Science Vol. 81 (6) 1372-1381 (2001)

[58] Warner, S.; Strain-induced crystallization and melting behavior of polyetheramide block copolymer; Journal of Elastomers and Plastics Vol. 22 Pages 166-173 (1990)

[59] Hatfield, G.R., Guo, Y., Killinger, W.E., Andrejak, R.A., Roubicek, P.M.; Characterization of Structure And Morphology In Two Poly (Ether-Block-Amide) Copolymers; Macromolecules Vol. 26 6350-6353 (1993)

[60] Zdharala, R.J., Gerkin, R.M., Hager, S.L., Critchfield, F.E.; Polyether-based Thermoplastic Polyurethanes. I. Effect of the Hard-Segment Content; Journal of Applied Polymer Science Vol. 24 2041-2050 (1979)

[61] Bonart, R., Morbitzer, L., Muller, E.H.*;* X-ray Investigations Concerning the Physical Structure of Cross-linking in Segmented Urethane Elastomers. II. Butanediol as Chain Extender; J. Macromol. Sci.-Phys. B3 (2) 337-356 (June, 1969)

[62] Bonart, R.; Thermoplastic Elastomers; Polymer Vol. 20 1389-1403 (November 1979)

[63] Hespe, H.F., Zembrod, A., Cama, F.J., Lantman, C.W., Seneker, S.D.; Influence of Molecular Weight on the Thermal and Mechanical Properties of Polyurethane Elastomers Based on 4,4'-Diisocyanato Dicyclohextmethane; Journal of Applied Polymer Science Vol. 44 2029-2035 (1992)

[64] Ghosh, S., Khastgir, D., Bhowmick, A.K.; Effect of Block Molecular Weight on the Mechanical and Dynamic Mechanical Properties of Segmented Polyamide; Polymer Vol. 39 (17) 3967-3975 (1998)

[65] Cella, R.; Morphology of Segmented Polyester Thermoplastic Elastomers; J. Polymer Sci.: Symposium No. 42 727-740 (1973)

[66] Reynolds, N., Spiess, H.W., Hayen, H., Nefzger, H., Eisenbach, C.D.; Structure and Deformation Behavior of Model Poly (ether-urethane) Elastomers, 1 Infrared Studies; Macromol. Chem. Phys. Vol. 195 2855-2873 (1994)

[67] Kim, H.D., Lee, T.J., Huh, J.H., Lee, D.J.; Preparation and Properties of Segmented Thermoplastic Polyurethane Elastomers with Two Different Soft Segments; Journal of Applied Polymer Science Vol. 73 345-352 (1999)

[68] Perkin Elmer Diamond DSC Manual

[69] Ratta, V., Ayambem, A., Young, R., McGrath, J.E., Wilkes, G.L.; Thermal Stability, Crystallization Kinetics and Morphology of a New Semicrystalline Polyimide Based on 1,3-bis (4-aminohenoxy) Benzene and 3,3',4,4'-biphenyltetracarboxylic dianhydride; Polymer Vol. 41(22) 8121-8138 (2000)

[70] Ren, M., Song, J., Zhao, Q., Li, Y., Chen, Q., Zhang, H., Mo, Z.; Primary and Secondary Crystallization Kinetic Analysis of Nylon 1212; Polymer International Vol.53 (11) 1658-1665 (2004)

[71] Lopez-Manchado, M.A., Arroyo, M.; Crystallization Kinetics of Polypropylene Part 4: Effect of Unmodified and Azide-Modified PET and PA Short Fibres; Polymer Vol. 40 (2) 487-495 (1999)

[72] Cho, K., Li, F., Choi, J.; Crystallization and Melting Behavior of Polypropylene and Maleated Polypropylene Blends; Polymer Vol. 40 (7) 1719-1729 (1999)

[73] Zhong, Z., Guo, Q.; Crystallization Kinetics of Miscible Thermosetting Polymer Blends of Novolac Resin and Poly (ethylene oxide); Polymer Vol. 41(5)1711-1718 (2000)

[74] Ren, M., Chen, Q., Song, J., Zhang, H., Sun, X., Mo, Z., Zhang, H., Zhang, X., Jiang, L.; Crystallization Kinetics and Melting Behavior of Syndiotactic 1,2-Polybutadiene; Journal of Polymer Science: Part B: Polymer Physics Vol. 43 (5) 553-561 (2005)

[75] Garg, S., Misra, A.; Crystallization Behavior of a Polyester-Polyamide Block Copolymer; Journal of Polymer Science: Polymer Letters Edition Vol. 23 27-31 (1985)

[76] Liu, M., Zhao, Q., Wang, Y., Zhang, C., Mo, Z., Cao, S.; Melting Behaviors, Isothermal and Non-isothermal Crystallization Kinetics of Nylon 1212; Polymer Vol. 44 (8) 2537–2545 (2003)

[77] Abouzahr, S., Wilkes, G.L.; Structure Property Studies of Polyester- and Polyether-Based MDI-BD Segmented Polyurethanes: Effect of One- vs. Two-Stage Polymerization Conditions; Journal of Applied Polymer Science Vol. 29 2695-2711 (1984)

[78] Lee, H.S., Hsu, S.L.; Structural Changes and Chain Orientational Behavior During Tensile Deformation of Segmented Polyurethanes; Journal of Polymer Science: Part B: Polymer Physics Vol. 32 2085-2098 (1994)

[79] Rao, R.S., and Shambaugh, R.L.; Vibration and Stability in the Melt Blowing Process; Industrial and Engineering Chemistry Research Vol. 32 3100-3111 (1993)

[80] Marla, V.T., and Shambaugh, R.L.; Three-Dimensional Model of the Melt-Blowing Process; Industrial and Engineering Chemistry Research Vol. 42 6993-7005 (2003)

[81] Moore, E.M., Shambaugh, R.L., Papasvassiliou, D.V.; Analysis of Isothermal Annular Jets: Comparison of Computational Fluid Dynamics; Journal of Applied Polymer Science Vol. 94 909-922 (2004)

[82] Krutka, H. M., Shambaugh, R.L., Papasvassiliou, D.V.; Analysis of Multiple Jets in the Schwarz Melt-Blowing Die Using Computational Fluid Dynamics; Industrial and

Engineering Chemistry Research Vol. 44 8922-8932 (2005)

[83] Krutka, H. M., Shambaugh, R.L., Papasvassiliou, D.V.; Analysis of the Temperature Field from Multiple Jets in the Schwarz Melt Blowing Die Using Computational Fluid Dynamics ; Industrial and Engineering Chemistry Research Vol. 46 5098-5109 (2006)

[84] Krutka, H. M., Shambaugh, R.L., Papasvassiliou, D.V.; Effects of the Polymer Fiber on the Flow Field from an Annular Melt-Blowing Die; Industrial and Engineering Chemistry Research Vol. 46 655-666 (2007)

[85] Continuous Fiber Module Manual. Fluent 6.1, Fluent Inc, 2003

[86] Ziabicki, A.; Fundamentals of Fibre Formation: The Science of Fibre Spinning and Drawing; London; New York: Wiley, c1976.

[87] Lu, F. and Spruiell, J. E.; The Influence of Resin Characteristics on the High Speed Melt Spinning of Isotactic Polypropylene. II. On-Line Studies of Diameter, Birefringence, and Temperature Profiles; Journal of Applied Polymer Science Vol. 34 Pg. 1541-1556 (1987)

[88] Patel, R. M., Bheda, J. H., and Spruiell, J. E. Dynamics and Structure Development During High-speed Melt Spinning of Nylon 6. II. Mathematical Modeling; Journal of Applied Polymer Science Vol. 42 Pages 1671-1682 (1991)

[89] Matsuo, T., Kase, S.; Studies on Melt Spinning. II. Steady-state and Transient Solution of Fundamental Equations Compared with Experimental Results; Journal of Applied Polymer Science Vol. 11 251-287 (1967)

[90] Matsuo, T., Kase, S.; Studies on Melt Spinning. I. Fundamental Equations on the Dynamics of Melt Spinning; Journal of Polymer Science: Part A Vol.3 2541-2554 (1965)

[91] Majumdar, B. and Shambaugh, R.; Air Drag on Filaments in the Melt-blowing Process; The Society of Rheology Vol. 34 (4) (1990)

[92] Kayser, J. and Shambaugh, R.; The Manufacture of Continuous Polymeric Filaments by the Melt-Blowing Process; Polymer Engineering and Science Vol. 30 No. 19 (1990)

[93] Zhao, R. and Wadsworth, L. C.; Attenuating PP/PET Bicomponent Melt Blown Microfibers; Polymer Engineering and Science Vol. 43 No. 2 (2003)

[94] Bheda, J. H. and Spruiell, J. E.; Dynamics and Structure Development during High Speed Melt Spinning of Nylon 6. I. On-Line Experimental Measurements; Journal of Applied Polymer Science Vol. 39 Pages 447-463 (1990)

[95] Zieminski, K., Spruiell, J.; On-Line Studies and Computer Simulation of the Melt Spinning of Nylon-66 Filaments; Journal of Applied Polymer Science Vol. 35 Pages 2223-2245 (1988)

[96] Lu, F. and Spruiell, J. E.; The Role of Crystallization Kinetics in the Development of the Structure and Properties of Polypropylene Filaments; Journal of Applied Polymer Science Vol. 49 Pages 623-631 (1993)